CFD Analysis of Air Lubrication Effects on Ship Propulsive Performance

Master's Thesis

Arne Heuvelman

TU Delft

DAMEN

Thesis for the degree of MSc in Marine Technology in the specialization of Ship Hydromechanics and Ship Design

CFD Analysis of Air Lubrication Effects on Ship Propulsive Performance

by

Adrianus Marinus Heuvelman

at

Damen Shipyards Group

This document is an adapted version of the thesis for publication purposes. All dimensions of the DACS system are omitted and are classified as confidential, in accordance with the general conditions for projects conducted by Delft University of Technology.

Report number: MT.23/24.039.M
To be defended publicly on July 17, 2024, at 14:00
Faculty of Mechanical Engineering, Delft University of Technology

Company supervisors:

Responsible/daily supervisor	Dr.ir. O. Zverkhovskyi	
Responsible supervisor	ir. S. Terry	

Thesis exam committee:

Chair	Prof.dr.ir. T.J.C. van Terwisga	TU Delft
Staff member	Dr.ir. P.R. Wellens	TU Delft
Staff member	Dr.ing. C.H. Thill	TU Delft
Staff member	Dr.ir. M.J.B.M. Pourquie	TU Delft
Company member	Dr.ir. O. Zverkhovskyi	Damen Shipyards Group
Company Member	ir. S. Terry	Damen Shipyards Group
External member	ir. M. Kerkvliet	Marin

Author details:

Student number	4862317
Author contact email	

Cover: Damen CF3850 Indigo

Preface

The completion of the work that follows has been made by the support and contribution of many people. First of all, I want to thank Sasha Zverkhovskyi for his supervision of the project. He helped me to get a detailed understanding of the working principles of the air cavity system his feedback on the research results has been greatly appreciated. Additionally, I want to acknowledge Scott Terry from the Damen RD&I department for his daily supervision and insightful advice, drawing from his experience in CFD, ship resistance, and propulsion. Next to this, I am also very grateful for the opportunity to see the air cavity system in practice during experimental tests. This improved my understanding of the cavity system and also increased my enthusiasm for the project. Furthermore, I am also thankful to Georgios and Cagri for their assistance with 3D modeling in Rhinoceros, grid generation, and CFD simulation setup. Their contributions have been essential to the project's progress. A special thanks to Tom van Terwisga for his supervision of the project from the university's perspective. His enthusiasm and expert opinion were encouraging. I am also thankful to Maarten Kerkvliet that he was able to make time for this project and share his opinion on the CFD results. Lastly, I am very grateful to my family for all their support during my studies, particularly during my work on the master's thesis. Their encouragement has been a constant source of motivation.

Arne Heuvelman
Gorinchem, July 2024

Summary

Shipping is one of the most cost-effective and environmentally sustainable modes of transportation. Given that approximately 60% of a typical ship's propulsive power is used to overcome frictional drag, implementing practices to reduce this resistance stands to yield substantial economic and environmental benefits, (Larsson & Raven, 2010). A promising drag reduction technique for a ship is air lubrication. Damen Shipyards Group is currently making this technology commercially available as the Damen Air Cavity System (DACS). The system reduces the frictional resistance of a ship by creating stable air cavities on the bottom hull of a ship. The air cavities cause a reduction in friction drag by decreasing the wetted area of a ship's bottom. During the development of the DACS system, it was observed that air cavities also change the inflow into the propeller. Both the changed inflow and the frictional drag reduction affect the propulsive efficiency and required propulsive power of the vessel. This thesis aims to provide a better understanding of how the propulsive performance of a ship is affected by air cavities. Additionally, a key application for air lubrication systems is on inland waterway vessels, which frequently operate in shallow waters. However, the impact of shallow water conditions on the performance of the air cavity system is currently unknown.

The research goals of this thesis are investigated with the help of computational fluid dynamics (CFD). A literature review identified the most feasible method to model a ship with air cavities i.e. representing the cavities as surfaces with a slip boundary condition. The influence of the air cavities on propulsive performance is investigated by studying the change in nominal wake field, thrust deduction, and propeller efficiency. Three ships were investigated: a cargo ship, a cruise ship, and an inland ship. The CFD results of the cargo ship were compared to sea trial data. Model test data was available for comparison of the cruise ship results. First, a grid convergence study and a sensitivity analysis were performed to investigate the accuracy of the numerical simulations and the power predictions. The biggest source of numerical uncertainty arose from the pressure drag. From the sensitivity analysis, it was found that the uncertainty of the power prediction is mainly affected by the uncertainty of the thrust prediction, followed by the uncertain propeller geometry for the cargo ship.

For the cargo ship, it was found that the air cavities cause a significant frictional drag reduction. It was also found that the air cavities caused a decrease in pressure drag because they decreased flow separation at the stern. Furthermore, a strong decrease of the nominal wake fraction was observed for this ship, because the air cavities change the boundary layer on the bottom of the ship. A change in propeller efficiency was also observed because the propeller working point changes. The magnitude of the change was larger than for the other ships because this ship has a controllable pitch propeller running at a fixed rpm. When comparing sea trial data to the CFD results, it was found that CFD underpredicts the power, especially at higher speeds. Next to this, CFD predicted a larger reduction in power than measured during the trials. The prediction of the cavity length was identified as the most likely cause for the difference.
A good comparison between model tests and CFD results was found for the cruise ship. It was found that the drag reduction and change in propulsive performance could be predicted reasonably accurately by modeling the air cavities as surfaces with a slip boundary condition. Furthermore, it was observed that the air cavities caused little change in propulsive efficiency on this ship. This is because the propellers of the cruise ship are located further away from the boundary layer of the ship and the wake field is therefore only slightly affected by the air cavities.
On the inland ship, it was observed that the pressure drag and flow separation at the stern were influenced due to the air cavities. However, no comprehensive conclusions could be made due to scatter in the data. This is most likely due to the uncertainty present when modeling flow separation. Furthermore also for this ship, a decrease in propulsive efficiency was found because the air cavities decreased the wake fraction of the ship. Additionally, CFD simulations were conducted for the inland ship at varying water depths to assess how shallow water conditions impact the performance of the air cavity system. Since the ship's frictional drag increased in shallow water, the total drag reduction from the air cavities also increased. Next to this, a change between pressure and flow separation when comparing air on and air off was observed. Also here, no strong conclusion could be made due to scatter in the data. Lastly, it was found that the change in wake field caused by the air cavities is larger in shallow water than in deep water.

Based on the results of the three ships studied it can be concluded that an air cavity system affects the propulsive performance of a ship. It was found that an air cavity system reduces the wake fraction of a ship because it limits the growth of the boundary layer on the bottom of a ship. The reduction increases for ships with a high block coefficient and a large air-covered area. For a twin screw ship, the change of the wake field is less significant. The change in propeller efficiency depends on the resistance reduction, possible change of the wake field, and the original working point of the propeller. Furthermore, it was found that the thrust deduction effect is not affected by the air cavity system. It can also be concluded from the results of the cruise ship that the flow around a ship with air cavities can modeled reasonably accurately provided that the shape of the air layer under the ship is known. More research is recommended on how air cavities change the flow separation and pressure drag of a ship.

Contents

List of symbols

Roman symbols

A_e/A_0	Propeller blade area ratio	-
$A_{ellipse}$	Ellipse area	m^2
A_T	Dry projected frontal area	m^2
A_{wl}	Waterline area	m^2
AHR	Average hull roughness	m
AR	Air cavity aspect ratio	-
B	Ship beam	m
B	Bias error	-
ΔC_{air}	Wind resistance coefficient	-
ΔC_{rough}	Roughness resistance coefficient	-
C	Volume fraction	-
C_T	Total resistance coefficient	-
C_x	Coefficient of axial wind force	-
c	Wave propagation velocity	m/s
c_b	Block coefficient	-
c_g	Group propagation velocity	m/s
c_p	Prismatic coefficient	-
c_w	Waterplane coefficient	-
D	Propeller diameter	m
DR	Drag reduction rate	-
E	Comparison error	-
EF	Drag reduction efficiency coefficient	-
F_i	Body force	N
Fr	Froude number	-
Fr_h	Depth-based Froude number	-
f_{bx}	Body force distribution actuator disk model in axial direction	N/m^2
f_{br}	Body force distribution actuator disk model in radial direction	N/m^2
$f_{b\theta}$	Body force distribution actuator disk model in tangential direction	N/m^2
g	Gravitational constant	m/s^2
H	Water depth	m
h_i/h_1	Grid refinement ratio	-
h_{skeg}	Skeg height	m
H/T	water depth to ship draft ratio	-
i	Sinkage	m
i_p	Longitudinal center of buoyancy	-
i_w	Longitudinal center of flotation	-
J	Advance ratio	-
K_T	Thrust coefficient	-
$K_{T,ship}$	Ship Thrust coefficient	-
K_Q	Torque coefficient	-
k_p	Number of propellers	-
L	Length	m
L_{cav}	Cavity length	m
$L_{cav,d}$	Cavity length in deep water	m
$L_{cav,s}$	Cavity length in shallow water	m
L_{pp}	Length between perpendiculars	m
L_{wl}	Waterline length	m
m	Mass	kg
N_i	Number of cells in the i-th mesh	-
n_p	Propeller rotational speed	rev/s

n_g	Numer of grids	-
P	Precision error	-
P_B	Engine brake power	W
P_{comp}	Compressor power	W
P_D	Delivered power	W
P_E	Effective power	W
P_N	Net power saving of the air lubrication system	W
P_T	Thrust power	W
P_{save}	Power saved by the air lubrication system	W
P_s	Shaft power	W
$P_{s,air,on}$	Shaft power air on	W
$P_{s,ref}$	Shaft power reference case	W
P/D	Propeller pitch to diameter ratio	-
p	Observed order of grid convergence	-
Q	Propeller open water torque	Nm
R	Ship resistance	N
ΔR_{DACS}	Added resistance of the DACS appendages	N
R_H	Propeller hub radius	m
R_P	Propeller radius	m
R_{add}	Added resistance	N
R_{cor}	Corrected resistance	N
R_f	Frictional resistance	N
R_p	Pressure resistance	N
R_v	Viscous resistance	N
Re	Reynolds number	-
S_{cav}	Air-covered area	m^2
S_{wet}	Wetted area	m^2
ΔT	Change in draft	m
T	Thrust	N
T	Ship draft	m
T_{aft}	Draft aft	m
T_{fore}	Draft fore	m
Δt	Time step	s
(t)	Thrust deduction fraction	-
$(1-t)$	Thrust deduction factor	-
t_{cav}	Air cavity thickness	m
u	Uncertainty	-
u_c	Uncertainty of computed result	-
u_e	Experimental uncertainty	-
u_m	Modeling uncertainty	-
u_n	Numerical uncertainty	-
u_{val}	Validation uncertainty	-
u_z	Output uncertainty	-
V	Flow velocity	m/s
V_{ref}	Reference velocity	m/s
V_{ship}	Underwater volume of the ship	m^3
v_a	Advance velocity	m/s
$v_{cav,lim}$	Velocity at which the cavity length is limited by the skeg height	m/s
v_s	Ship speed	m/s
W_{cav}	Cavity width	m
(w)	Wake fraction	-
(w_n)	Nominal wake fraction	-
$(1-w)$	Wake factor	-
$(1-w_n)$	Nominal wake factor	-
x	Input quantity	-
x_0	Nominal value of input quantity	-
Y_{PC}	Y-coordinate of the propeller center	m

y^+	Dimensionless wall distance	-
Z_{PC}	Z-coordinate of the propeller center	m
z	output quantity	-

Greek symbols

α	Constant in discretization error approximation	-
Δ	Displacement	ton
Δ	Actuator disk thickness	m
Δ_ϕ	Data range parameter	-
ϵ_ϕ	Discretization error	-
λ	Wave length	m
η_D	Propulsive efficiency	-
η_h	Hull efficiency	-
η_o	Open water efficiency	-
η_r	Relative rotative efficiency	-
μ	Dynamic viscosity	Ns/m^2
μ_a	Air dynamic viscosity	Ns/m^2
μ_w	Water dynamic viscosity	Ns/m^2
ρ	Density	kg/m^3
ρ_a	Air density	kg/m^3
ρ_w	Water density	kg/m^3
τ_w	Wall shear stress	N/m^2
ϕ_0	Estimate of the exact solution of ϕ_0	-
ϕ_i	Any integral or other functional of a local flow quantity	-
∇	Displacement	m^3

Abbreviations

ALDR	Air layer drag reduction
ALS	Air lubrication system
BDR	Bubble drag reduction
DACS	Damen Air Cavity System
DNS	Direct numerical simulation
DR	Drag reduction rate
LES	Large eddy simulation
RANS	Reynolds averaged Navier Stokes equations
RSM	Reynolds stress model
TALDR	Transitional air layer drag reduction
VoF	Volume of Fluid

List of Figures

List of Tables

Chapter 1
Introduction

1.1 Background

Air lubrication for ships, an innovative technology aimed at reducing fuel consumption and emissions, has gained significant attention in recent years due to the increasing global emphasis on environmental sustainability and cost efficiency in maritime operations. This technique involves creating an air layer between the ship's hull and the water, which reduces frictional resistance and thereby enhances fuel efficiency. Given the maritime industry's substantial contribution to global greenhouse gas emissions, the implementation of air lubrication systems presents a promising solution to mitigate environmental impact while also offering economic benefits through reduced operational costs. This relevance is underscored by the International Maritime Organization (IMO) targets, which aim to cut the shipping industry's greenhouse gas emissions by at least 40% by 2030 compared to 2008 levels and reach near-zero GHG emissions by 2050, (International Maritime Organization, 2023).

This thesis aims to contribute to the advancement of air lubrication technology by focusing on improving power savings predictions. By developing more reliable predictions of energy savings, this research seeks to facilitate the development of better systems and enable the maritime industry to make informed decisions regarding the adoption of air lubrication technology.
The thesis is written in collaboration with Damen Shipyards Group. Damen Shipyards Group is a family-owned company with a global presence, engaged in both ship construction and maintenance and repair services. Its extensive product portfolio includes tugs, workboats, patrol vessels, cargo ships, dredgers, superyachts, and fast ferries. Damen, as a family business with a long-term perspective, is dedicated to securing the future for generations to come. Striving to be the most sustainable shipbuilder globally, Damen's ambitions center on achieving circularity and zero emissions sailing. In line with these ambitions, Damen developed the Damen Air Cavity System (DACS). The system reduces the frictional resistance of ship by creating stable air cavities on the bottom hull of a ship. The air cavities cause a reduction in friction drag by decreasing the wetted area of a ship's bottom. Fuel savings between 7 and 12% can be obtained depending on the ship type, (Damen Shipyards Group, 2023). Figure 1.1 shows air cavities in an experimental setup.

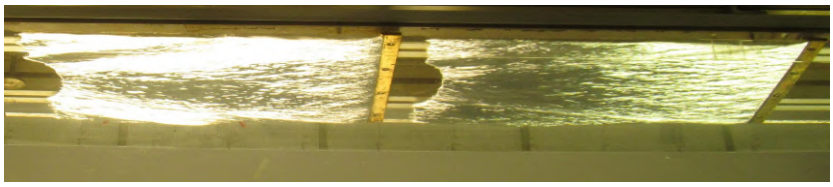

Figure 1.1: Two air cavities in an experimental setup, Damen footage.

Different air lubrication techniques have been developed in the past, see Gorbachev and Amromin (2012) and Thill (2016). The technology behind the DACS system was originally developed at the Delft University of Technology (TU Delft). Zverkhovskyi (2014) performed fundamental experimental research to understand the flow physics of external air cavities. Extensive research in numerical modeling of air cavities was performed amongst others by Rotte et al. (2019). After extensive R&D work, the system was commercialized by Damen Shipyard Group. Recently, the first system was installed on a general cargo vessel. Fuel savings up to 7% were measured during sea trials, (Damen Shipyards Group, 2023).

1.2 Problem statement

An air cavity system reduces the frictional drag of a vessel. In literature, see section 2.6, and during model tests with the DACS system, it was observed that air cavities also change the inflow into the propeller. Both the changed inflow and the frictional drag reduction affect the propulsive efficiency and

required propulsive power of the vessel. A better understanding of how the propulsive performance of a ship is affected by air cavities is required to make a better prediction of the potential fuel savings of DACS. Moreover, it could also aid propeller design for new-build ships equipped with the air cavity system.

Furthermore, an important application for the Damen Air Cavity System is on inland waterway vessels. These vessels have a large frictional drag, but also a large flat bottom area. Therefore for such vessels, a substantial decrease in fuel consumption can be obtained with DACS. Inland ships often sail in shallow water. Currently, it is not known how the shallow water effect influences the performance of the air cavity system. During model tests on a vessel with external air cavities, a larger drag reduction rate in shallow water than in deep water was measured. However, only a single measurement point was obtained.

1.3 Research question

The problem statement of this research is summarized in a research question:

How does an external air cavity system affect the propeller performance of a ship?

The main research question is supported by several sub-questions:

1. How does the propeller-hull interaction change?
2. How does the propeller efficiency change?
3. How does the change in propeller performance affect the estimated power savings of the system?
4. What will be the effect of optimizing the propeller in combination with DACS?
5. What is the influence of the shallow-water effect?

How does the propeller-hull interaction change?

More specifically the goal of this question is to investigate how the propeller wake field, the self-propulsion factors, and the hull efficiency change due to the application of air cavities.

How does the propeller efficiency change?

The resistance of a ship with air cavities will decrease. Therefore the propeller will operate at a different working point. The propeller efficiency and rotational speed will also be different at this working point.

How does the change in propeller performance affect the estimated power savings of the system?

Currently, the power savings of DACS are estimated based on the drag reduction rate and required compressor power of the system. However, due to the changed propeller working point and self-propulsion the power savings might also be different.

What will be the effect of optimizing the propeller in combination with DACS?

The effects of the air cavity system on the propeller performance are currently not taken into account. If the air cavity system causes a large change in propulsive efficiency it might be worth to redesigning the propeller.

What is the influence of the shallow water effect?

The shallow water effect changes the drag reduction rate of the air cavity system. It can also change the propulsive efficiency of the vessel.

1.4 Research approach and scope

The research questions will be answered using computational fluid dynamics. Currently, there is not enough data available from model tests or sea trials to draw firm conclusions. Performing additional model tests or sea trials is not within the scope and available budget for this project.

First of all a literature study was performed into the current state-of-the-art knowledge available on the research question, see chapter 2. The literature review also involved a investigation into the most feasible CFD modeling technique for the flow around a ship with air cavities. It was concluded that the airflow on the bottom of the ships will not be resolved, see section 2.5.3. Instead, a simplified model is applied: the air cavity shape is approximated and the cavities are modeled as surfaces with a slip boundary condition. This modeling approach is not yet mature, validation has only been performed for a single air cavity in an experimental setup, (Zverkhovskyi et al., 2015) and (Zverkhovskyi, 2023). Furthermore, CFD simulations always give rise to additional numerical and modeling uncertainties. Therefore verification and validation are performed first to assess the corresponding uncertainties in the results of CFD simulations.

Afterwards, the research questions are answered based on the results of case studies on three different ships. The ships are different in terms of hull form, resistance decomposition, and propulsion arrangement. For each ship type CFD simulations are performed before the installation of the air cavity system, and after the installation with air on. A comparison is made between both cases. The shallow water effect is investigated for the inland ship because such a ship often sails in shallow water. For this ship simulations are performed at multiple water depths and in deep water for comparison, both with air on and air off. Sea trial measurements are available for the general cargo ship, whereas model test results are present for the cruise ship. The CFD results will be compared to the experimental data.

1.5 Scope

The main focus of the project will be on how external air cavities affect the propeller performance. This applies to all vessels that can be equipped with the Damen Air Cavity System. The shallow water effect is also important but only applies to certain vessel types, such as inland vessels. Therefore it will be a subquestion of the research and it is studied less extensively. This research will only focus on external air cavities. This method seems to be the most practical and effective air lubrication technique, (Zverkhovskyi, 2014), and is applied in the Damen Air Cavity System (DACS). Therefore only vessel types that are relevant for DACS are investigated. It is believed that the selected vessel types contain a broad distribution of vessels with different hull form shapes and different flat bottom areas.

No effort will be put into trying to solve the problems currently obtained with the two-phase flow modeling of external air cavities using RANS, (Rotte et al., 2019). The focus of the research will be more on the practical applications of external air cavities. Consequently, a simplified modeling method is applied to resolve the air cavities.

Lastly, the required air flow rate for the air cavity system is not considered. It is also not related to the propulsive efficiency of the ship. As a result, all power predictions will be made for delivered power. The engine(s) is not considered.

1.6 Thesis outline

The thesis outline is as follows: This chapter presents an introduction to the problem addressed in this thesis. Chapter 2 gives an overview of the relevant physical theory and physical principles. It also describes the state-of-the-art literature available. Afterwards, chapter 3 describes the modeling method in detail. It also explains the setup of the CFD simulations. Verification and validation of the modeling method are presented in chapter 4. After that, the results of the three case studies are presented in chapters 5, 6, and 7. The case studies involve a general cargo ship (including a comparison with sea

trial data), a cruise ship (including a comparison with model test data) and an inland ship (both in deep and in shallow water). A discussion and analysis of some important findings and assumptions are given in chapter 8. Chapter 9 presents the conclusions of the research. Lastly, a discussion of the limitations of the used method is presented and recommendations for further research are made in chapter 10.

Chapter 2
Theoretical framework & Literature review

First of all an overview of the relevant theory and physical principles for this research are presented. Afterwards, the current state-of-the-art research available on the topic is presented.

2.1 Air lubrication

Air lubrication is a promising energy-saving method that can be used to decrease fuel consumption and greenhouse gas emissions from ships. An air lubrication system (ALS) decreases the frictional drag of a ship by injecting air under the flat bottom of a ship. The system gives the highest drag reduction for vessels for which the frictional resistance accounts for a large portion of the ship's total resistance. Furthermore, the effectiveness of the system increases for vessels with a larger flat bottom area, since air can only be injected under the flat bottom of a ship. As a result slow-sailing vessels with a large flat bottom area like tankers, bulk carriers, and inland vessels can gain the largest energy savings with air lubrication. For more slender and faster vessels like container ships and ferries still fuel savings can be obtained, but they will be lower. Multiple different air lubrication techniques have been developed: air bubble drag reduction, air layer drag reduction, internal air cavities, and external cavities. Each technique has its advantages and disadvantages. They will be discussed in more detail in the next sections.
The flow around an air lubricated ship is a multiphase flow. Two different multiphase flow regimes can be distinguished, see also figure 2.1:

1. Disperse flows: flows consisting of finite particles, drops or bubbles (the disperse phase) distributed in a connected volume of the continuous phase
2. Separated or stratified flows: two or more continuous streams of different fluids separated by interfaces.

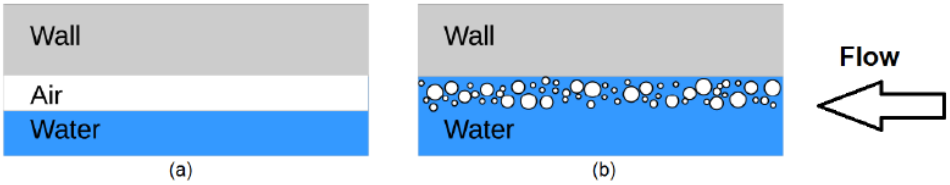

Figure 2.1: Multiphase flow regimes relevant for air lubrication techniques, (Rotte et al., 2016).

2.1.1 Air bubble drag reduction

With the bubble drag reduction (BDR) method numerous air bubbles are injected under the bottom of the ship. The air bubbles can be created by e.g. injecting air through a porous medium. A BDR flow is classified as a flow in the dispersed flow regime in which water is mixed with air bubbles. The working principle of bubble drag reduction is not fully understood and a discussion is ongoing regarding the different underlying physical mechanisms, (Rotte et al., 2016) and (Elbing et al., 2013). Rotte et al. (2016) describes that the most straightforward drag reduction mechanisms are based on a change in the local density and viscosity of the flow. The difference in density and viscosity between water and air is in the order of 10^3. For these mechanisms, it is essential that the air bubbles are present in the ship's boundary layer. Elbing et al. (2013) states that it is generally agreed that bubbles interact with and can be deformed by the turbulent boundary layer and that they can lower the near-wall Reynolds stress $-\rho\langle u'v'\rangle$. According to Murai (2014) the drag reduction mechanism of air bubbles is little explained by a single universal hypothesis. Multiple different mechanisms exist that depend on

the flow speed, and the bubble size. Furthermore, he also reports that flow regimes (depending on flow speed and bubble size) exist for which air bubbles cause a drag increase rather than a drag decrease.

Both Sanders et al. (2006) and Elbing et al. (2008) performed experimental tests of BDR on a flat plate. Those tests were performed at high Reynolds numbers, to get as close to a full-scale ship as possible. Sanders et al. (2006) found that the frictional drag reduction effect of the air bubbles is lost after the first few meters downstream of the air injector. Also Elbing et al. (2008) found a relatively poor downstream persistence of the drag reduction effect. Significant drag reduction is limited to the first few meters downstream of air injection. During full-scale trials of an inland vessel equipped with a BDR, no drag reduction effect was observed, (Thill, 2016). However, the commercial company Silverstream Technologies reported a net power saving of 4% at full-scale tests of their system, (Silberschmidt et al., 2016).

2.1.2 Air layer drag reduction

Elbing et al. (2008) observed during experiments with a flat plate in a water tunnel, that a bubbly flow can transform into an air layer flow when a sufficient amount of air is injected. He distinguishes three different flow regimes based on the air injection rate and the corresponding drag reduction rate, see figure 2.2.

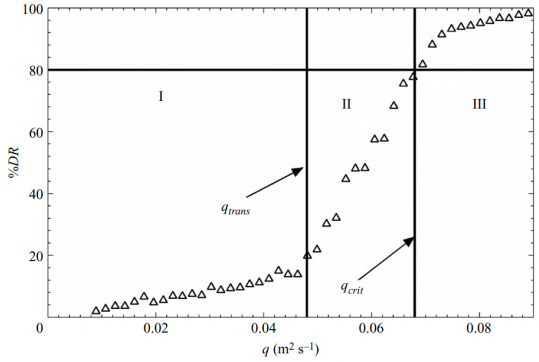

Figure 2.2: Measured drag reduction rate %DR versus air injection rate q on a flat plate. Three different flow regimes are observed: a BDR regime (I), a TALDR regime (II), and an ALDR regime (III), (Elbing et al., 2008).

This same effect was also observed by Nikolaidou et al. (2021). The three different flow regimes are classified as follows:

I. The bubble drag reduction (BDR) regime. The flow is characterized by the presence of dispersed bubbles.

II. The transitional air layer drag reduction (TALDR) regime. In this regime alternating regions of bubbly flow and segments of air layer are present.

III. The air layer drag reduction (ALDR) regime. Here a continuous air layer is formed. This is a stratified flow regime.

The three different flow regimes are also illustrated in figure 2.3

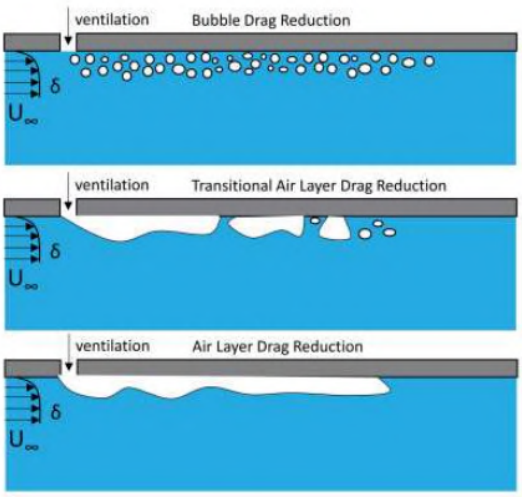

Figure 2.3: Schematic representation of three different air layer regimes, (Nikolaidou et al., 2021).

It was observed that the air layer could persist over the entire length of the test section. In contrast to BDR, no decay in the level of drag reduction was observed over length. Therefore a much larger drag reduction rate can be obtained with ALDR, despite the larger required air injection rate. The drag reduction mechanism of an air layer is also different compared to BDR. It is based on a reduction of the wetted surface. The wall friction of air is in the order of 10^3 times smaller compared to the wall friction of water due to the difference in density, (Rotte et al., 2016). A disadvantage of ALDR is the low stability of the air layer, (Zverkhovskyi, 2014). In laboratory conditions, the air layer can persist over a large length. In reality, for sea-going ships, it will not be possible to maintain a stable air layer. A more stable flow can be obtained by creating an air cavity, either an external or an internal air cavity. The three different methods to obtain a stratified flow regime, ALDR, the external air cavity, and the internal air cavity are all based on the same physical mechanism: a reduction of the wetted area. The three different methods are illustrated in figure 2.4

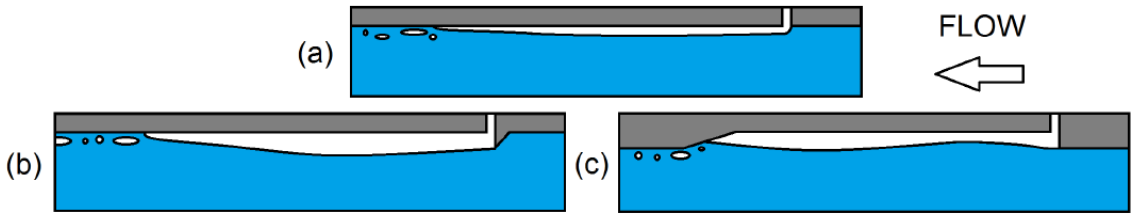

Figure 2.4: Three different methods to obtain a stratified flow: natural air layer (a), external cavity (b), and internal cavity (c), (Rotte et al., 2016).

The advantage of air cavities compared to a natural air layer is that they are more stable at a lower flow rate. Their main disadvantage is, however, that they require additional modifications to the ship hull. Another option to increase the stability of an air layer is the use of a superhydrophobic coating. A superhydrophobic coating is a water-repellent coating that requires a significantly lower air flux to maintain a stable air layer, (Peifer et al., 2020). However, Thill (2016) found that such a coating has multiple drawbacks in practice. The coating is expensive, and very sensitive to wear and marine growth.

2.1.3 Internal air cavity

An internal air cavity, also known as an air chamber, can be created by injecting air into a recess in the bottom of the ship hull. The mean flow is separated from the air layer by injecting the air

behind a backward-facing step. At the closure region, the air and water flow merge at the so-called beach. In contrast to an external air cavity, the length of the free surface is not limited. Instead, a multi-wavelength air cavity can be formed. (Rotte et al., 2016) Internal air cavities have been proven to be effective in practice. In Russia, power savings between 15 and 25% have been obtained for river-going vessels during full-scale trials, (Gorbachev & Amromin, 2012). In the planing speed regime, the frictional resistance also takes up a considerable part of the total resistance so internal air cavities are a useful way for drag reduction for high-speed planing vessels as well. They have been applied to e.g. Russian military high-speed craft. (Matveev, 2003) However, internal air cavities also have some big disadvantages, (Zverkhovskyi, 2014). First of all, drastic modifications to the ship hull are required; a recess should be created in the bottom of the hull. As a result, the draft of the vessel is limited in shallow water and also the ship's structural weight can increase. Furthermore, a large drag increase will be observed if the air supply system fails.

2.1.4 External air cavity

In contrast to an internal air cavity, no bottom recess is required for an external air cavity. An external air cavity can be created by injecting air behind a co-called "cavitator". A cavitator is an obstruction in the spanwise direction that creates a suction pressure downstream of it. In this way, the mean flow can be separated from the wall. An external cavity requires side fences/skegs to remain stable, otherwise the air will leak away from the sides. It has been observed that the maximum stable cavity length that can be obtained, equals half a gravity wave length. Therefore the maximum cavity length in deep water can be computed using linear wave theory, for a given ship speed v_s as follows:

$$L_{cavity} = \frac{v_s^2 \cdot \pi}{g} \tag{2.1}$$

This means that multiple external cavities should be created on the bottom hull to get as much coverage with air as possible. This is different from internal air cavities which can have a multi-wavelength profile. A disadvantage of external cavities is that the system requires appendages on the bottom hull (cavitators and side fences). These appendages cause additional drag that is present both if the system is on and if it is not working. Zverkhovskyi (2014) performed model tests of an inland vessel with external air cavities. A net drag reduction caused by the external air cavity system of 8 and 12% was measured. During this model tests it was observed that external air cavities affect the hydrostatic stability of a vessel for small heeling angles. This problem can be solved by separating the air cavity into multiple cavities in the transverse direction.

A commercial external air cavity system is DACS. The Damen Air Cavity System (DACS) is an air lubrication system developed by Damen Shipyards Group. The system creates stable air cavities on the flat bottom of a ship. Fuel savings between 7 and 12% can be obtained for sea-going ships, depending on the ship type. For inland waterway vessels fuel savings between 10 and 20% are claimed, due to their relatively low speed and their large flat bottom area. Figure 2.5 shows the system fitted to different ship types. (Damen Shipyards Group, 2023)

Figure 2.5: The Damen Air Cavity System (DACS) for different ship types, (Damen Shipyards Group, 2023).

Air cavities can have a larger drag reduction rate than BDR. Furthermore, they are more stable than air layer drag reduction. (Zverkhovskyi, 2014) The largest drag reduction rate can be obtained with internal air cavities. (Rotte et al., 2016) However, they are less suitable from a practical and a commercial perspective than external air cavities, because of the large recess that should be created in the bottom of a ship. This can be done for new-build vessels, but it is usually not possible or desired when the system is installed on an existing vessel. The Damen air cavity system uses external air cavities as the drag reduction technique. Furthermore, considering the advantages and disadvantages described above, it appears that external air cavity drag reduction is an effective and efficient method for reducing the frictional drag experienced by a vessel. Therefore, this research will mainly focus on external air cavities. The next section will discuss some more aspects of external air cavities.

Details

This section will discuss some more details of external air cavities. Some physical principles, but also practical issues will be covered.

Air loss

For both internal and external air cavities, the air flux required to create the cavity is larger than the air flux required to maintain the cavity. Air is lost from the cavity in the closure region due to three different physical mechanisms: the re-entrant jet mechanism, the wave pinch-off mechanism, and the ligament stretching mechanism, see also figure 2.6. (Rotte et al., 2016) and (Rotte et al., 2023)

The re-entrant jet mechanism is observed for sheet cavities and breaks up the sheet cavity into cloud cavities. The mechanism works as follows: a high adverse pressure gradient is formed in the closure region of sheet cavities. The increase in local pressure forces a thin liquid stream into the cavity called a re-entrant jet. The re-entrant jet destabilizes the cavity. As a result, part of the cavity breaks up and is advected with the flow.

The wave pinch-off mechanism is governed by capillary-gravity waves at the air-water interface. It is hypothesized that these waves are formed by turbulence structures from the turbulent boundary layer upstream of the cavity that disturb the free surface. When the wave amplitude off the capillary-gravity wave equals the cavity thickness, parts of the cavity and pinched off by the waves.

Ligament stretching mechanism The ligament stretching mechanism is governed by viscous forces from the water phase that stretch out gas ligaments. The ligaments break up due to instabilities and are advected downstream by the water flow. Strong velocity gradients need to be present close to the cavity interface, for the ligament stretching mechanism to occur. The contribution of each of these mechanisms depends on the flow conditions and the cavity geometry.

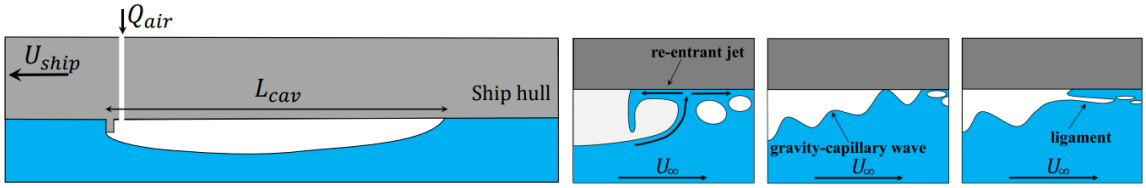

Figure 2.6: Schematic of an external air lubrication system and the possible air loss mechanisms. Re-entrant jet (left), wave pinch-off (middle), and ligament stretching (right), (Rotte et al., 2023).

Cavity length

Both design and modeling purposes require a prediction of the cavity length. A prediction of the caviy length can be made base on observations from experimental research. Zverkhovskyi (2014) found that the maximum stable length of an external air cavity is limited by half a gravity wave length. Therefore it can be derived from potential flow theory that in deep water the maximum stable cavity length L_{cav} can be computed as :

$$L_{cavity} = \frac{v_s^2 \cdot \pi}{g} \tag{2.2}$$

This equation shows that the cavity length increases with the flow velocity (or ship speed). However, Zverkhovskyi (2014) also found that the thickness of an air cavity increases linearly with length, see equation 2.3. During experiments in a cavitation tunnel on an air cavity he found that all measurements (different flow speeds and different cavitator heights) collapsed on a single line. This means that the aspect ratio of a cavity can be assumed constant:

$$AR = \frac{L_{cav}}{t_{cav}} = 60 \tag{2.3}$$

The shape of an air cavity can be approximated by an ellipse, (Zverkhovskyi et al., 2015). Meaning that the maximum thickness of a cavity is observed halfway its length. When the cavity thickness is larger than the height of the skegs at the sides of the cavity, the air will escape sideways. As a result, the cavity length cannot grow further. This means that at low speed the cavity length is limited by half a gravity wave length. At higher speed the cavity length is limited by the skeg height. It cannot increase anymore although the flow speed would be increased. This is also illustrated in figure 2.7. The velocity at which the cavity length can no longer grow due to the limited skeg height is called $v_{cav,lim}$ and can be computed in the following way:

$$v_{cav,lim} = \sqrt{\frac{AR \cdot h_{skeg} \cdot g}{\pi}} \tag{2.4}$$

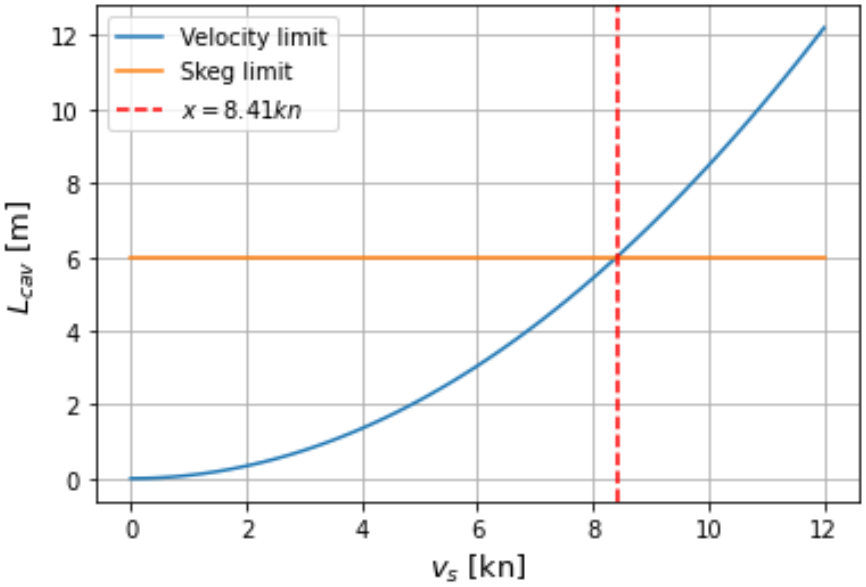

Figure 2.7: Cavity length limit for a skeg height of 0.1m.

The skeg height is therefore an important design parameter for the air cavity system. A high skeg height will increase the maximum cavity length. However, it also limits the maximum draft of the ship, e.g. in ports. In turn, a low skeg height will results in more cavities behind each other. On the area in between the cavities a new boundary layer is created and a thin boundary layer has a higher skin friction. Furthermore, a larger skeg will also cause a higher appendage drag. The skeg height will therefore be a compromise between those effects.

Drag reduction mechanism

As explained earlier the working mechanism for drag reduction of air cavities is the reduction of the wetted area. However, the frictional resistance reduction of external air cavities is not proportional to the wetted area reduction; in fact, it is lower. (Zverkhovskyi, 2014) and (Zverkhovskyi, 2023) The reason for this is that the local skin friction coefficient on the surfaces between the air cavities is higher compared to the situation without cavities. For a general boundary layer on a flat plate, the boundary

layer grows, so its thickness increases over the length of the flat plate. The local shear stress τ_w is proportional to the wall-normal derivative of the local velocity at the wall:

$$\tau_w = \mu \cdot \left. \frac{\partial u}{\partial y} \right|_{y=0} \tag{2.5}$$

For a thicker boundary layer, this derivative decreases. Therefore also the local shear stress and thus the local skin friction decreases with boundary layer thickness and thus with length. Due to the much lower skin friction of air compared to water, the cavities can be approximated as surfaces with a slip boundary condition. So no boundary layer will be developed on them. Therefore a new boundary will be developed after each cavity. Therefore the local skin friction after an air cavity is larger than when no cavity would be present. The same holds for the boundary layer next to the sides of the air cavities. This phenomenon can be modeled by the drag reduction efficiency coefficient EF. The value of EF is lower than 1 and depends on the number of cavities and their length. EF can be defined as the ratio of the actual frictional drag reduction caused by the cavities over the frictional drag reduction based solely on the reduction of the wetted area. This phenomenon is schematically illustrated for a flat plate scenario with two air cavities in figure 2.8, (Zverkhovskyi, 2014).

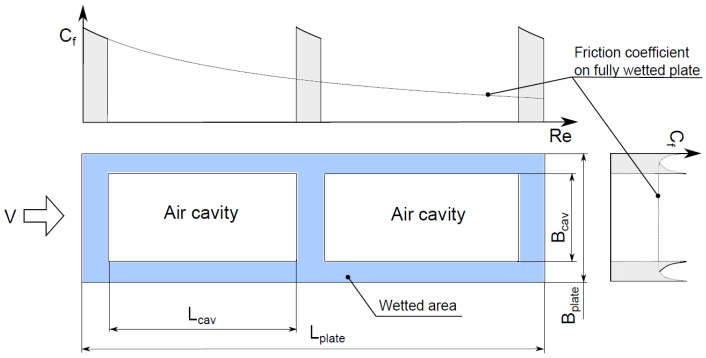

Figure 2.8: Simplified illustration of the friction coefficient distribution on a flat plate with slip areas caused by air cavities, (Zverkhovskyi, 2014).

The net drag reduction rate DR of a ship by an external air cavity system can be estimated as follows:

$$DR = \frac{R_f}{R_{tot} + R_{added}} \cdot \frac{S_{cav}}{S_{wet}} \cdot EF \tag{2.6}$$

where R_{tot} is the total drag of a bare hull, R_f is the frictional drag of a bare hull, R_{added} is the added resistance of the ALS, EF is the efficiency coefficient of the drag reduction, S_{wet} is the wetted area of the bare hull, and S_{cav} is the area covered by air cavities.

2.1.5 Power saving estimation

Several authors describe a method to quickly estimate the potential power saving of an air lubrication system, (Zverkhovskyi, 2014), (Mäkiharju et al., 2012), and (Kim & Steen, 2023). As explained in subsection 2.1.4, the drag reduction rate of an air lubrication system can be estimated by equation 2.6. This equation assumes that the cavities only affect the frictional resistance and that the wave resistance and form factor are unchanged. This assumption is usually made and is also applied for the scaling of model tests with air cavities, (Foeth, 2008). To compute the drag reduction rate, the resistance R_{tot} of the vessel without the air lubrication system should be known. Furthermore, the proportion of the total resistance that accounts for the frictional resistance should be known. The added resistance of the air lubrication system R_{added} and the efficiency of the drag reduction method is different for the different air lubrication techniques. They also depend on the vessel type and the system layout. The area covered by air cavities can be approximated from the flat bottom area of a ship. Kim and Steen (2023) provide empirical relations to estimate the flat bottom area of a ship based on the block coefficient.

The net power saving percentage $P_N[\%]$ can be computed as:

$$P_N[\%] = \frac{P_{save} - P_{comp}}{P_B} \tag{2.7}$$

with P_{save} the power saved by the air lubrication system, P_{comp} the required compressor power for the system and P_B the total brake power of the vessel. P_{comp} is usually approximated based on experiments, see e.g. Mäkiharju et al. (2012). A ship with a larger draft will require more compressor power because the compressor must overcome a larger pressure difference. If it is assumed that the air cavity system does not affect the propulsive efficiency the net power saving can be approximated as:

$$P_N[\%] = \frac{DR \cdot P_B - P_{comp}}{P_B} \tag{2.8}$$

2.2 Computational Fluid Dynamics (CFD)

CFD (Computational Fluid Dynamics) can be used to resolve the viscous flow for ship hydrodynamic applications using numerical methods. With CFD the governing equations can be resolved numerically. To do this, the fluid domain is discretized into finite volumes. Also, the time should be discretized into finite time steps. The governing equations for a ship hydrodynamic flow problem are given below.

2.2.1 Continuity

The continuity equation states that the mass of a fluid element is constant:

$$\frac{\partial \rho}{\partial t} + \nabla \cdot (\rho \underline{u}) = 0 \tag{2.9}$$

with density ρ and velocity vector $\underline{u}$. For an incompressible flow the continuity equation reduces to:

$$\nabla \cdot \underline{u} = 0 \tag{2.10}$$

It can also be written in Einstein notation, see equation 2.11. This compact formulation is also used in the next sections.

$$\frac{\partial u_i}{\partial x_i} = 0 \tag{2.11}$$

2.2.2 Momentum conservation

Momentum conservation for a fluid element is expressed by the Navier-Stoke equations (incompressible flow):

$$\rho \cdot (\frac{\partial u_i}{\partial t} + u_j \frac{\partial u_i}{\partial x_j}) = -\frac{\partial p}{\partial x_i} + \mu \cdot \frac{\partial^2 u_i}{\partial x_j \partial x_j} + F_i \tag{2.12}$$

with dynamics viscosity μ, pressure p and F_i representing a body force.

2.2.3 Two-phase flow

The free surface can be modeled using the VoF (Volume of Fluid) method. In this method, an additional transport equation is solved for the volume fraction C in each cell. $C = 1$ means that the cell is filled with water, and $C = 0$ means that it is filled with air. The interface is located within the domain between 0 and 1. Usually, the flow field in air and water is omputed simultaneously. The physical constants (density ρ and dynamic viscosity μ in each cell can be determined from the volume fraction:

$$\rho = \rho_w \cdot C + \rho_a \cdot (1 - C) \tag{2.13}$$

$$\mu = \mu_w \cdot C + \mu_a \cdot (1 - C) \tag{2.14}$$

with subscripts w and a for water and air.

2.2.4 Turbulence modeling

Various ways to numerically calculate the flow around a ship are available. First of all, the entire flow field can be computed by directly solving the Navier-Stokes equations. This method is called Direct Numerical Simulations (DNS). Performing a DNS on the scale of a ship is not possible with modern-day computers. This is because of the very small time step and mesh size required to resolve all the turbulence structures in the flow. According to Larsson and Raven (2010) the total number of grid points required for a ship is of the order of 10^{21}. Therefore this method can only be employed for research on low Reynolds number flows. To reduce the computational effort, turbulence modeling is required.

One method is to solve the flow using LES (Large Eddy Simulation) models, also referred to as, scale resolving methods. LES focuses on accurately resolving the larger, more energetic turbulence structures in the flow, while the effects of smaller-scale turbulence are modeled rather than explicitly solved. The Navier-Stokes equations are adjusted through a filtering process to separate these scales: larger eddies are directly resolved, whereas the effect of small-scale turbulence is modeled using a subgrid model which for example introduces the so-called turbulent- or eddy-viscosity. The LES method still demands significant computational resources, requiring fine meshes and small time steps. Therefore, it is currently not feasible to perform LES computations on a ship model, and certainly not on a full-scale ship for design purposes, (Larsson & Raven, 2010). For research purposes, however, LES is applied to ships. Furthermore, Rotte et al. (2023) used LES to resolve the flow in and around an external air cavity, see section 2.5.2 for a more detailed discussion. A more feasible way to compute the viscous flow around a ship is the RANS (Reynolds-Averaged Navier Stokes) method. This method is used successfully for both model scale and full-scale ships and gives reasonably accurate results, (Larsson & Raven, 2010).

RANS

The RANS (Reynolds average Navier-Stokes) equations are based on the Reynolds decomposition. This decomposition is based on the observation that flow variables in a turbulent flow can be decomposed into a mean and a fluctuating component. I.e.

$$u = \bar{u} + u' \tag{2.15}$$

with instantaneous flow velocity u, mean flow velocity $\bar{u}$ and the turbulent fluctuation u'. Substituting the Reynolds decomposition for all variables into the continuity equation and the Navier-Stokes equations and averaging over time yields the RANS equations. Continuity:

$$\frac{\partial \bar{u}_i}{\partial x_i} = 0 \tag{2.16}$$

Momentum conservation:

$$\rho \cdot (\frac{\partial \bar{u}_i}{\partial t} + \bar{u}_j \frac{\partial \bar{u}_i}{\partial x_j}) = -\frac{\partial \bar{p}}{\partial x_i} + \frac{\partial}{\partial x_j}(\mu \frac{\partial \bar{u}_i}{\partial x_j} - \rho \overline{u_i' u_j'}) + F_i \tag{2.17}$$

Due to the presence of the term $\rho \overline{u_i' u_j'}$ (the Reynolds stress) the equations cannot be closed. Additional turbulence models are required.

RANS turbulence models

Multiple turbulence models with different complexity exist. All turbulence models include empirical constants and no model capable of generating accurate results for all possible conditions has been developed. The different turbulence models can be classified into eddy viscosity models or Reynolds stress models (RSM). (Larsson & Raven, 2010)

There are linear and non-linear eddy viscosity models. The linear models are often based on the Boussinesq assumption. They assume that the Reynolds stress can be computed from the rate of strain tensor in the same way as the viscous stresses. The only difference is that the molecular viscosity is replaced by the "so-called" turbulent viscosity. The turbulent viscosity can be either computed directly (a zero-equation model) or based on one or two turbulent transport equations (one-equation or two-equation models). Zero-equation or one-equation turbulence models are hardly used in ship

hydrodynamic applications. Two-equation models, however, have been shown to give good results and are commonly used. (ITTC, 2014). Two-equation models solve two transport equations. The basic model is the $k-\epsilon$ model which solves one equation for the turbulent kinetic energy in the flow k and one for the turbulent dissipation rate ϵ. The $k-\omega$ turbulence model is also commonly applied. It uses a different definition ω for the turbulent dissipation rate in the flow. The $k-\epsilon$ and the $k-\omega$ model both have some disadvantages. Therefore the $k-\omega$ SST turbulence model can be used. This model combines the different advantages of the two models. $k-\omega$ is used in the inner region of the boundary layer, whereas $k-\epsilon$ is used in the free shear flow. This model is often used for ship-hydrodynamic applications. (ITTC, 2014)

A different class of turbulence models are the Reynolds stress models (RSM). Reynolds stress models directly solve model transport equations for all the components of the Reynolds stress tensor. RSM gives superior results compared to two-equation models. However, it also has a much larger computational cost, because more transport equations (six instead of two) should be solved. Furthermore, the solution procedure is also less stable. For these reasons, usually two-equation models are applied for ship applications. EARSM (explicit algebraic Reynolds stress models) computes the Reynolds stress based on a reduced number of transport equations. They are considered to be a reasonable compromise between costs and complexity, (ITTC, 2014). In general, Reynolds stress models are better capable of resolving anisotropic turbulence, which is e.g. present in the stern region of a ship. It is always good practice to compare different turbulence models because there is no universal good turbulence model for all applications.

2.2.5 Near-wall treatment

In CFD simulations, the boundary layer should be resolved to accurately compute the wall shear stress. However, in the near-wall region, flow variables encounter very large normal gradients. This requires proper modeling of the near-wall region. Two approaches are possible:

1. The use of near-wall turbulence models that are able to resolve the flow all the way down to the wall by using boundary conditions for the turbulence quantities at the wall. I.e. using the $\kappa-\omega$ turbulence model

2. The use of wall functions. These are semi-empirical formulations that model the flow in the inner part of the boundary layer, i.e. the so-called "Law of the Wall"

Resolving the flow all the way down to the wall requires an extremely fine mesh for full scale ship Reynolds numbers. The first discretization point should be below a dimensionless wall distance y^+ of 1, to resolve the inner part of the boundary layer. This approach often leads to an extremely high aspect ratio for the near-wall grid points. This not only results in large grids but also numerical instability problems, especially for full-scale simulations. Wall functions require less spatial resolution of the near-wall region. The first discretization point should be within the limit of validity of the wall function, which is typically a y^+ value between 30 and 500. The disadvantage of wall functions is that they are typically based on two-dimensional flow with a zero pressure gradient. Wall functions become less valid with increasing adverse pressure gradients. Therefore, a trade-off should be made between accuracy and computational effort. (ITTC, 2014).

2.3 Resistance to power

The propulsion system of a ship generates thrust using a propeller to let the ship move at a certain speed. Power is generated by the engine to overcome the ship's resistance. The three concepts that play a role when predicting the power required for a ship to sail at a certan speed are: resistance, propulsion and propeller-hull interaction. The resistance R is the force required to tow the ship at a specific speed v_s (without propulsor). The ship's resistance is the result of shear and normal stresses (pressures) exerted on the hull surface by the water flow. When the flow around a ship is resolved using CFD the resistance is divided into viscous and pressure resistance. They are computed by respectively integrating the shear stress and pressure over the ship hull. Consequently, the pressure resistance is composed of both inviscid and viscous effects. The viscous resistance computed with CFD is only due to friction.

2.3.1 Propulsion

The propeller performance can be expressed by three non-dimensional parameters: the advance ratio J, the thrust coefficient K_T, and the torque coefficient K_Q, (Klein Woud & Stapersma, 2017). The non-dimensional advance ratio J is the ratio of the advance velocity v_a to the circumferential speed $n_p \cdot D$.

$$J = \frac{v_a}{n_p \cdot D} \tag{2.18}$$

Thrust and torque can be made non-dimensional with the rotational speed n_p, the propeller diameter D and the water density ρ. This results in the thrust coefficient K_T and the torque coefficient K_Q:

$$K_T = \frac{T}{\rho \cdot n_p^2 \cdot D^4} \tag{2.19}$$

$$K_Q = \frac{Q}{\rho \cdot n_p^2 \cdot D^5} \tag{2.20}$$

The open water efficiency η_o, can be expressed in terms of these three non-dimensional parameters:

$$\eta_o = \frac{1}{2\pi} \cdot \frac{T \cdot v_a}{Q \cdot n_p} = \frac{1}{2\pi} \cdot \frac{K_T \cdot J}{K_Q} \tag{2.21}$$

In the open water diagram the thrust and torque coefficients and the open water efficiency are plotted as a function of the advance ratio J. In this diagram, K_Q is multiplied by ten so that all curves can be plotted in one diagram.

2.3.2 Propeller-hull interaction

The performance of the propeller and the ship hull are different in isolation compared to when the propeller is located behind the ship hull. This difference is due to the mutual interaction of the propeller and the hull also known as the propeller-hull interaction. This section explores the different effects that occur due to the propeller hull interaction.

Thrust deduction effect

Only a part of the thrust produced by the propeller is used to overcome the pure towing resistance of the ship. The remaining part is used to overcome the added resistance encountered when a propeller is present. The propeller increases the ship's resistance due to two effects, (Rotteveel, 2019). Firstly, the propeller creates a low-pressure field upstream and a high-pressure field downstream. This low-pressure field will, depending on the stern shape, result in additional pressure resistance. Secondly, the acceleration of the flow induced by the propeller increases friction at the stern. As a result, the required thrust T to propel a ship is larger than the resistance R of the ship in towed condition. This difference is expressed by the thrust deduction fraction (t):

$$t = \frac{k_p \cdot T - R}{k_p \cdot T} \tag{2.22}$$

The relation between thrust T and resistance R is than expressed using the trust deduction factor $(1 - t)$:

$$R = (1 - t) \cdot k_p \cdot T \tag{2.23}$$

In general, the size of the thrust deduction coefficient increases when the wake fraction increases. The magnitude of the thrust deduction factor is highly dependent on the hull shape. For a ship with one propeller, t usually lies in the range of 0.1 to 0.3. Generally, a ship with a high block coefficient C_b has a large thrust deduction fraction. For a ship with two propellers and a conventional stern shape, the thrust deduction effect will be low. This is because the suction effect of the propellers occurs further away from the hull. However, for a twin-screw ship with a twin-skeg stern shape, the thrust deduction fraction will be comparable to a ship with a single propeller. (MAN Energy Solutions, 2023).

Wake fraction

The velocity of the water at the propeller location does not equal the ship's speed. At the stern, the boundary layer of the ship has a considerable thickness. The propeller operates (partly) within this boundary layer. As a result, the advance velocity v_a of the propeller relative to the water is lower than the ship speed v_s. (Klein Woud & Stapersma, 2017). The wake fraction w represents this velocity deficit relative to the ship speed in the propeller plane. v_a is the average value of the axial velocities in the propeller plane. The difference between the ship speed v_s and the advance velocity v_a is called the wake fraction w:

$$w = \frac{v_s - v_a}{v_a} \tag{2.24}$$

The advance velocity as experienced by the propeller can be expressed in terms of the ship speed using the wake factor $(1 - w)$:

$$v_a = (1 - w) \cdot v_s \tag{2.25}$$

The propeller plane is called the wake field. Three different wake fields can be defined: the nominal wake field, the total wake field, and the effective wake field. The three wake fields will be discussed in more detail. (Carlton, 2007), (Rotteveel, 2019), (Larsson & Raven, 2010).

Nominal wake field

The nominal wake field is the velocity field in the propeller plane if no propeller is present. The nominal wake field is mainly dominated by viscous flow effects. At the stern of a ship, the boundary layer has obtained a significant thickness. As a result, the propeller plane is usually partly or even completely within the ship's boundary layer. Separated flow might also be present in the propeller plane in case high adverse pressure gradients occur in the stern section.

Total wake field

The total wake field also includes the effect of the rotating propeller behind the ship. Due to the propeller, the flow is accelerated and contracted upstream. This suppresses boundary layer growth and flow separation. A ship with an operating propeller behind it has a thinner boundary layer. Also, flow separation present in a nominal wake field might be absent in a total wake field.

Effective wake field

What matters to the propeller is the effective wake field. It is defined as the total wake field excluding the velocities directly induced by the propeller. Viscous flow effects such as the suppressed boundary layer are included in the effective wake field. As a result, velocities in an effective wake field are typically higher than those in a nominal wake field. From a propeller design perspective, the effective wake field is the most important, because this is the wake field that is experienced by the propeller and determines the blade loading. However, it is easier to determine the nominal wake field. It is used as a starting point for propeller design. Generally, the wake field quality can be assessed reasonably well based on the nominal wake field.

Hull form

There is a close relation between hull form, especially the stern shape and the wake field. Different stern shapes can result in very different wake fields. Three different ship types will be discussed: Full hull forms, slender hull forms and twin-screw vessels. (Larsson & Raven, 2010) and (Carlton, 2007) and (Dyne, 1995)

Full hull form

For full forms, e.g. a bulk carrier or a tanker, three different hull forms are generally applied. Traditionally a V-shape stern is stern is applied, which has the lowest resistance. However, its wake field is not so optimal. For such a stern shape the high wake (low velocity) is concentrated in a V-shaped region around the propeller center. Next to this, a deep wake peak is present in the top part of the

propeller disk, whereas in the lower part, the flow velocity is much closer to the freestream velocity. This gives rise to a rapidly varying angle of attack and thus to vibrations. Also, the wake fraction will be low.

A U-shape stern has a better axisymmetric wake distribution and a higher wake, compared to a V-shape stern. This is because a bilge vortex is present for a U-shape stern. The bilge vortex collects the frictional wake from all parts of the ship boundary layer and concentrates it in the propeller plane. For creating a more uniform wake field careful design of the stern shape is required to suitably position the bilge vortex. A bulbous stern shape has an even stronger bilge vortex. However, the big disadvantage of U-shaped and bulb-shaped sterns is that they have a higher resistance. This is because a vortex requires energy. Although such stern shapes result in a higher hull efficiency they will thus not cause a reduction in propulsive power compared to a V-shape stern. The main advantage of su

Slender hull form

A slender hull form with a single-screw configuration is typically applied to container ships and RoRo vessels. Compared to a full stern shape, such vessels have a less homogeneous wake. Furthermore, the mean wake is also lower, meaning that such vessels have a lower hull efficiency. Again the wake can be made more uniform by changing the stern shape from a V-shape to a more U-shaped or bulb-shaped stern. In other words by introducing or increasing the strength of a bilge vortex. (Larsson & Raven, 2010)

Twin screw

The wake of a twin screw vessel is rather different than that of a single screw vessel. First of all it is asymmetric, in contrast to a single screw vessel. Furthermore, the hull boundary layer will only partially pass through the propeller disk. As a result, the velocity deficit in the propeller plane is low, resulting in a low wake fraction and hull efficiency. Next to this, the propeller wake is disturbed by the wake of the shaft support struts and by the wake of the shaft itself.

Hull efficiency

The wake and the thrust deduction effect can be combined together into the hull efficiency η_h, which is defined as the ratio of the effective power P_E over the thrust power P_T, see also equation 3.9. The effective power P_E is defined as the power needed to overcome resistance R at speed v_s, see equation 2.26. The power as delivered by the propeller in water moving at velocity of advance v_a with useful output T is the thrust power P_T (per propeller), see equation 2.27. If the wake fraction exceeds the thrust deduction fraction the hull efficiency can exceed unity. This often happens, especially for single-screw vessels. This is the reason why the propeller is usually positioned aft of a vessel. The propeller positioned aft allows winning back energy from the boundary layer, due to the propeller operating in the viscous wake of the ship. (Klein Woud & Stapersma, 2017). Table 2.1 shows typical self-propulsion factors for different propeller arrangements, (MAN Energy Solutions, 2023). In general for a single-screw vessel the hull efficiency increases with the block coefficient.

$$P_E = R \cdot v_s \tag{2.26}$$

$$P_T = T \cdot v_a \tag{2.27}$$

$$\eta_h = \frac{P_E}{k_p \cdot P_T} = \frac{R \cdot v_s}{k_p \cdot T \cdot v_a} = \frac{1-t}{1-w} \tag{2.28}$$

Table 2.1: Typical self-propulsion factors, (MAN Energy Solutions, 2023).

Propeller arrangement	**Wake fraction** w	**Thrust deduction fraction** t	**Hull efficiency** η_h
Single-screw	0.20-0.45	0.10-0.30	1.1-1.3
Twin-screw, single skeg	0.10-0.25	0.05-0.15	0.95-1.15
Twin-screw, double skeg	0.15-0.35	0.05-0.025	1.05-1.25

Relative rotative efficiency

Normally the performance of a propeller is tested in a so-called open water test. In the open water test, the propeller is tested with uniform inflow. In reality, the propeller is located behind the ship's hull. The propeller torque measured in an open water test is slightly different from that when the propeller is behind the ship hull, for an equal thrust production in both cases. This is due to the non-uniform incoming velocity field. This difference is expressed by the relative rotative efficiency η_r. Usually, the relative rotative efficiency is very close to unity, (Klein Woud & Stapersma, 2017).

2.3.3 Power prediction

The power that should be delivered to all the propellers to let the ship sail at speed v_s is defined as the delivered power P_D:

$$P_D = \frac{R \cdot v_s}{\eta_h \cdot \eta_o \cdot \eta_r} = \frac{R \cdot v_s}{\eta_d} \tag{2.29}$$

All losses that are present in the ship propulsion can be combined into the propulsive efficiency η_d:

$$\eta_d = \eta_h \cdot \eta_o \cdot \eta_r \tag{2.30}$$

The delivered power is not equal to the required engine power. Additional losses occur in the transmission line, e.g. at shaft bearings or at the gearbox. For this thesis, however, the investigation is limited to the delivered power, because the engine and shaft line configuration can be different for each ship, e.g. podded propulsion, multiple engines, etc.

2.4 Shallow water

First of all, it should be clear what is exactly meant by the term "shallow water" and other definitions. The definitions given by the International Towing Tank Conference (ITTC) are used, (ITTC, 2021). The flow around a ship can be restricted in both vertical and lateral directions. This leads to the following definitions:

- Shallow water: Restrictions in vertical direction (finite water depth);
- Restricted water: Restriction in lateral direction (e.g. other ships, banks, harbor);
- Confined water: Restrictions in both vertical and lateral direction (e.g. a river or channel);

Multiple authors describe boundaries for when the water should be considered deep or shallow. According to ITTC (2021), if at least one of the following two indicators has been reached, shallow water effects have to be considered:

- Depth-based Froude number $Fr_h = \frac{V}{\sqrt{g \cdot h}} > 0.5$
- Water-depth to ship-draft ratio $H/T < 4.0$

where V is ship's speed, g the gravitational acceleration, h the water depth, and T the ship's draft.

2.4.1 Wave properties

In shallow water, the general properties of gravity waves are different than in deep water, (Larsson & Raven, 2010). In this section, the most important differences are highlighted. The relations given can be derived from potential flow theory. The gravity waves are assumed to be linear, which is valid for waves with small amplitudes. From potential flow theory, the dispersion relation for a finite water depth can be derived. It gives a relation between the wave propagation speed c and the wavelength λ:

$$c = \sqrt{\frac{g \cdot \lambda}{2\pi} tanh(\frac{2\pi \cdot h}{\lambda})} \tag{2.31}$$

The dispersion relation can also be written in dimensionless form:

$$\frac{c}{\sqrt{g \cdot h}} = \sqrt{\frac{\lambda}{2\pi \cdot h} tanh(\frac{2\pi \cdot h}{\lambda})} \tag{2.32}$$

The dispersion relation in dimensionless form is a function of λ/h only. This relation is plotted in figure 2.9. The figure shows that the wave velocity approaches a limiting value for decreasing water depth (increasing λ/h):

$$c = \sqrt{g \cdot h} \tag{2.33}$$

The equation shows that the wave speed is independent of the wavelength in shallow water (h going to zero). This means that all waves run at the same speed. For the deep water case (h going to infinity) it can be derived from the dispersion relation that the wave speed is independent of the water depth:

$$c = \sqrt{\frac{\lambda \cdot g}{2\pi}} \tag{2.34}$$

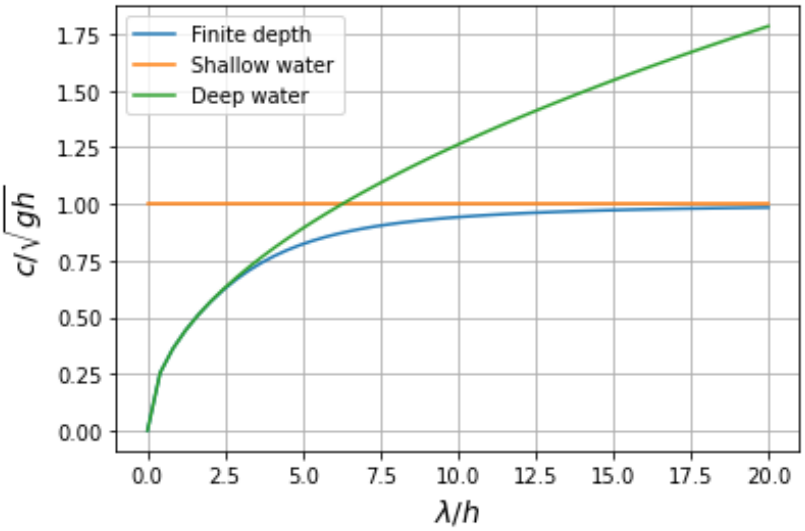

Figure 2.9: The dispersion relation in dimensionless form.

In general, wave energy does not travel at the same speed as wave propagation speed. In deep water, the group velocity c_g (energy transport velocity) of a wave equals half the wave propagation velocity c:

$$c_g = \frac{c}{2} \tag{2.35}$$

For a finite water depth, the group velocity is also a function of the water depth. The general relation between group velocity and wave propagation speed is:

$$\frac{c_g}{c} = \frac{1}{2} \cdot (1 + \frac{4\pi \cdot h/\lambda}{sinh(4\pi \cdot h/\lambda)}) \tag{2.36}$$

This equation shows that for λ/h approaching infinity the group velocity becomes equal to the wave speed.

2.4.2 Different resistance components and effects

The shallow water effects on ship resistance are the most important from the perspective of air lubrication. There are multiple shallow water effects on ship resistance. Moreover, different resistance components have different physical bases. Therefore studying the shallow water effects of the various resistance components separately can help to gain a better insight.

In shallow water, the shear stress and the pressure distribution along the ship hull, as well as the ship-generated waves are influenced by the limited water depth. The three main resistance components

that are related to these physical phenomena are the frictional resistance (shear stress), the viscous pressure resistance (pressure), and the wavemaking resistance (waves). In addition, also the trim and sinkage of the ship are affected by the finite water depth. (Zeng, 2019).

Viscous resistance

The effect of water depth on the viscous flow is an increased flow velocity along the hull and larger pressure gradients. If the flow gets more shallow the flow is forced to pass along the sides of the hull rather than under the bottom. As a result, the flow will follow a more horizontal path. Usually this results in more streamline curvature and larger pressure gradients. The frictional resistance is larger due to the increased flow velocity. The viscous pressure resistance increases due to the changed pressure distribution. This is expressed by a larger form factor. Furthermore, due to the larger pressure gradients, the ship's boundary layer thickness increases. This can lead to flow separation at the stern. The magnitude of all the effects described above mainly depends on the ratio H/T (water depth to draft ratio). For a smaller H/T value the effects will be more pronounced. Then the shape of the hull form also gets more important. (Zeng, 2019) and (Raven, 2022)

Trim and sinkage

A ship sailing in shallow water will have a higher dynamic sinkage than a ship sailing in deep water. Due to the proximity of the bottom, the flow speed past the vessel increases. The increased flow speed causes a decrease in pressure under the hull. As a result, the dynamic sinkage of the vessel will increase. (Larsson & Raven, 2010). The changed pressure distribution under the hull also leads to a trimming moment. Vessels with a high block coefficient will usually have a bow-down trimming moment. More slender vessels will usually have a stern-down trimming moment. This can be different depending on the hull form of a specific vessel. (van den Bosch, 2010). The combined phenomena of sinkage and trim in shallow water is known as squat. The increase in sinkage and trim causes an additional increase in resistance, (Raven, 2022). The squat effect is illustrated in figure 2.10, (Marine Insight, 2023).

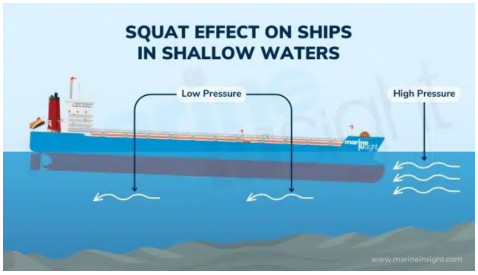

Figure 2.10: The squat effect, (Marine Insight, 2023).

CFD in shallow water

The squat effect might cause some trouble when performing numerical simulations of a ship sailing a shallow water. For a normal CFD simulation of a ship sailing in deep water the trim and sinkage of the vessel are solved, to allow the vessel to move to its dynamic equilibrium position. Due to the squat effect in shallow water, the ship can have excessive sinkage and trim. Consequently, high mesh deformation between the ship's bottom and the sea floor can occur. This can lead to over-thinning of these cells, resulting in cells with negative volume. A possible solution is to estimate the trim and sinkage beforehand using e.g. empirical relations. The mesh can then be created at the estimated trim and sinkage position of the vessel.

Wavemaking resistance

The dominant parameter for the wave making resistance is the depth Froude number Fr_h. For low values of Fr_h the effect of the water depth on the wave making resistance is limited. For Fr_h approaching 1.0 (critical speed) the waves become longer than in deep water and the wave resistance increases. The kelvin angle also increases to 90 degrees at the critical speed. Close to the critical speed, the wave resistance increases strongly depending on the strength of the transverse waves (and thus on the ship's

properties). Above the critical speed the wavemaking resistance decreases. Larsson and Raven (2010) distinguish 4 different flow regimes based on Fr_h

2.4.3 Different flow regimes for waves in shallow water

The different properties of gravity waves in shallow water inevitably cause a change in the wave pattern generated by a ship. Larsson and Raven (2010) distinguish multiple flow regimes. These flow regimes can be classified based on the depth-based Froude number Fr_h:

$$Fr_h = \frac{V}{\sqrt{g \cdot h}} \tag{2.37}$$

Low subcritical: $Fr_h < 0.7$

In this flow regime, no change in the shape of the ship wave pattern can be observed. However, the wave amplitudes can increase. Furthermore, there can be other shallow water effects present. Also for a low depth Froude number, the keel clearance of a vessel can be small. As a result, the above-described shallow water effects on the viscous resistance, trim, and sinkage can occur. These effects mainly depend on the water depth to draft ratio (H/T) rather than on the depth-based Froude number.

High subcritical: $0.7 < Fr_h < 0.9$

For higher depth Froude numbers the effects occurring in the low subcritical flow regime get more pronounced. However, also another shallow water effect will occur. Now, the wave pattern shape will change as well. For the same wave speed, the wave length of a gravity wave will increase with decreasing water depth. This can be found from the dispersion relation, see equation 2.31. Figure 2.9 shows that the difference between deep and shallow water waves increases with an increasing value of λ/h. This means that the longest wave components will change first. For a ship, with increasing depth Froude number the transverse waves will get longer first, while the shorter diverging wave components are still unaffected.

For all ships, the wave pattern is contained within the so-called Kelvin wedge. The angle of the Kelvin wedge is determined by the ratio of the group velocity to the wave propagation velocity. This ratio equals 0.5 in deep water and increases in shallow water, as described in section 2.4.1. As a result, the width of the Kelvin wedge increases in shallow water. At $Fr_h = 1$ the angle will be 90 degrees.

(Trans)critical: $0.9 < Fr_h < 1.1$

In the critical flow regime, the shallow water effects can be dramatic. At the critical speed, reached at $Fr_h = 1$ the transverse waves (which move at the ship's speed) move at the maximum wave speed of $\sqrt{gh}$, see equation 2.33. The wavelength of the transverse waves is now no longer dependent on the ship's speed. Consequently, a regular wave pattern of transverse waves with constant length is not necessary and the transverse wave system might not be steady and stable. In addition to this, the wave group velocity equals the wave speed at the critical speed, so the wave energy is kept in the wave itself where it is generated. Energy is continuously fed into this wave, so it can grow strongly. This can lead to a very large increase in resistance, trim, and sinkage.Most displacement ships are not able to pass the critical speed because they have not enough power or because of hitting the bottom. At the critical speed only the transverse waves are critical. The divergent wave components are shorter and slower and are therefore not critical. Therefore, ships that mainly generate diverging waves, e.g. fast ships, are much less influenced and can pass the critical speed.

Supercritical: $Fr_h > 1.0$

In the supercritical range, the ship speed is larger than the maximum wave propagation speed so transverse can no longer exist. The ship's wave pattern will only consist of diverging waves. This leads usually to a significant decrease in trim and sinkage of the vessel. Furthermore, the ship's resistance is generally lower in the supercritical regime than in deep water.

2.4.4 Propulsion

What matters in the end for ship performance is the delivered power and not only the resistance. Therefore the shallow water effects on the propulsive efficiency η_D should be known. In shallow water, the wake fraction and the thrust deduction fraction are changed. Furthermore, the working point of the propeller changes, which affects the propeller open water efficiency.

Raven (2022) developed a novel correction method for shallow water effects on ship speed trials. This method was also adopted recently by the ITTC and the ISO guidelines for ship speed trials.. The report of the "Raven method" states that little information is available in literature on shallow water effects on propulsion. Some general effects are known, however.

Regarding the propeller-hull interaction both the wake fraction and the thrust deduction effectchange in shallow water. The thrust deduction accounts for the action of the propeller pressure field on the ship's stern. It is expected that the thrust deduction will increase in shallow water. The reason for this is that the propeller pressure field will extend to greater distances. In general an increase in viscous resistance results in an increase of the wake fraction. This means that the wake fraction will increase when the water depth decreases. In the depth range relevant for sea trial corrections it is most likely that the wake fraction is more sensitive to H/T than the thrust deduction fraction. As a result, the hull efficiency would slightly increase.

It is unknown how shallow water affects the relative rotative efficiency. For small H/T the wake field might change substantially. This could affect η_r. For the depth range relevant for sea trials the change in η_r is most likely negligible.

Regarding the propeller open water efficiency, two effects are present. There is an increase in thrust due to the resistance increase in shallow water. Next to this, the propeller inflow speed is reduced due to the increased wake fraction. Both effects increase the propeller loading, which usually causes a decrease in efficiency.

The increase in hull efficiency and the decrease in open water efficiency oppose each other. Most likely the change in propulsive efficiency is much smaller than the resistance increase in shallow water. The shallow water effect on propulsive efficiency depends on the water depth, but also on the hull form, especially the stern shape. In the end, the sea trial shallow water correction method of Raven does not include a correction for the change in propulsive efficiency, because too little data is known. Older correction methods for sea trials also assume a constant propulsive efficiency. Also the research of Zeng (2019) on ship resistance prediction in shallow water recommends more research on shallow water effects on the propulsive efficiency.

2.5 Numerical modeling of air cavities

Multiple attempts have been made in literature to model the flow around air lubricated ships numerically. This thesis focuses on external air cavities. Therefore, the discussion is limited to the numerical modeling of external air cavities. For more information on the numerical modeling of other air lubrication techniques (such as air layer drag reduction and internal air cavities) see e.g. Cucinotta et al. (2018), Mukha and Bensow (2020), and Shiri et al. (2012).

2.5.1 Two-phase RANS

Two-phase simulations of external air cavities were first performed by Zverkhovskyi et al. (2015). He investigated a single air cavity on a 2D flat plate. The VoF method was used to model the two-phase flow. Several problems occurred. It was found that the cavity size could not be simulated correctly at a given air injection rate because the air leakage from the end cavity is not modeled correctly with the used numerical approach. The same problem occurred for 3D simulations. As a result, the pressure in the cavity cannot be established correctly for a fixed air injection rate. He suggests that improving the volume fraction transport equation by adding a diffusion term could help to model the closure region more accurately.

The numerical modeling of (the closure region of) external air cavities is studied in more detail by Rotte et al. (2016). Again a single 2D cavity on a flat plate is studied. She states that the key to the numerical prediction of the air layer characteristics lies in the correct modeling of the closure region. Therefore the closure region and the corresponding flow physics in that region are studied in more

detail. Two main mechanisms responsible for air losses in the cavity closure region are identified: the re-entrant jet and wave pinch-off mechanisms, see also subsection 2.1.4.

The re-entrant jet mechanism can be modeled using RANS-VoF methods. However, it was found that the commonly used two-equation turbulence models, such as the $k-\epsilon$ and the $k-\omega$ models show serious deficiencies for the modeling of the shedding mechanisms for air cavities. These methods were originally developed for single-phase RANS simulations. In two-phase simulations, they can over-predict the eddy-viscosity in and downstream of the cavity closure region. This could prevent the development of the re-entrant jet. It was found that this problem remained after including an eddy-viscosity correction model, (Rotte, Kerkvliet, & van Terwisga, 2018). Rotte et al. (2017) suggests that using a Reynolds stress model instead of a two-equation turbulence model could solve the problem. Barbaca et al. (2017) was also able to model the re-entrant jet formation in the closure region of an external air cavity. The wave pinch-off mechanism is governed by waves formed by turbulence structures hitting the air-water interface. These mechanisms cannot be simulated with a RANS solver. A scale-resolving or a hybrid turbulence model is required. (Rotte et al., 2019).

Next to this also problems occur with the VoF method, used for modeling the air-water interface. An unphysical thin air layer is observed in the closure region and downstream of the cavity. An example is visible in figure 2.11. As a result, the wall shear stress and consequently the friction drag reduction of the air cavity cannot be accurately predicted. It is hypothesized that a different flow model is required for modeling the multiphase flow in the closure region. This could be a more complex VoF model that uses a geometrical reconstruction of the interface, a Level-Set approach, or an Eulerian multiphase model, (Rotte et al., 2019). This problem is also observed for LES simulations of the air cavity, (Rotte et al., 2023).

In the end, it was concluded that RANS-VoF methods are capable of predicting velocity profiles at different stream-wise locations in the boundary layer around the cavity. However, the required air flow rate cannot be predicted. There are two reasons for this. First of all, not all air loss mechanisms can be modeled using the RANS flow model. Secondly, the VoF method, used for modeling the air-water interface, is incapable of modeling the multi-phase flow in and downstream of the air cavity. (Rotte et al., 2019).

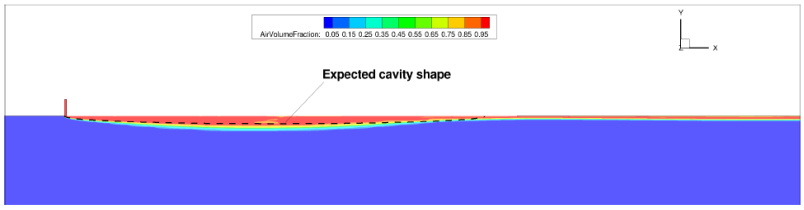

Figure 2.11: A 2D air cavity on a flat plate simulated using the RANS VoF method, (Zverkhovskyi et al., 2015).

2.5.2 Scale resolving simulations

Scale-resolving simulations were also performed to get a better understanding of the flow dynamics in the closure region of air cavities. As explained earlier a RANS flow model cannot resolve all air loss mechanisms in the closure region of an external air cavity. Rotte, Charruault, et al. (2018) examined hybrid RANS-LES simulations for modeling external air cavity flows. It was found that these simulations showed a more realistic cavity interface and closure behavior than RANS simulations. However, the cavity profile was very sensitive to the upstream velocity profile of the boundary layer. Furthermore, the way the hybrid model switches between RANS and LES inside the air cavity also posed problems.

Rotte et al. (2023) also performed LES simulations of an external air cavity. It was found that velocity profiles downstream of the air cavity computed with LES show better agreement with experimental results than RANS results. Moreover, a third air loss mechanism was identified that was not observed in RANS simulations. This third mechanism is the ligament stretching mechanism. It is governed by viscous forces in the water phase that stretch out gas ligaments. The ligaments break up due to instabilities and are transported away from the cavity by the water flow. Also with LES simulations, the air-water interface could not be modeled correctly. Similar problems occurred as with

the earlier described 2-phase RANS simulations.

From this, it can be concluded that, of all the above-described numerical methods, scale-resolving models provide the most accurate representation of air cavities, (Rotte et al., 2023) and (Mukha & Bensow, 2020). Rotte et al. (2016) states that from a practical point of view, however, scale-resolving models are not believed to be viable for practical ship design purposes yet, due to the significant amount of added computational time. These models can however first be used to identify the physical conditions in the closure region and to study and identify scaling influences. Thereafter, one could develop a RANS model for the numerical modeling of air cavities. Furthermore, more research is required to improve the two-phase flow modeling in the closure region of the cavity.

2.5.3 Single phase RANS

Due to the high computational cost and the challenges faced with 2-phase flow modeling of air cavities, simulations with a single-phase flow model are also performed. Zverkhovskyi et al. (2015) modeled the air cavities as surfaces with a slip boundary condition. For a known cavity shape on a flat plate, he could compute the velocity profiles in the boundary layer around the air cavity and the drag reduction rate. The computations showed good agreement with experimental results (PIV measurements) of the same air cavity.

Zverkhovskyi (2023) also studied the resistance reduction by air cavities applied on an inland waterway vessel with this approach, see figure 2.12. The cavity thickness was neglected and also the cavity shape was idealized. In this way, the skin friction and boundary layer development along the vessel hull could be modeled. The simulations were not validated.

The single-phase approach also has some drawbacks, (Rotte et al., 2019). The cavity shape should be known before performing the simulations. Next to this, in the closure region of the air cavities, the cavity surface is highly unstable and unknown. Furthermore, to compute the required air flux for the air cavities, a two-phase flow approach is needed.

From this, it can be concluded that modeling the air cavities as slip surfaces is a promising approach with relatively low computational cost. However, the cavity shape should be known, the required air flux cannot be computed, and the cavity shape is simplified. More validation for the application of this method to ships is required. (Zverkhovskyi, 2023)

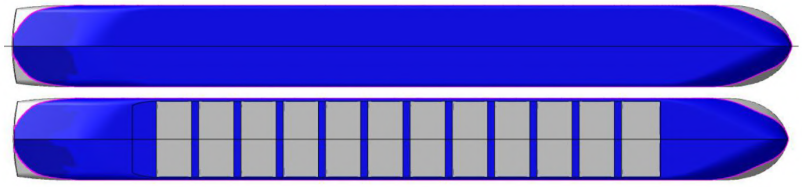

Figure 2.12: Bottom view of an inland vessel. Top is the reference model; bottom is with the patches representing air cavities with a slip boundary conditions (grey), (Zverkhovskyi, 2023).

2.6 Air lubrication and propeller performance

2.6.1 Possible air leakage

An often-heard concern of air lubrication systems is that air (bubbles) might leak flow into the propeller and deteriorate its performance

Kawakita (2013) found that the propeller efficiency is decreased in a bubbly flow. This decrease is due to a reduction of the local flow density and due to the increased non-uniformity of the wake. Secondly, air leakage into the propeller might also impact the cavitation behavior of the propeller, (Li et al., 2022).

However, Kawakita (2013) states that for an air-lubricated ship the void fraction at the propeller disk is relatively low (less than 1%). Therefore in practice for air-lubricated ships, the decrease of propeller efficiency and the change of pressure fluctuations of the propeller will be negligible. This claim is also supported by (Mäkiharju et al., 2012). Furthermore as noted by (Pavlov et al., 2020), commercial companies such as Mitsubishi, Silverstream, and Samsung have not reported problems with bubble stream interaction with propellers.

2.6.2 Propeller hull interaction

Multiple authors observed that a vessel with air cavities has a lower hull efficiency because the wake fraction is reduced. The physical interpretation for the lower wake fraction is that a friction reduction (due to air cavities) is always associated with changes in the hull boundary layer and wake. The presence of the surfaces with the slip boundary condition along the ship's bottom does not allow the boundary layer to grow as it happens in the reference case (the vessel without air cavities). As a result, the boundary layer will be thinner which causes a higher axial velocity in the propeller plane. (Sverchkov & Borusevich, 2019), (Gorbachev & Amromin, 2012) (Amromin, 2016), (Wu et al., 2020) (internal air cavities), and (Zverkhovskyi, 2023) (external air cavities).

Sverchkov and Borusevich (2019) found that flow separation at the stern of a high block coefficient was reduced by the internal air cavity. This resulted into a more uniform wake field. A more uniform wakefield was also observed by Wu et al. (2020).

Furthermore, Wu et al. (2019) and Arakawa et al. (2018) found that an air lubrication system also slightly affects the thrust deduction effect. However, this effect is insignificant according to Gorbachev and Amromin (2012) and Hoang et al. (2009).

Lastly, Wu et al. (2019) and (Wu et al., 2020) state that the propeller efficiency will also change for an airlubricated ship. The propeller working point is changed due to the resistance reduction.

2.7 Air lubrication in shallow water

Little research has been performed on the performance of air lubrication systems in shallow water. Only a few observations have been made in literature. Experimental research on external air cavities on a flat plate, by Zverkhovskyi (2014), showed that the shallow water effect might substantially increase the cavity length. The experiments were performed in a cavitation tunnel. It was found that the finite channel depth affects the cavity length. As described earlier, this research showed that the maximum stable cavity length L_{cav} equals half a gravity wavelength. L_{cav} can then be computed by substituting $L_{cav} = \lambda/2$ into the deep water dispersion relation (eq. 2.34:

$$V = \sqrt{\frac{\lambda \cdot g}{2\pi}} \tag{2.38}$$

The same can be done for the shallow water dispersion relation (see eq. 2.31. This gives an implicit relation for the maximum cavity length in shallow water:

$$V = \sqrt{\frac{L_{cav} \cdot g}{\pi} tanh(\frac{\pi \cdot h}{L_{cav}})} \tag{2.39}$$

Equation 2.39 can be solved numerically to find L_{cav} as a function of water depth and flow speed. In figure 2.13 The cavity length in shallow water over the cavity length in deep water is plotted as a function of the depth-based Froude number. The figure shows that for $Fr_h < 0.61$ the increase in length is less than 1% and thus negligible. For $Fr_h = 0.77$ the cavity length is 10% larger than in deep water. Lastly, for $Fr_h > 1$ the flow gets supercritical. In that case, the cavity length is no longer dependent on the flow speed; theoretically, the cavity length then approaches infinity. However, in practice, the cavity length will be limited by the length of the flat bottom of the ship.

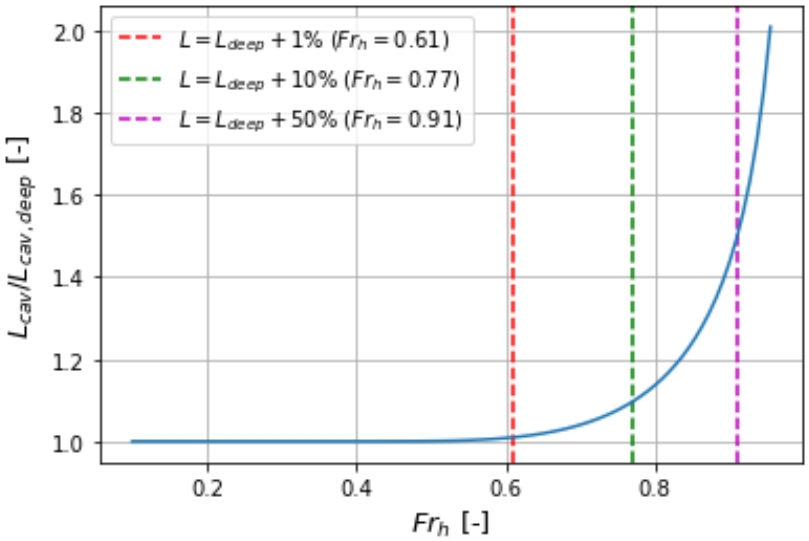

Figure 2.13: Cavity length increase in shallow water as a function of the depth-based Froude number.

Furthermore, model tests of a vessel with a large internal cavity in shallow water were performed by Galushina et al. (2020). It was found that the drag reduction is different compared to deep water. A larger drag reduction than in deep water was observed but in a narrower speed range. Above a certain speed, the cavity caused a drag increase rather than a drag decrease. This effect is even more pronounced in confined waters. During model tests on a vessel with the DACS system in shallow water, a larger drag reduction rate was measured, compared to deep water. However, only very few measurements were obtained. Gorbachev and Amromin (2012) point out that an external air cavity system has a drawback in shallow water. The skegs mounted to the bottom of the hull will limit the draft of the vessel. As a result, the cargo-carrying capacity of the vessel is reduced. Therefore the skeg height should be as low as possible for vessels operating in shallow water.

Chapter 3
Methodology

This chapter describes the methodology of the modeling method used in this thesis. For all ships three cases are relevant:

- Reference case: The ship before the installation of the DACS system
- Air off: The ship including the appendages of the DACS system but without air flow
- Air on: The ship including the appendages of the DACS system with air flow

To study all three cases, modeling of the air cavities and of the appendages is required, this is described first. Afterwards, it is explained how a power prediction is made for all ships. Lastly, the setup of the CFD simulations is described.

3.1 Air cavity modeling

Based on the literature review presented in section 2.5, it can be concluded that it is currently not feasible to accurately predict the two-phase flow around a vessel with external air cavities. A promising and the most viable alternative is to model the air cavities as surfaces with a slip boundary condition, see (Zverkhovskyi, 2023). However, this requires an approximation of the shape of the air cavities. Section 2.1.4 explains in detail how the cavity length can be approximated. This method will be applied in all cases in this research unless explicitly stated. For the air cavities, a constant aspect ratio of 60 is assumed, as observed by Zverkhovskyi (2014). The air cavities are modeled as flat rectangular surfaces. The appendages of the air cavity system are not included. Their added resistance is included later, see also section 3.2. This approach was also used by Zverkhovskyi (2023). It should be noted that in reality, the air cavities have a 3D shape. Modeling the air cavities in 3D would also require modeling all the system appendages in detail. This would result in a very fine mesh and a high computational cost, see also section 3.2. Furthermore, a typical aspect ratio of an air cavity (length over thickness ratio) is approximately 60, see section 2.1.4. This means that the thickness of the cavity is small compared to its length. Therefore it seems justified to model the cavities as flat surfaces. Rotte et al. (2019) points out that in the in the closure region of the air cavities, the cavity surface is highly unstable and unknown, see also figure 3.1. However, it should be noted that the closure region only covers a fraction of the total cavity area, so modeling the cavity surface as rectangular is close to reality.

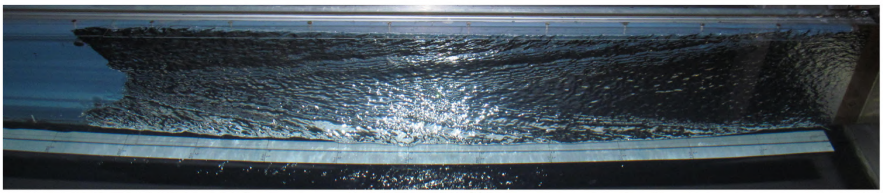

Figure 3.1: Air cavity with an irregular shape in the closure region, (Zverkhovskyi, 2014).

3.2 System appendages

The appendages of the DACS system, the skegs, and the cavitators, also cause an additional increase in resistance. This should also be modeled. Figures 3.2 show a figure of the actual appendages installed on the general cargo ship. The added resistance is different for air on and air off. With air off, there will be flow separation in front and behind the cavitators as they are just steps in the flow. With air on a cavity is formed behind each cavitator, consequently, the flow is only separated in front of each cavitator. Furthermore, with air on, the sides of the skegs are partially covered with air due to the thickness of the air cavities. Therefore, the added resistance of the appendages will be lower with air on.

In this research, the appendages are not included in the CFD simulations with air on. It would be most accurate to model the 3D air cavities as 3D surfaces with a slip boundary condition and also include the appendages in the CFD simulations. However, this would require an approximation of the 3D shape of the cavities, which is also uncertain but not impossible. Moreover, a very fine mesh would be needed to accurately resolve the flow around the appendages, especially for the cavitators which are much smaller than the skegs, see also figure 5.5. In case the cavitators are included, it should also be investigated if the flow separation of the cavitators is correctly resolved with the applied turbulence model and wall functions. This would require considerable effort and is also not directly related to the project's scope. Therefore the appendages are modeled in a more simple way.

The appendages are not included in all CFD simulations with air on. Rather, the resistance of the appendages with air on is approximated and added to the resistance computed with CFD. This approach was also used by Zverkhovskyi (2023). For all ships, the added resistance is estimated or modeled differently. This is described separately for each ship. In the CFD model, the air cavities are placed directly next to each other, without them being separated by the skegs. It should be noted that as a result, the actual air-covered area is slightly lower than when the skegs would have been included. However, for all ships, this difference in air-covered area is less than 1% and therefore negligible. Furthermore, the appendages could also influence the wake field and the thrust deduction effect. This effect is neglected. For the general cargo ship it was observed that the skegs only have little impact on the wake field and thrust deduction effect, see section 5.5. It should be noted that the modeling method of the cavities and appendages is a simplified and pragmatic approach designed to facilitate an initial study. This method can always be reviewed and refined as necessary in the future.

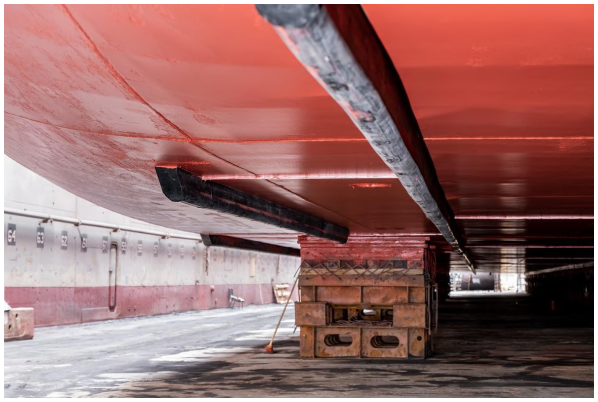

Figure 3.2: DACS appendages installed on the general cargo ship, (Damen Shipyards Group, 2023).

3.3 Shaft power prediction

For all three case studies, a shaft power prediction is made. This is done in the following way: The shaft power prediction is made for the ideal trial condition. This allows for comparison with sea trial and extrapolated model test results. Therefore the resistance R, predicted using CFD, should be corrected for hull roughness and wind resistance. This can be done in the following way: First of all the total resistance coefficient C_T should be computed:

$$C_T = \frac{R}{0.5\rho v_s^2 S_{wet}} \tag{3.1}$$

The CFD simulations are all performed on a smooth hull without roughness. However, the actual ship will have some roughness. This can be corrected by adding a roughness resistance coefficient ΔC_{rough} to the total resistance coefficient. The roughness resistance can be approximated using the Townsin's formula:

$$\Delta C_{rough} = 0.044 \cdot \left(\left(\frac{AHR}{L_{pp}} \right)^{1/3} - 10Re^{-1/3} \right) + 0.000125 \tag{3.2}$$

where AHR is the average hull roughness. For EEDI and delivery trials, a value of 150 μm should be applied, (ITTC, 2017c). Furthermore, an actual sailing ship also encounters wind resistance. This is

not modeled in the CFD simulations. The wind resistance coefficient ΔC_{air} can be computed as:

$$\Delta C_{air} = C_x \frac{\rho_{air}}{\rho_{water}} \cdot \frac{A_T}{S_{wet}} \tag{3.3}$$

with C_x the coefficient of axial wind force, A_T the dry projected frontal area of the hull and S_{wet} the wetted area of the hull. C_x is assumed to be 0.8, which is in line with the ISO guidelines for sea trials for this ship type, ("ISO 15016: Guidelines for the assessment of speed and power performance by analysis of speed trial data", 2015). A_T is approximated from the drawings of the ship. The corrected resistance R_{cor} can then be computed using equation 3.4. Note that the wetted area is reduced by the air cavities when the air lubrication system is on. In that case, the roughness correction is applied to the reduced wetted area:

$$R_{cor} = (C_T + \Delta C_{rough} \cdot \frac{S_{wet} - S_{cav}}{S_{wet}} + \Delta C_{air}) \cdot 0.5 \rho v_s^2 S_{wet} \tag{3.4}$$

As explained earlier the added resistance of DACS appendages ΔR_{DACS} are not included in the CFD simulations with air on. All results presented for resistance R do not include any corrections. The added resistance is added afterward. Therefore for the case with air on the corrected resistance R_{cor} is defined as:

$$R_{cor} = (C_T + \Delta C_{rough} \cdot \frac{S_{wet} - S_{cav}}{S_{wet}} + \Delta C_{air}) \cdot 0.5 \rho v_s^2 S_{wet} + \Delta R_{DACS} \tag{3.5}$$

3.3.1 Power calculation

The delivered power P_d can then be computed using equation 3.6. For this computation the hull efficiency η_h, the relative rotative efficiency η_r and the propeller open water efficiency η_o are required. For a fixed pitch propeller the propeller open water efficiency η_o can be obtained from the propeller open water diagram. For each ship speed a $K_{T,ship}$ can be constructed using equation 3.7. The propeller working point is located at the intersection point between the $K_{T,ship}$ curve and the propeller K_T curve in the open water diagram. η_o can be read from the advance ratio at the propeller operating point. The general cargo ship has a controllable pitch propeller so a different approach is used for that case, see section 5.2.

$$P_d = \frac{R_{cor} \cdot v_s}{\eta_h \cdot \eta_r \cdot \eta_o} \tag{3.6}$$

$$K_{T,ship} = c_7 \cdot J^2 \tag{3.7}$$

$$c_7 = \frac{R_{cor}}{\rho \cdot D^2 \cdot k_p \cdot (1-t) \cdot (1-w)^2 \cdot v_s^2} \tag{3.8}$$

The relative rotative efficiency η_r cannot be obtained from the CFD results. However, η_r is usually close to 1.0. Therefore it is often and also in this case assumed to equal unity. (Klein Woud & Stapersma, 2017). The hull efficiency can be computed from the thrust deduction fraction and the wake fraction, see equation 3.9. The thrust deduction fraction is computed using the actuator disk model. The wake fraction is approximated from the nominal wake field. Both assumptions are elaborated in the subsequent sections.

$$\eta_h = \frac{(1-t)}{(1-w)} \tag{3.9}$$

3.3.2 Actuator disk model

The thrust deduction fraction is found from the CFD simulations using the actuator disk model. The actuator disk model, which can be used to compute the propeller thrust in behind condition, is implemented in FINE™/Marine in the following way. The momentum equations include a body-force f_b (a source term). An actuator disk with inner radius R_H, outer radius R_P, and thickness Δ can be defined, which should be equal to the hub radius, radius, and thickness of the propeller respectively. The center of the actuator disk is set at the propeller center. A body force distribution is

then set on the actuator disk, with components f_{bx} (axial), $f_{br} = 0$ (radial), and $f_{b\theta}$ (tangential). The axial and tangential body force distributions vary in radial direction and are based on the Goldstein optimum circulation distribution, (Goldstein, 1929), without any loading at the propeller root and tip. Integration of the body forces over the actuator disk volume recovers the prescribed thrust T and torque Q. A more detailed description of the equations involved with the actuator disk model is given in appendix A. With the actuator disk model two different options are possible in FINE™/Marine:

- Specify thrust and torque and solve for the ship's speed
- Specify the ship speed and solve for thrust, by balancing the thrust with the ship's resistance.

In the second case, the propeller torque Q is not known. In that case, the actuator disk model should be coupled to the propeller open water curves. Alternatively, only a thrust distribution on the actuator disk is specified. Meaning that the body force is constant in the tangential direction.

The bodyforce distribution in the radial direction (thrust) is symmetric in the xz-plane. This allows to only model half the ship hull with a half actuator disk (for single-screw vessels). In that case, the plane y=0 should be a symmetry boundary condition. The full ship should be modeled if also a tangential bodyforce distribution (torque) is applied.

For the present work of this thesis, in all cases, the required thrust at a certain ship speed is computed. Only a thrust distribution is specified on the actuator disk. The reason for this is that propeller open water data is not available for all the different cases. Furthermore, the general cargo ship has a CPP propeller for which the pitch setting at a certain ship speed is not known beforehand. This means that the tangential velocities induced by the propeller are not modeled. However, Rotteveel (2019) states that axial propeller-induced velocities are considerably stronger than transversal velocities, so this should not affect the result significantly. Lastly, modeling only half the ship also reduces the computational cost significantly. Another assumption of the applied actuator disk model is that the thrust distribution is axisymmetric. In reality, a propeller operating behind a ship hull does not usually have a uniform thrust distribution. The velocity deficit in the wake closer to the ship hull is stronger. Because of this, the local angle of attack is also larger, which increases the local thrust force. Therefore a real propeller will not have a uniform thrust distribution in tangential direction. (Rotteveel, 2019). For the cruise ship, this effect is expected to be smaller, because it is a twin-screw vessel. In that case, the velocity deficit in the propeller plane is much lower. Villa et al. (2019) compared five different actuator disk models with different complexities, ranging from a constant thrust distribution to a radial and tangential varying thrust and torque distribution on the KCS hull form. The results were also compared to the RANS-BEM and the sliding mesh approach. A variation lower than 4% on the thrust deduction factor has been obtained among all the models. These results show that the thrust deduction effect can be modeled reasonably accurately with a simplified actuator disk model.

3.3.3 Wake fraction

The wake fraction is approximated from the nominal wake field. It should be noted that this assumption is not correct. The nominal wake fraction is typically higher than the effective wake fraction because it does not include the effects of the propeller, see also section 2.3.2. More sophisticated propeller models are required to obtain the effective wake field and the effective wake fraction such as the RANS-BEM method or resolving a fully discretized propeller using the sliding mesh technique. This would require a significant computational effort. Consequently, there will be a considerable modeling uncertainty present in the prediction of the wake fraction. The effect of this uncertainty on the accuracy of the power prediction is investigated in section 4.2. For twin-screw ships the nominal wake field is typically closer to the effective wake field than for single screw ships, (Carlton, 2007) and (Larsson & Raven, 2010). This is also visible in the comparison between model test and CFD results for the cruise ship, section 6.6.

3.4 Numerical setup

The flow around the ships, resistance, nominal wake field, and thrust are computed using CFD. The CFD software FINE™/Marine from Numeca is used. FINE™/Marine is a CFD system dedicated to marine applications. It is designed specifically for multiphase hydrodynamic problems, developed at the

Ecole Centrale du Nantes, and distributed commercially by Cadence. The software consisted of different components: HEXPRESS™can be used for automated generation of fully hexahedral unstructured grids; Marine solver: 6-DOF incompressible flow solver with free surface capturing; CFView™: qualitative and quantitative post-processing, (Numeca, 2024). The CFD software runs on a High-Performance Computing (HPC) cloud platform.

Resistance and self-propulsion simulations with the actuator disk model are commonly performed at Damen. For common ships (without air cavities) extensive verification and validation studies have been performed by the Damen RD&I department. Therefore, their recommended settings e.g. the grid size, time step, and convergence criteria will be used. The recommended settings by Damen are based on the guidelines of FINE™/Marine combined with the results of in-house R&D work. All simulations will be performed at full scale, given the pronounced scale effects present in the propeller wake field. The numerical setup of the CFD simulations will be explained in more detail in the subsequent sections.

3.4.1 Domain & boundary conditions

Figure 3.3 shows the used computational domain for all deep water simulations including the used coordinate system. The origin of the earth-fixed coordinate system is set on the mirror plane, at the stern of the ship at the waterline. In this way, the free surface (at t=0) is set at z=0. The size of the computational domain is 8L x 3L x 3L (Length x width x height). This ensures that the edges of the domain are located far enough away from the ship. For all cases, only half the ship is modeled to reduce the computational cost of the simulations. This can be done because the ship and the flow around the ship are symmetric.

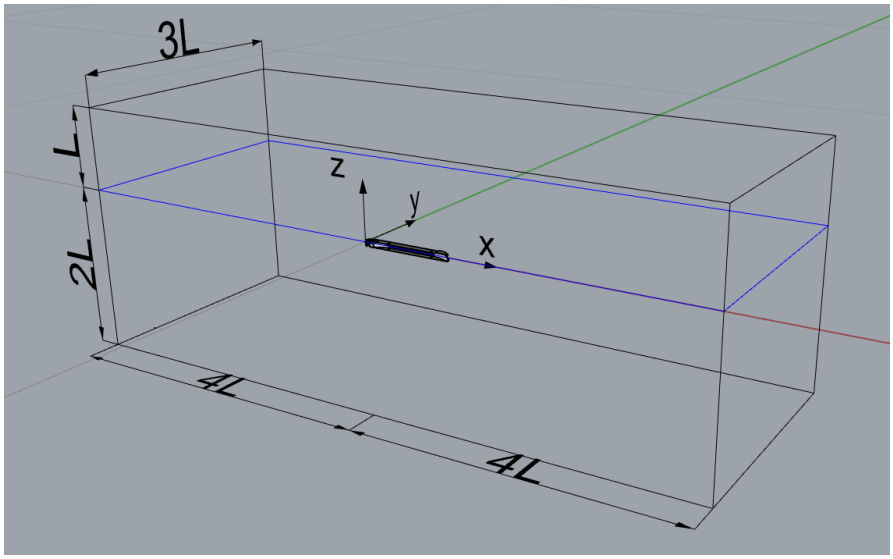

Figure 3.3: Computational domain for the CFD simulations.

Figure 3.4 shows the boundary conditions that are set. The motions of the ship (surge, heave, and pitch) are resolved. Therefore all vertical planes (inlet, outlet, and side) of the domain except the mirror plane have a far-field boundary condition with zero velocity, see also section 3.4.3. The deck of the ship has a slip-wall boundary condition because the air drag of the ship is not of interest to the present investigation. The rest of the ship geometry will have a wall-function boundary condition. All surfaces representing air cavities, if present, will have a slip boundary condition.

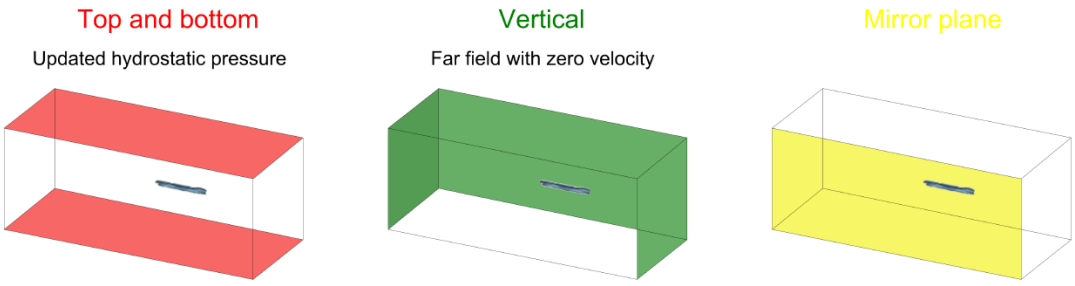

Figure 3.4: Boundary conditions for the CFD simulations in deep water, (Cadence, n.d.).

3.4.2 Solver settings

The 2-equation turbulence model k-omega (SST-Menter) is used to model the turbulence. This turbulence model is the industry-standard model for ship hydrodynamic applications, (ITTC, 2014). The flow in the boundary layer is modeled using wall functions because full-scale simulations are performed.

FINE™/Marine uses a finite volume method to discretize the flow. This method solves the momentum and mass conservation equations in integral form. The velocity field is obtained from momentum conservation and the pressure field follows from pressure-velocity coupling. AVLSMART is used as the discretization scheme for both the turbulence and the momentum equations. This discretization scheme is based on the 3rd-order QUICK scheme. The VoF (Volume of Fluid) model is used to model the interface between air and water. The BRICS scheme is applied for the discretization of the mass fraction equation. A more detailed description of the numerical framework of the FINE™/Marine solver and of the applied discretization schemes can be found in the FINE™/Marine theory guide, (Cadence, n.d.).

3.4.3 Body motion

During the simulations the surge motion of the ship is imposed, the heave (sinkage) and pitch (trim) motions are solved. When dealing with simulations to reach an equilibrium position for a hull (steady-state solution), the first method is to use a fully unsteady approach, i.e. to couple the flow motion and Newton's law at each time step. As a consequence, for the stability of the numerical algorithm, the required time step should be small enough. To relax this condition and decrease the CPU time, the quasi-static (QS) method has been developed. It is based on a succession of predicted body attitudes. These attitudes are evaluated using an ad-hoc quasi-static approach. This procedure remains stable even for larger time steps, enabling the use of the sub-cycling acceleration method for the fraction volume equation. (Cadence, n.d.)
For the surge motion, a 1/2 sinusoidal ramp profile is imposed with:

- Final time (t1): $V_{ref}/0.5$
- Final velocity (v1): V_{ref}

The heave and pitch motions are released from the start and are solved using the quasi-static method. The global time step of the simulations is computed based on the target Courant number of 0.3.

3.4.4 Convergence

Ensuring the convergence of a CFD simulation is critical to obtaining reliable and accurate results. In this research, convergence is assessed by monitoring the L2 norm of the residuals, which quantifies the average magnitude of the solution's change between iterations across all grid points. For each simulation, the residuals are expected to decrease significantly, indicating that the solution is approaching a steady state. For the CFD simulations of this research typically a reduction of 2-3 orders in magnitude is observed. Additionally, the convergence is verified through the stability of key physical quantities such as forces and motions (trim and sinkage). These quantities must stabilize and exhibit minimal variation over time. (ITTC, 2014). All integral quantities in this research (resistance components,

thrust, etc) are computed by taking the average of the last 10% of the solution in time. In all cases, the standard deviation of the last 10% of the solution was lower than 1%. No large differences in convergence behavior were observed between the different simulations and ships.

3.4.5 Mesh

HEXPRESS™is used for grid generation. This program is capable of generating unstructured hexahedral grids. First, a computational domain is created using Rhinoceros™. Afterwards, the domain is imported into HEXPRESS™. The mesh is generated in five steps:

1. Creating an initial mesh
2. Adapting to the geometry
3. Snapping to the geometry
4. Optimization of the mesh
5. Adding a viscous layer

In the initial step, the coarsest part of the grid is generated across the entire domain based on the required number of initial cells. Following this, the grid undergoes refinement to achieve the necessary level of detail. Refinements can be applied to surfaces, curves, or within specific boxes. Next, the grid is snapped to the geometry. After the mesh snapping phase, the grid typically exhibits poor quality. This is addressed during the optimization phase, where the grid quality is enhanced. The final step involves inserting the viscous layer into the grid. At this stage, cells near the geometry are expanded and filled with boundary layer cells, based on an initial cell size and growth ratio.

The amount of cells of the initial mesh, and the grid refinement levels on the hull and appendages are chosen based on the guidelines of the Damen RD&I department for performing ship resistance simulations. For the viscous layer, the first cell size is determined by the use of wall functions and based on the ship length and highest ship speed simulated. The target $y+$ value for all three ships was between 200 and 300. The exact value for each ship is slightly different due to the different Reynolds numbers for each ship. No viscous layer was inserted on the deck because the air resistance is not of interest. The minimum orthogonality for all meshes was 5 degrees (recommended by Numeca), to ensure suitable grid quality. Refinement boxes are added to accurately resolve the flow in important areas. The following refinement boxes are included:

- Bow wave region
- Stern wave region
- Transom region
- Propeller disk region (for actuator disk)
- Stern region (to accurately resolve the flow approaching the wake field)

The mesh settings are identical for all ships. Mesh refinement at the location of the propeller is required for the simulations including the actuator disk. However, it is also present for the simulations without the actuator disk. This reduces the amount of meshes that should be generated. One mesh can be used for simulations with and without the actuator disk. Figure 3.5 shows the mesh around the inland ship from different views. The mesh around the general cargo ship and the cruise ship shows a similar structure. The surface mesh on the appendages of the different ships is shown in figure 3.6. For the appendages, a finer mesh is present near the leading and trailing edge to accurately resolve the flow.

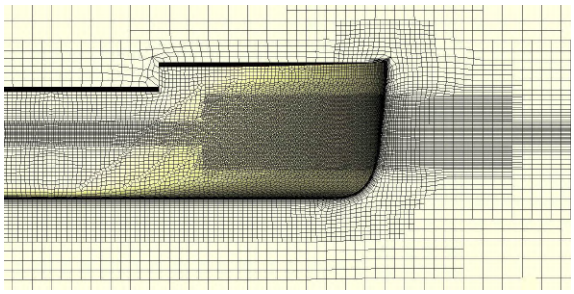

(a) Bow region

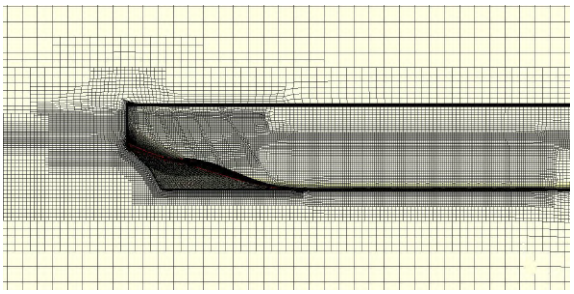

(b) Stern region

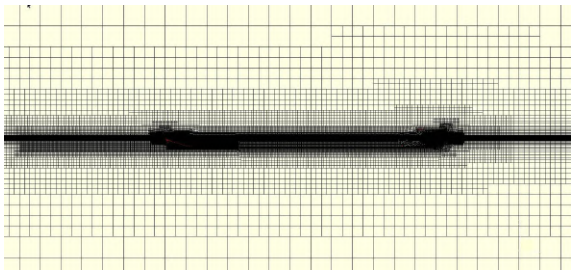

(c) Side view of the mesh around the ship.

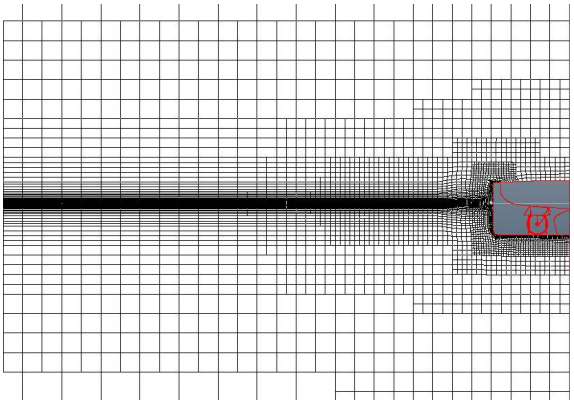

(d) Front view of the mesh around the ship.

Figure 3.5: Mesh around the inland ship from different views.

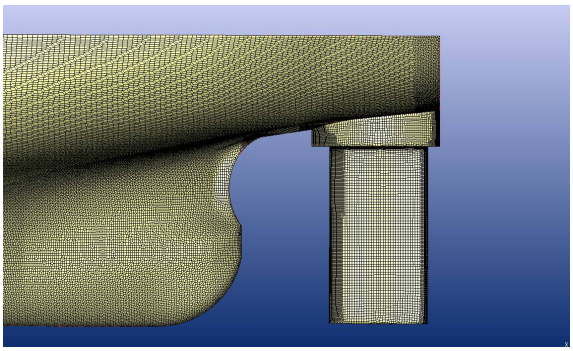

(a) General cargo ship: rudder & headbox

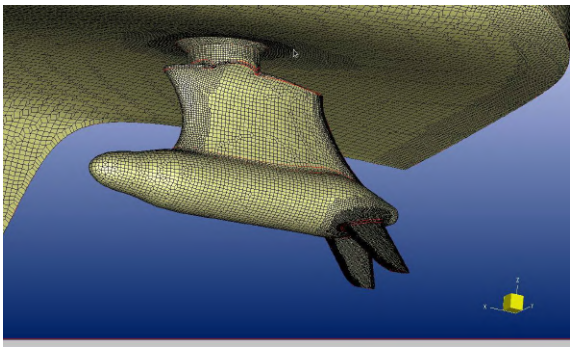

(b) Cruise ship: Pod

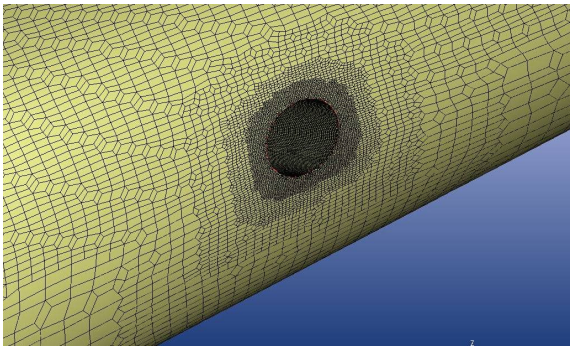

(c) Cruise ship: anti-suction tunnel

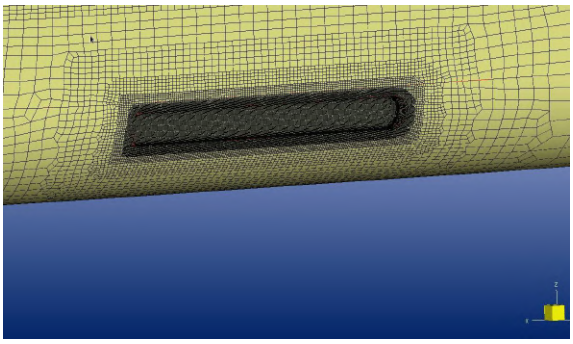

(d) Cruise ship: stabilizer fin recess

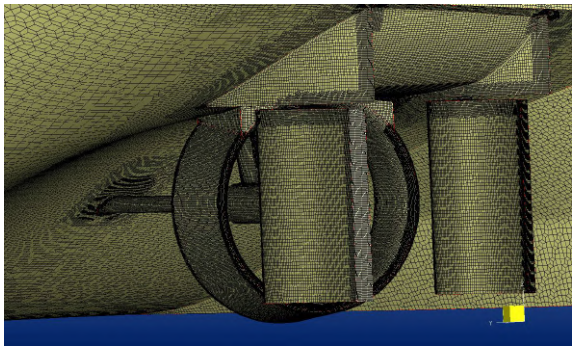

(e) Inland ship: shaft, nozzle and rudders

Figure 3.6: Surface mesh on the appendages of the different ships.

3.4.6 Mesh with air on

Some modifications are made to the mesh settings for the CFD simulations including the air cavities. A one-order higher grid refinement level, compared to the reference case is set on the entire flat bottom of the ship. This ensures a more detailed capturing of the flow of the bottom which is of interest. On the surfaces in between the air cavities, a more dense grid is required. This is because a new boundary layer is developed behind each cavity. Enough cells should be present in the longitudinal direction to accurately capture this effect, (Zverkhovskyi, 2023).

A small investigation was made into the required grid refinement level on the bottom surfaces in between the cavities for the general cargo ship. The amount of cells in length direction on the surface in between the cavities is varied. Three different variations in grid refinement level were made. Table 3.1 shows the change in resistance compared to the most refined case. The change in viscous drag is very small in between the three different cases. Surprisingly, the pressure resistance is also slightly changed, up to 1%. This could be because for the general cargo ship the air cavities also cause a reduction in pressure drag and flow separation on the stern, see section 5.6. However, the grid refinement study showed that a considerable uncertainty on the pressure resistance is present, see also section 4.1. Therefore the change could also be due to numerical uncertainty. A refinement level of 10 is selected to be applied to all simulations with air on as a compromise between computational cost

and accuracy.

Table 3.1: Change of the resistance compared to the finest case, for different refinement levels of the surfaces in between the cavities (N cells: amount of cells in length direction).

Refinement level	N cells	#cells	ΔR [%]	ΔR_p [%]	ΔR_v [%]
9	11	10.16E+06	-0.75	-1.06	-0.18
10	22	11.73E+06	-0.45	-0.60	-0.17
11	44	15.01E+06	-	-	-

The viscous layer is set on the entire bottom. For the air cavities, a viscous layer is not required because those surfaces have a slip boundary condition. However, excluding viscous layers on the bottom would result in big changes in cell sizes near the wall in front and behind the cavities. Potentially this could lead to numerical problems. Figure 3.7 shows the mesh on the bottom of the general cargo ship including. The figure shows that the surfaces in between the cavities have a higher refinement level than the cavities themselves. However, the change in mesh size is gradual and not abrupt. It could also have been possible to make a very fine mesh on the entire bottom to create an even smoother mesh. However, this would result in a large increase in the amount of cells of the mesh. Consequently, the computational cost would increase significantly.

Table 3.2 shows the number of cells in the mesh for all the ships with and without air. The cruise ship and inland ship have considerably more cells than the general cargo ship. This is because they have more appendages. For the general cargo ship, the amount of cells increases for a shorter cavity length. The reason for this is that for a shorter cavity length, the surfaces in between the cavities (which have a higher refinement level) are longer. The inland ship also has a large increase in cells comparing the reference case and air on. This is because its cavities are much shorter than for the other ships so more cavities and surfaces in between them are present.

Table 3.2: Amount of cells in the mesh for all ships with and without air cavities.

	# cells
General cargo ship ref	9.04E+06
General cargo ship $L_{cav} = 100\%$	11.7E+06
General cargo ship $L_{cav} = 87\%$	12.87E+06
General cargo ship $L_{cav} = 74\%$	14.67E+06
Cruise ship ref	12.57E+06
Cruise ship air on	16.03E+06
Inland ship ref	13.57E+06
Inland ship air on	18.97E+06

Figure 3.7 shows the mesh on the bottom of the three ships with cavities. The dense areas represent the surfaces in between the cavities.

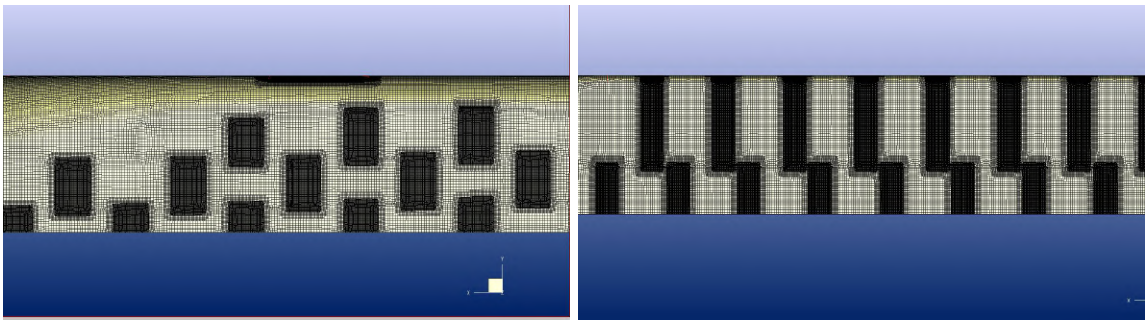

(a) Cruise ship *(b) Inland ship*

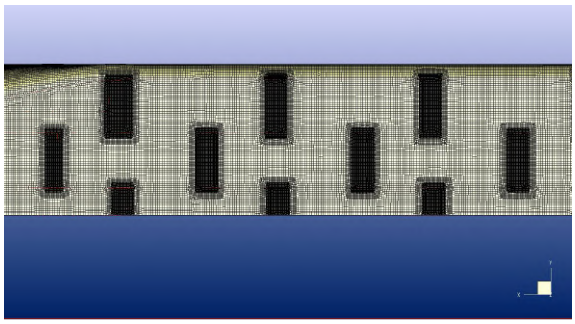

(c) General cargo ship

Figure 3.7: Surface mesh on the bottom of the three ships with air cavities.

3.4.7 Shallow water

For the CFD simulations in shallow water, several changes are made to the standard approach for deep water. These changes are based on recommendations from FineMarine™and best practices of Damen RD&I. First of all the computational domain is cut off. The bottom plane is moved up to $z = -H$. Furthermore, the bottom plane is split 0.5L behind the aft of the ship. This splits the bottom into two parts:

- Bottom_fwd: Bottom plane from inlet to 0.5L behind the aft of the ship
- Bottom_bck: Bottom plane from 0.5L behind the aft of the ship till the outlet

The Bottom_fwd plane will have a wall-function boundary condition, whereas the Bottom_bck plane will have a slip wall boundary condition. This modification is done to keep the cell count low by coarsening the cells at the back of the domain and removing the viscous layers. The flow over the bottom behind the ship is not of interest to the present investigation. Figure 3.8 shows all boundary conditions that are set for the CFD simulations in shallow water.

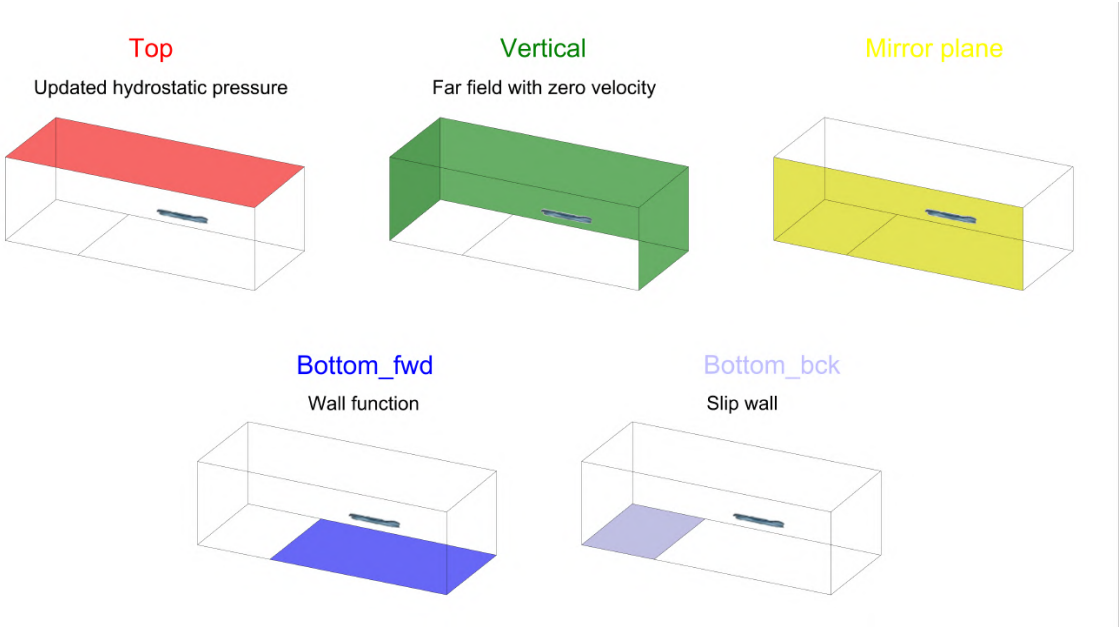

Figure 3.8: Boundary conditions for the CFD simulations in shallow water, (Cadence, n.d.).

Wave damping is activated. A wave damping zone is set 1L distance from each boundary to ensure that the reflections are dampened. Due to the squat effect in shallow water, the ship can have excessive sinkage and trim. Consequently, high mesh deformation between the ship's bottom and the sea floor can occur. This can lead to over-thinning of these cells, resulting in cells with negative volume. Therefore additional measures have been taken. First of all, the ship is meshed at the location of the expected sinkage. The sinkage is predicted using the method of Tuck (1966), see also section 7.5.2

Secondly, the body motion settings are changed. The sinkage is released from the start of the simulation. The trim, however, is released after the velocity ramp-up of the ship is completed. The under-relaxation parameters for both trim and sinkage are decreased to 0.05 (default is 0.2). Reducing under-relaxation parameters slows down the rate at which solution variables are updated during each iteration. This helps to prevent oscillations or divergence in the solution, promoting more gradual and stable convergence. Also, the position update intervals for trim and sinkage are set to every 20 timesteps. This is done to avoid abrupt changes in motion, which would make the ship touch the ground during the transient. The altered settings for body motion lead to a significant increase in computation time to achieve convergence of the body motions compared to deep water simulations.

The mesh settings are also changed. Viscous layers are set on the Bottom_fwd plane. The target $y+$ for the bottom equals 300. As already mentioned earlier no viscous layers are inserted on the Bottom_bck plane, to reduce the cell count of the mesh. Two additional mesh refinement boxes are added to the mesh in the region of the ship hull: one that covers the space between the hull and the sea floor as well as one that covers the free surface and the sea floor.

Chapter 4
Verification and Validation

Modeling the flow using CFD introduces errors and uncertainties in the computed result. It is important to know the uncertainty of the predicted results to draw reliable conclusions. For this two concepts are of importance: Verification and Validation. Verification refers to the question of whether the equations are solved in the right way, so it is a mathematical exercise. Validation refers to investigating whether the right equations are solved. Verification deals with numerical errors, whereas validation deals with modeling errors. CFD results can be validated by comparing them to experiments, e.g. model tests of sea trials. The numerical errors in the results can be investigated by performing a grid convergence study. First of all the setup and results of a grid convergence study for the general cargo ship are presented. Afterwards, a sensitivity study is performed to investigate the uncertainty of the power predictions. Lastly, validation between experimental and CFD results is performed.

4.1 Verification

An approximation of the numerical error arising from the CFD simulations is made by systematic grid refinement. Error is defined as the difference between the computed value and the extrapolated value from the numerical data fit. An estimate of the error is defined as uncertainty, which is made at some confidence level, usually 95%. This means that the extrapolated value from the numerical data fit of the quantity is expected to be within ±U interval about the computed value 95 times out of 100. (Insel, 2008) and (Coleman & Steele, 2018) According to Eça and Hoekstra (2014), it is commonly accepted that the numerical error of a CFD prediction has three components: the round-off error, the iterative error, and the discretization error. The round-off error is due to the finite precision of computers. The iterative error arises from the numerical approximation process, where repeated iterations to solve the governing equations may not converge exactly, leading to small discrepancies between the computed and converged solutions. The discretization error results from the approximations made to discretize the governing equations. The importance of the discretization error decreases with grid refinement.

For the computation of the numerical uncertainty, it is assumed that the contribution of the round of error and the iterative error to the numerical error is negligible compared to the discretization error. This assumption is commonly made because the round of error is typically very small. Furthermore, theoretically, it should be possible to reduce the iterative error to the level of the round-off error. (Eça & Hoekstra, 2014).

Eça and Hoekstra (2014) describe a method to compute the discretization error using systematic grid refinement. The basic equation to estimate the discretization error ϵ_ϕ is:

$$\epsilon_\phi \simeq \phi_i - \phi_0 = \alpha h_i^p \tag{4.1}$$

ϕ_i stands for any integral or other functional of a local flow quantity, ϕ_0 is the estimate of the exact solution, α is a constant to be determined, h_i is the typical cell size and p is the observed order of grid convergence. Equation 4.1 can only be applied when all grids are in the asymptotic range and the grids are geometrically similar. In practice, when simulating turbulent flows around complex geometries using unstructured grids it is hardly possible to meet these assumptions. Therefore Eça and Hoekstra (2014) proposed a slightly different procedure. With their method, a power function is fitted to the results in a least squares sense. The fitting of this function can be done for different power functions and also a weight factor can be added to the least squared method in this calculation. The uncertainty computation also accounts for scatter in the data and anomalous convergence behavior by using a safety factor. First, a judgment is made of the quality of the data fit, with the help of the data range parameter Δ_ϕ, see equation 4.2. The error estimation is considered reliable if the solution is monotonically convergent with $0.5 < p < 2.1$ and if the standard deviation of the data is lower than the data range parameter ($\sigma < \Delta_\phi$). In that case, a safety factor of 1.25 is applied to the uncertainty calculation. In all other cases a safety factor of 3 is applied. Due to the least-square approximation and possible spread in the data the results of at least four grids are required for the uncertainty calculation. The exact calculation process is described in more detail in Eça and Hoekstra (2014).

$$\Delta_\phi = \frac{(\phi_i)_{max} - (\phi_i)_{min}}{n_g - 1} \tag{4.2}$$

A grid convergence study is performed for the general cargo ship including the air cavities on the bottom. This appears to be the most interesting verification case because extensive verification studies on normal ships without air cavities were already performed earlier by the Damen RD&I department. The study is performed for the maximum speed measured at the sea trials of 12.97 knots. The parameters of interest are total resistance, pressure resistance, viscous resistance, and the nominal wake fraction, so the simulations were performed without an actuator disk.

For grid generation the mesh created using the guidelines was taken as the starting point (named fine), assuming that this mesh should have an acceptable and low uncertainty as it follows the best practice of FineMarine™and Damen. Two coarser grids (named coarse and medium) and one finer grid (named finest) were created with a grid refinement ratio of $\sqrt{2}$. This refinement ratio is recommended by ITTC (2017d) for industrial CFD grid refinement studies. Also, one other grid was added between the fine and the finest grid to have another data point with a dense mesh (named extra fine).

The grids were generated in the following way. The change in cell size between the meshes was achieved by changing the initial domain division cell size by the applied refinement ratio and keeping the rest of the settings (all mesh refinement levels) unchanged. An exception to this approach was the boundary layer mesh settings which sought to maintain the same surface y+ value for each mesh. Consequently, the cells in the boundary layer broadly maintained their wall-normal thickness in all cases (and were refined like the rest of the mesh in the wall-tangent directions). Y+ is kept constant because theoretically, any y+ value in the log-law region of the boundary layer should give the same result when using wall functions. As a result, all grids are approximately geometrically similar except for the boundary layer region. Keeping the y+ value constant for all verification cases aligns with the approach recommended by Roache (1997), whereby he considers the wall function akin to an elaborate boundary condition and so commences the grid study outside it. This approach differs from the case when a wall-resolved turbulence model is used. In that case, the y+ value should also be changed in between the different grids and effort should be made to create a geometrically similar viscous layer, see e.g. Vink (2017).

Typically, the grid refinement ratio h_i/h_1 used for the numerical uncertainty computation is computed based on the number of cells present in the mesh:

$$h_i/h_1 = \left(\frac{N_1}{N_i}\right)^{1/3} \tag{4.3}$$

with N_1 the number of cells in the finest mesh, and N_i the number of cells in the i-th mesh. However, this is not correct when grid similarity is only present outside the viscous layer, because the viscous layer is not geometrically similar between the different grids. Therefore the grid refinement ratio is computed based on the amount of cells present after the initial domain division step in the mesh. The CFD results for the different grids are presented in table 4.1 and figure 4.1. The figure shows that the results of the pressure resistance show a deviation from the main trend that is observed at $h_i/h_1 = 1.162$. The reason for this is not understood as no significant difference in the convergence of the force signal (standard deviation) and in the convergence of the residuals of this simulation was observed.

Table 4.1: CFD results on the different grids.

	h_i/h_1	R [kN]	R_p [kN]	R_v [kN]	$(1-w)$ [-]
Coarse	2.771	197.04	129.57	67.47	0.667
Medium	2.000	194.87	127.34	67.52	0.672
Fine	1.402	189.41	121.77	67.64	0.677
Extra Fine	1.162	189.73	122.20	67.53	0.676
Finest	1.000	188.68	121.17	67.51	0.675

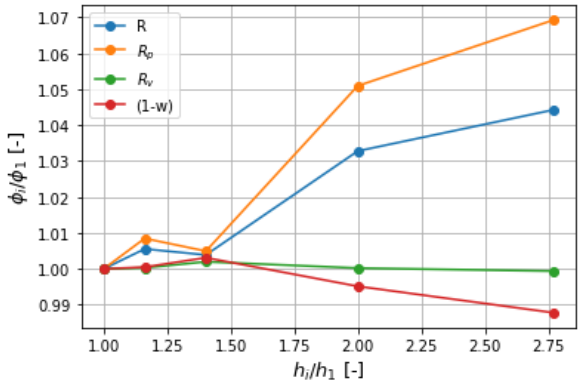

Figure 4.1: Relative difference of resistance and wake factor for different cell sizes.

Table 4.2 shows the computed numerical uncertainty. The results are also plotted in figure 4.2. The change in the viscous drag between the different grids is really small. Also, no clear convergence behavior is visible (p is outside of the range $0.5 < p < 2.1$). Consequently, a safety factor of 3 is applied to the computed uncertainty as recommended by Eça and Hoekstra (2014). Probably this is because y+ is not changed between the different grids. The viscous resistance is obtained by integrating the wall shear stress over the surface of the hull. The wall surface is computed from the wall-normal derivative of the flow velocity and it is therefore less sensitive to the grid size in the wall tangent direction. This is also in agreement with the results from the variation of the amount of cells in the wall-tangent direction in between the cavities, see section 7.5.2. Also, in that case, little change in the resistance was observed. Still, a low uncertainty of 2.8% is obtained on the fine mesh, despite the safety factor of 3.

The nominal wake factor shows a smooth second-order convergence behavior and has therefore a low numerical uncertainty. For the pressure resistance and consequently also for the total resistance, a low order of grid convergence (close to 1) is observed. Hence a relatively high numerical uncertainty for the pressure resistance of 9.5% is obtained on the fine mesh. This low order of grid convergence was not expected. A possible reason could be that significant flow separation is present on the gondola of the ship, see also section 5.2. It is questionable if this flow phenomenon is accurately resolved using wall functions. All in all, a numerical uncertainty of 6.5% is obtained for the fine mesh.

The settings for the fine mesh are used for all other CFD simulations in this thesis. This is because of the low order of grid convergence for the pressure and total resistance. Using a finer mesh would increase the computational cost significantly and no significant gain in accuracy would be achieved. Furthermore, the viscous resistance and nominal wake factor which are of main interest for this research have a low numerical uncertainty on the fine mesh.

Table 4.2: Discretization uncertainty of the parameters on the different grids.

	h_i/h_1	u_R [%]	u_{Rp} [%]	u_{Rv} [%]	$u_{(1-w)}$ [%]
Coarse	2.771	10.21	15.00	2.16	3.24
Medium	2.000	8.26	12.01	3.25	1.93
Fine	1.402	6.51	9.49	3.27	1.66
Extra Fine	1.162	5.21	7.43	2.78	0.99
Finest	1.000	4.57	6.48	2.55	1.08

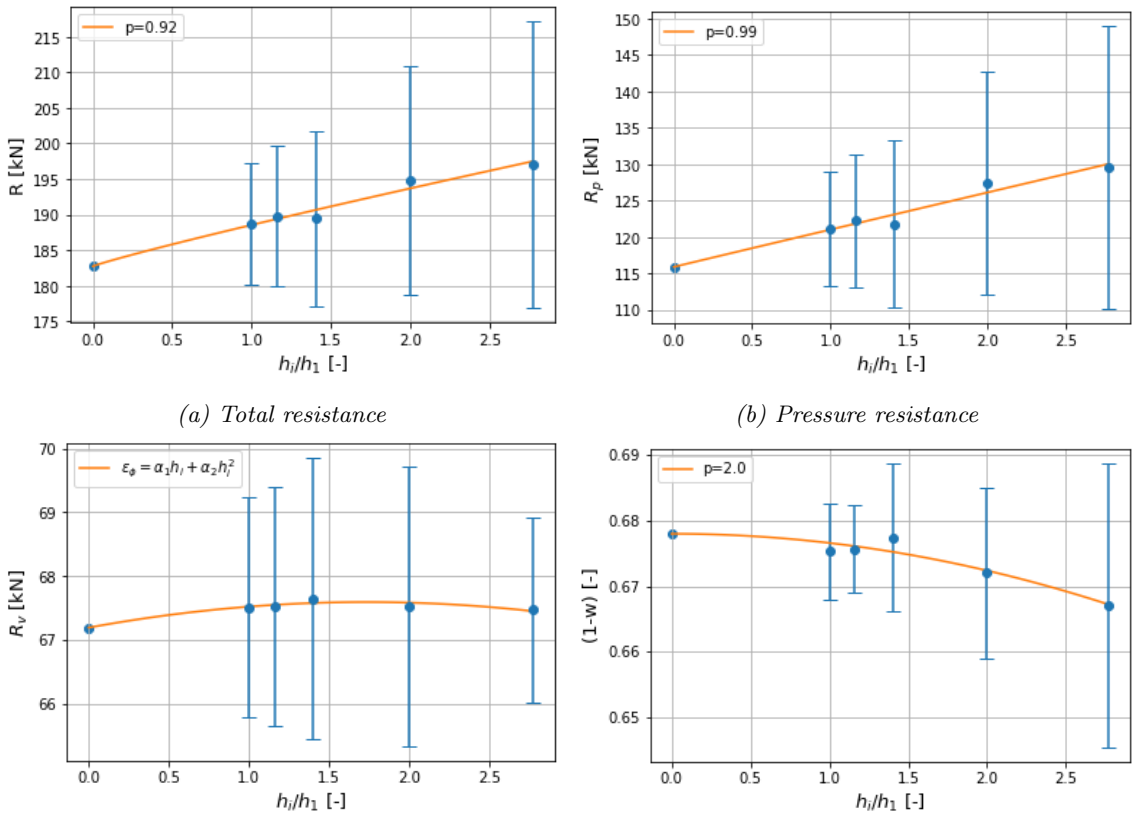

(a) Total resistance

(b) Pressure resistance

(c) Viscous resistance

(d) Nominal wake factor

Figure 4.2: Results of the grid refinement study.

4.2 Sensitivity study

For the validation of the method against sea trial measurements (general cargo ship) and model test measurements (cruise ship) quantities are compared that are computed based on multiple parameters. E.g. for the general cargo ship the shaft power is compared which is a function of resistance, thrust deduction, wake factor, propeller efficiency, etc. Each parameter is determined differently and has therefore a different uncertainty. Vrijdag (2014) studies the uncertainty in ship performance predictions, namely ship speed, brake power, and bollard pull predictions in the design stage. These predictions are comparable to the predictions that are made in this thesis. Vrijdag (2014) suggests two different methods to quantify output uncertainty based on uncertain input parameters: a linearization approach and a Monte Carlo approach. When using the Monte Carlo approach, outputs are repeatedly calculated by randomly selecting input parameters from their distributions, resulting in various system realizations and corresponding outputs.

Both methods have their strong and weak points. The linearization approach gives insight into the underlying system because it quantifies the contributions of all parameters. However, it is a linear method so it only gives accurate predictions for linear models. In contrast, the Monte Carlo approach can handle non-linearities, but it does not give direct insight into the underlying system behavior.

According to Vrijdag and de Vos (2012), a ship propulsion system behaves closely to linear for reasonably sized variations in input parameters. Furthermore, it is very useful to investigate which parameters contribute the most to the output uncertainty of the problem. In this way, a better interpretation of the output uncertainty can be obtained. Therefore the linearization method is applied.

4.2.1 Linearization method

With the linearization method, the output uncertainties can be computed from the output sensitivities and the input uncertainties. For an output quantity z that is a function of input quantity x:

$$z = f(x) \tag{4.4}$$

The output sensitivity is then expressed as:

$$\frac{\partial z}{\partial x} \tag{4.5}$$

It can be convenient to use the normalized sensitivity:

$$\frac{\partial z^*}{\partial x} = \frac{\partial z}{\partial x} \cdot \frac{x_0}{z_0} \tag{4.6}$$

with x_0 and z_0 the nominal values of input and output. This normalized presentation allows for a more intuitive interpretation since it expresses the percentage of change in output based on a percentage change in input. All input parameters have their own input uncertainty. Multiple types of uncertainty exist, e.g. modeling uncertainty, measurement uncertainty, numerical uncertainty, etc. For the present analysis, modeling and numerical uncertainty are deemed to be the most important. Modeling uncertainty means using simplified versions of real-world physics in models, recognizing that these simplifications may not fully capture the complexities of the actual system. An example is the thrust deduction factor which is determined using the actuator disk model, which is a simplified representation of reality. Another example is the relative rotative efficiency η_r which is approximated to be equal to 1. It is difficult to quantify the modeling uncertainty, Vrijdag (2014) suggests to use expert opinion.

In the analysis also numerical uncertainty is present because several parameters are obtained using CFD, e.g. resistance. For this analysis the numerical uncertainty is assumed to be equal to the grid discretization uncertainty, see section 4.1. The total input uncertainty u can then be computed from the modeling uncertainty u_m and the numerical uncertainty u_n:

$$u = \sqrt{u_m^2 + u_n^2} \tag{4.7}$$

The output uncertainty can be computed from the input uncertainties u_i and the output sensitivities $\partial z\ \partial x_i$:

$$u_z^2 = \sum_i (\frac{\partial z}{\partial x_i})^2 \cdot u_{x_i}^2 \tag{4.8}$$

When normalized input uncertainties and sensitivities are used the equation changes to:

$$(u_z^*)^2 = \sum_i (\frac{\partial z^*}{\partial x_i})^2 \cdot (u_{x_i}^*)^2 \tag{4.9}$$

The above-described method is performed for both the general cargo ship and the cruise ship in the following way. A Python script was made that computes the shaft power P_s based on the different input parameters. The sensitivities are computed numerically using the central difference scheme. For both ships, the analysis is made at the typical operational speed.

4.2.2 General cargo ship

For the general cargo ship, the input parameters are:

- Resistance R
- Thrust T
- Nominal wake factor $(1 - w_n)$
- Relative rotative efficiency η_r
- Blade area ratio A_e/A_0

The open water efficiency of the propeller is computed from the known propeller diameter and the approximated blade area ratio. For more details on the exact calculation procedure see section 5.2. Therefore the blade area ratio of the propeller is one of the input parameters for this analysis.

R, T and $(1-w)$ are determined numerically so their numerical uncertainty equals the grid discretization uncertainty as determined in section 4.1. The actuator disk model was not included in the grid convergence study. However, the trust is the ship's resistance including the added resistance due to the suction of the propeller. Therefore is seems to be an appropriate assumption that the numerical uncertainty of the thrust is assumed to be equal to that of the resistance.

For resistance, a modeling uncertainty of 0.02 is applied which accounts for the approximated shape of the rudder and for the approximations made for wind and roughness resistance. The modeling uncertainty for eta_r was retrieved from Vrijdag (2014). For the wake factor and for thrust the modeling uncertainty was approximated to be 0.05. This is because the thrust is computed using the actuator disk model and the wake factor is computed from the nominal wake field and not from the effective wake field. Both are simplifications of reality. Lastly, a high uncertainty of 0.1 is assumed for the blade area ratio. The reason for this is that the propeller shape is unknown and therefore subject to a high uncertainty. A blade area ratio of 0.7 was assumed, which is usually a starting point for design, however, the actual value could very well be much different.

Table 4.3 shows the input uncertainties and the contribution to the output uncertainty for the general cargo ship. The sensitivities to shaft power are shown in figure 4.3. The figure shows that for resistance the sensitivity is zero. The reason for this is that resistance cancels out in the equations when computing the shaft power. The figure also shows that the blade area ratio has a normalized sensitivity of 0.53, meaning that although this parameter has a high uncertainty, its contribution to the output uncertainty is lower. All together the total output uncertainty of shaft power is then computed to be **10.2 %**. The largest contribution to the output uncertainty is due to the thrust prediction, followed by the blade area approximation. In this case, the most effective way to reduce this uncertainty is to decrease the uncertainty of the thrust prediction. It can be done by using a finer mesh in the CFD simulations (to decrease the numerical uncertainty). The modeling uncertainty of the thrust can be reduced by, e.g. using a more complex actuator disk model or by also modeling the propeller using a sliding mesh technique.

Table 4.3: Cargo ship: numerical, modeling, and total input uncertainties and the contribution to the output uncertainty of the input parameters.

	u_n [-]	u_m [-]	u [-]	$(u^*_{z,i}{}^2)$ [-]
R	0.065	0.02	0.068	-
T	0.065	0.05	0.082	6.81E-03
$(1-w_n)$	0.017	0.05	0.053	3.43E-04
η_r	-	0.02	0.02	4.00E-04
A_e/A_0	-	0.1	0.02	2.85E-03

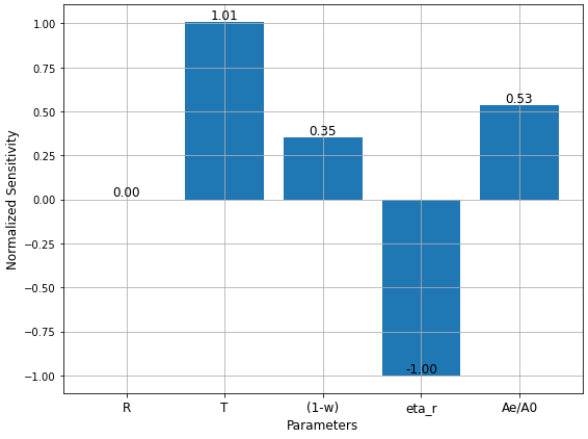

Figure 4.3: Normalized sensitivity to shaft power for the general cargo ship.

4.2.3 Cruise ship

An approximation of the shaft power uncertainty was also made for the cruise ship. For this ship, the calculation procedure is slightly different. The ship has a fixed pitch propeller, so the open water efficiency is computed from the intersection of the $K_{T,ship}$ curve and the propeller K_T curve in the open water diagram, see also section 3.3 The propeller specification is available so there is no uncertainty in the blade area ratio, in contrast to the general cargo ship. However, the open water diagram of the propeller was not available so it was assumed to be equal to that of a B-series propeller with the same properties as the actual propeller. This introduces a modeling uncertainty because the actual propeller performance might be different to that of the B-series propeller. Furthermore, the open water diagrams of the B-series also have an experimental uncertainty. To account for this, Vrijdag (2014) suggests using a modeling uncertainty of 0.025 for the K_T and the K_Q curve.

For the cruise ship, no grid convergence study was performed. The mesh settings for the cruise ship are very similar to those of the general cargo ship (in terms of domain size and grid refinement levels). The Froude number and Reynolds number are also relatively close for both ships. However, the general cargo has quite some flow separation at the transom and at the gondola. This is not the case for the cruise ship. It only has a little bit of flow separation at the appendages. This flow separation could be a reason for the relatively high uncertainty of resistance and thrust for the general cargo ship. Therefore the numerical uncertainty of the cruise ship could be lower. Now a conservative approximation is made.

For the cruise ship, a lower modeling uncertainty of 0.02 is assumed for the wake factor. This is because the cruise ship is a twin screw ship and it has a rather low wake fraction. Usually, the effective wake field is close to the nominal wake field for twin screw ships, (Carlton, 2007). The other uncertainties are the same as for the general cargo ship.

Table 4.4 shows the input uncertainties of the cruise ship. The sensitivities to shaft power are shown in figure 4.4. All together the total output uncertainty of shaft power is then computed to be **10.3 %**. Surprisingly this uncertainty is close to that of the general cargo ship, although that ship has a much larger uncertainty for the propeller. The reason for this is the difference in sensitivity for the propeller data and wake fraction for both ships. The prediction of the thrust is by far the biggest contribution to the uncertainty of the power prediction for the cruise ship. Also for this ship, the most effective way to decrease the uncertainty is therefore to lower the numerical and modeling uncertainty of the thrust.

Table 4.4: Cruise ship: numerical, modeling, and total input uncertainties and the contribution to the output uncertainty of the input parameters.

	u_n [-]	u_m [-]	u [-]	$(u^*_{z,i})^2$ [-]
R	0.065	0.02	0.068	-
T	0.065	0.05	0.082	8.31E-03
$(1-w_n)$	0.017	0.02	0.026	4.08E-04
η_r	-	0.02	0.020	4.00E-04
K_T curve	-	0.025	0.025	7.70E-04
K_Q curve	-	0.025	0.025	6.25E-04

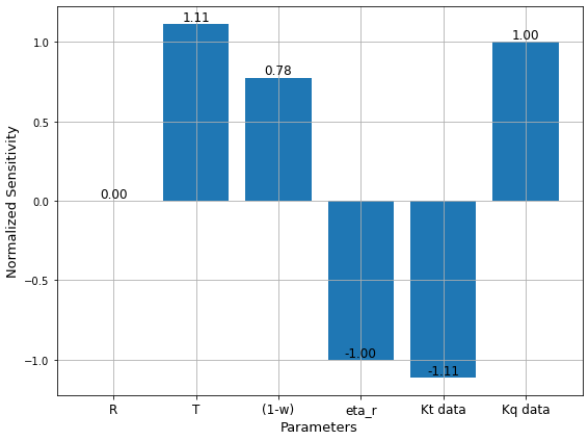

Figure 4.4: Normalized sensitivity to shaft power for the cruise ship.

4.3 Validation

Validation is performed by comparing the computed results to experimental data. A quantity can be considered validated if the comparison error E is lower than the validation uncertainty U_{val}:

$$|E| < U_{val} \tag{4.10}$$

The validation uncertainty is a combination of the uncertainty of the computed result U_c and the experimental uncertainty U_e:

$$U_{val} = \sqrt{U_c^2 + U_e^2} \tag{4.11}$$

This section explains how the experimental uncertainty is approximated for the validation of the results of the general cargo ship and the cruise ship. A comparison between the experimental and computational results is presented in chapters 5 and 6. Often a correction factor is added to CFD results when comparing power predictions made using CFD with sea trial measurements or model test results. This correction factor is based on the accuracy of earlier predictions. For this research, such a correction is not applied because it is unclear if the correction factor would be similar when the cavities are added to the ship.

4.3.1 Sea trial uncertainty

For the general cargo ship, a comparison is made between the computed power and the power measured during sea trials. Several authors studied the uncertainty encountered when performing sea trial measurements. The experimental uncertainty U_e is commonly split into the bias error B and the precision error P:

$$U_e = \sqrt{P^2 + B^2} \tag{4.12}$$

Precision errors are due to random scatter of the data. Bias error, also known as systematic error refers to the deviation of measurements from the true value due to flaws in the experimental setup, calibration, or measurement technique. (Insel, 2008) and (Coleman & Steele, 2018). Insel (2008) attempted to quantity the uncertainty encountered during sea trial measurements using a Monte Carlo analysis. He stated that ship trials have uncertainties mainly due to two sources:

- Trial measurements: torque, shaft revolution rate and ship speed measurement uncertainties;
- Trial analysis: uncertainties due to corrections applied to trial measurements

He found an average bias error of 3-5% and an average precision error of 7-9% on shaft power. Furthermore, he found that the precision error is governed mainly by the sea trial conditions such as waves, wind, and current. A similar study was performed by Seo and Oh (2021). They found a relatively low uncertainty on shaft power of 1-2% in ideal conditions. The biggest uncertainty source was the

shaft power measurement system. They also stated that the uncertainty will increase when corrections are made due to the weather conditions. A validation study of full-scale CFD-delivered power predictions was performed by Orych et al. (2021). They estimated the experimental uncertainty of the sea trial measurements from the results of (Insel, 2008) to be 6%. It should be noted, however, that they assumed a low precision error because sea trial data was available for 12 sister ships. Other full-scale CFD validation studies used experimental uncertainties of 7.6% (K. Korkmaz et al., 2023) and 10% (Werner & Gustafsson, 2020). Recently another study on sea trial uncertainty was published, (Ponkratov & Struijk, 2024). An uncertainty of 4-6% was reported for power speed trials in favorable weather conditions. Summarizing all literature contributions, the experimental uncertainty of sea trials will be between 5 and 10% and it increases when corrections are made due to the weather conditions. The sea trials of the Danita were performed in calm weather conditions. Furthermore, the results were averaged from four runs were performed, which decreases the precision error. Therefore, in this case, the sea trial uncertainty is estimated to be approximately **5%**.

4.3.2 Model test uncertainty

The results for the cruise ship are compared to model test data. An extensive investigation into model test uncertainty was performed by Forgach (2002). He found an uncertainty of 1.79% for model scale resistance and 0.66% for model scale delivered power. ITTC (2017b) and ITTC (2017e) also report uncertainties in the order of 1-3% for model scale resistance and self-propulsion parameters. However ITTC (2017e) states that extrapolation to full scale might lead to significant sources of error and uncertainty. Therefore a conservative **5%** uncertainty is approximated for the full-scale experimental uncertainty of all extrapolated model test results.

4.3.3 Uncertainty air cavity modeling

Additional uncertainty is present for results including the air cavities. This is due to the cavity length approximation, possible change in hull roughness after installation of the system, and the modeling of the added resistance of the appendages. In chapters 5, 6, and 7 a comparison is made between experimental and computational results for the change in resistance, wake factor, propeller efficiency, and power caused by the air cavities. The uncertainty is different for the results of the cargo ship and the cruise ship because different assumptions were made. Therefore it is separately discussed in a qualitative way for each ship, see sections 5.7 and 6.6. An investigation into the possible cause of differences is made when large discrepancies are visible between the CFD and experimental results. E.g. for the general cargo ship, the effect of a possible shorter cavity length is investigated, see section 5.8

Chapter 5
General cargo ship

5.1 Description

The first case study is performed on the Danita, a general cargo ship on which the Damen Air Cavity System (DACS) is installed. The ship is equipped with a single diesel engine and has a CPP propeller. The vessel sails at a fixed engine rpm due to the shaft generator. Table 5.1 shows the properties of the general cargo ship at the trial loading condition. The typical operational speed of the ship is between 12 and 13 knots. Figure 5.1 shows a picture of the vessel.

Table 5.1: Cargo ship: general properties.

Length L_{wl} [m]	114.11
Beam B [m]	16.5
Draft aft T_{aft} [m]	5.0
Draft fore T_{fore} [m]	4.65
Displacement Δ [ton]	7667.8
Block coefficient C_b [-]	0.823

Figure 5.1: General cargo ship Danita, (Damen Shipyards Group, 2023).

The ship has a relatively full hull form and therefore a high block coefficient. For this analysis a 3D model of the ship hull was available. Figure 5.2 shows the bow and the stern shape of the ship. The rudder however was not present in the available 3D model. Therefore the rudder and headbox of a comparable vessel with a similar rudder type (Damen CF3850) were added to the 3D model. The rudder and headbox shapes were very similar. Only the size was slightly different. Therefore, they have been scaled to the correct size as indicated on the GA drawing of the vessel. Because the rudders of the two vessels are comparable it is assumed that the use of this different rudder will not affect the results of the simulations.

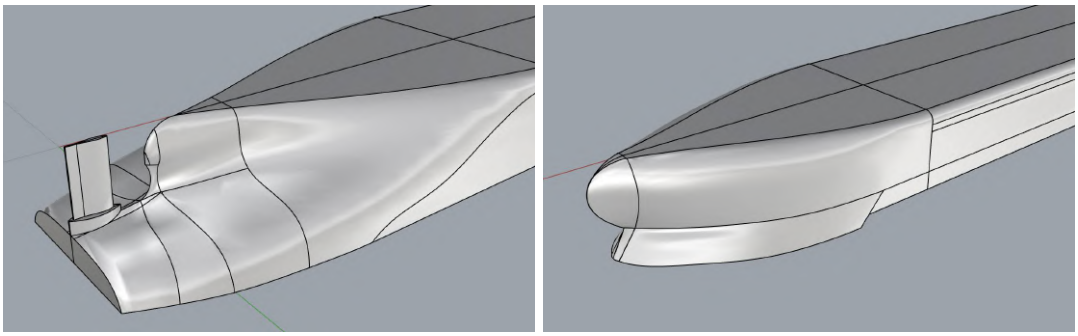

Figure 5.2: Cargo ship: bottom view of the bow and stern shape.

The ship is equipped with a controllable pitch propeller (CPP) with a diameter of 3.6m. Unfortunately, little details about the propeller geometry are known except of the number of blades (4). The hub diameter and the propeller thickness could be approximated for the GA drawing of the ship.

5.2 Reference case

First of all, CFD simulations were performed for the reference case (before the installation of the DACS system). The (mesh) settings of the CFD simulations were already described in section 3.4. The CFD simulations were performed at the same speeds as measured during the sea trials. Table 5.2 shows the results of the CFD simulations. The table shows that the viscous drag is more dominant at lower speeds. Furthermore, the ship has a high nominal wake fraction.

Table 5.2: Cargo ship reference case: CFD results.

v_s [kn]	Fr [-]	R [kN]	R_p [kN]	R_v [kN]	R_v/R [-]	(1-w_n) [-]	$(1-t)$ [-]
9.07	0.14	79.43	28.57	50.86	0.64	0.610	0.810
10.67	0.16	112.09	42.89	69.25	0.62	0.614	0.809
11.95	0.18	152.05	66.59	85.51	0.56	0.617	0.809
12.41	0.19	181.30	91.86	89.44	0.49	0.614	0.812
12.97	0.20	228.49	128.53	99.96	0.44	0.607	0.815

Based on the CFD results a power speed prediction is made. The computation differs from the methodology described in section 3.3 for the computation of the propeller efficiency. As explained earlier only the diameter and number of blades of the propeller are known. An approximation of the propeller efficiency is made in the following way: The blade area ratio A_e/A_0 is assumed to be 0.7. This is a typical value for propellers of comparable ships built at Damen. The rpm of the propeller is fixed and known, meaning that the advance ratio can be computed for each speed. Then for each speed, the propeller pitch is solved with the help of the Wageningen C-series, a systematic series of CPP propellers. From the computed thrust the non-dimensional required thrust coefficient $K_{T,req}$ can be computed. Then the propeller pitch is solved which has the same K_T value as the required K_T value at the given advance ratio. Afterwards, all required parameters (diameter, blade area ratio, advance ratio, number of blades, and pitch) are known to compute the open water efficiency η_o from the Wageningen C-series. The computation is performed with a tool created by the Damen RD&I department that contains all polynomials of the Wageningen C-series.

The results of the power speed computation are presented in table 5.3. The table shows that the ship has a low pitch and also low propeller efficiency at the operational speed of 13 knots. Probably the propeller was designed for a different loading condition and some sea margin could also have been present. Another possibility is that the propeller was designed for a higher speed.

Table 5.3: Cargo ship reference case: power speed computation.

v_s [kn]	R_{cor} [kN]	P_s [kW]	η_o [-]	P/D [-]	η_h [-]	η_d [-]
9.07	82.84	1093.7	0.266	0.379	1.327	0.353
10.67	118.07	1355.5	0.363	0.465	1.317	0.478
11.95	160.62	1780.6	0.423	0.557	1.312	0.555
12.41	190.91	2077.7	0.443	0.608	1.323	0.587
12.97	239.47	2598.0	0.459	0.679	1.341	0.615

5.3 Comparison with sea trials

Power speed measurements have been performed during sea trials. Three different cases were measured:

- Before the installation of DACS (reference)
- After the installation with air OFF
- After the installation with air ON

All trials have been performed according to the standards of ISO15016 (Guidelines for the assessment of speed and power performance by analysis of speed trial data), ("ISO 15016: Guidelines for the assessment of speed and power performance by analysis of speed trial data", 2015). Calm weather was observed for all tests (1-1.5 m wave height and 10-15 knots of wind). All tests have been performed at the same draft, with sufficient water depth, and comparable weather conditions (within the definitions and limits of ISO15016). The ship was fully loaded during all sea trials. During the trials, the ship speed, and shaft power were measured (torque measurement on the propeller shaft). The compressor power for the air supply was also measured for the case with air ON. For each speed that was tested, four runs were performed. The final results were averaged over those for four runs. The power consumption for all three trials is calculated back to ideal weather conditions according to ISO 15016 for comparison. All runs were done at the same engine rpm. The vessel's speed was modified by changing the propeller pitch. Measurements were performed at the top speed of the ship (fully loaded) and at multiple lower speeds.

The ship went into drydock to install the DACS system. During the installation, the hull was also cleaned. Because of this, the hull roughness before and after installation could be different. However, this ship mainly sails in the Baltic Sea. The Baltic Sea is known for its low fouling pressure (among others due to local climate and the low biodiversity), (European Commission Directorate-General for Environment, 2023). Furthermore, little fouling was observed during the drydock inspection. Therefore the change in hull roughness will probably be low, but it could still be present. The actual power reduction caused by the air cavity system might therefore be slightly lower than when comparing the reference case with the air on case. However, the ship has the same hull roughness when comparing the cases air off and air on. For that comparison, the power reduction is larger, which shows that the system is functioning.

A comparison is made for the shaft power of the ship in the reference condition between the sea trial measurements in ideal trial condition and the CFD results. The results are shown in table 5.4 and in figure 5.3. They show that the difference at 9 knots is really low. However, the difference increases with increasing speed, with CFD underpredicting the sea trial measurements.

In chapter 4 an approximation of the experimental uncertainty of the sea trials U_e (5%)and of the uncertainty of the predicted power using CFD U_c (10.2%). This leads to a total validation uncertainty U_{va} of 11.4%. Table 5.4 shows that the comparison error is lower than the validation uncertainty for a speed of 9.07 and 10.67 knots. This means that no validation is present at the other speeds. In the sensitivity analysis, it was shown that the biggest contributions to the uncertainty are the thrust prediction and the approximation of the propeller geometry. They are therefore probably the most important reason for the difference between CFD and sea trial results, see also section 4.2.2. Another reason could be that the sea trials were performed before the ship went into dry dock. The hull roughness could be larger than assumed for the corrections of the CFD results. An underprediction of the required power when using CFD is a common observation in literature, see e.g. Mikulec and Piehl (2023). It is unclear why the difference changes with increasing speed. Probably it is a combination of the underlying uncertainties of all the assumptions made for both methods.

Table 5.4: Cargo ship reference case: comparison of shaft power predicted using CFD and measured during sea trials (ideal condition).

	P_s [kW]		
v_s [kn]	Sea trial	CFD	Diff. [%]
9.07	1095.1	1093.7	-0.13
10.67	1456.0	1355.5	-6.90
11.95	2011.8	1780.6	-11.49
12.41	2398.8	2077.7	-13.39
12.97	3009.9	2598.0	-13.69

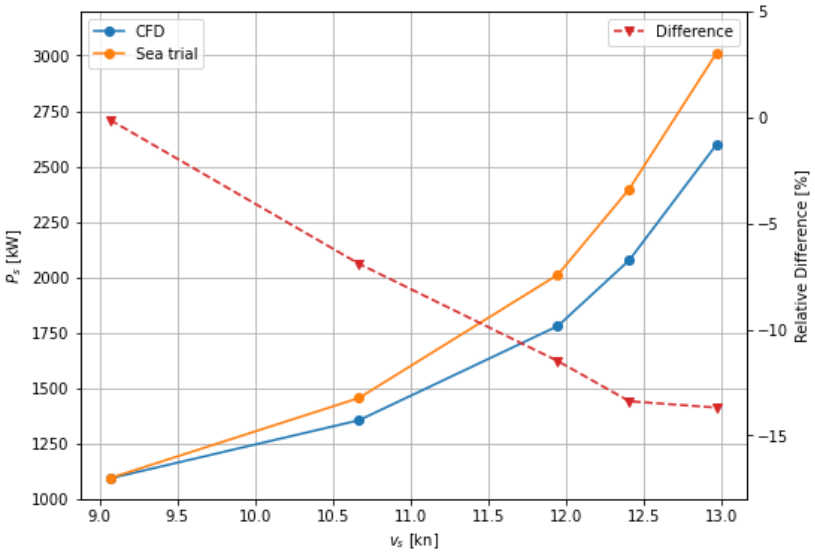

Figure 5.3: Cargo ship reference case: shaft power predicted using CFD and measured during sea trials (ideal condition).

5.4 Air cavity system

Figure 5.4 shows a schematic layout of the air cavity system on the bottom of the ship. The size of the cavitators is exaggerated for visualization purposes. The modeling methodology of the air cavities is already explained in section 3.1. For this ship, the cavity length is limited by the skeg height at the operational speed of the ship. The cavity length is therefore computed from the skeg height and equals approximately 90% of the distance in between the cavitators. After the CFD simulations were performed it was realized that the cavity length at 9.07 knots is limited by the flow velocity rather than the skeg height and is therefore slightly shorter. Therefore the results at 9.07 knots with air on do not represent a physical air cavity. Still, the results at 9.07 knots are presented to give an indication of what happens to the drag reduction and change in power. The actual changes will be lower. At all other speeds investigated, the flow velocity is larger, so that the cavity length is limited by the skeg height. In section 5.8 two shorter cavity lengths are investigated. In that case, the results obtained at 9.07 knots represent a physical air cavity.

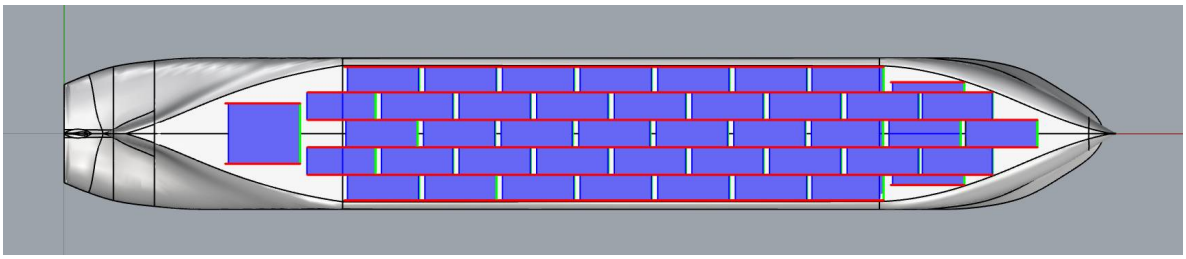

Figure 5.4: Cargo ship: schematic layout of the air cavity system on the bottom of the ship. (Blue: air cavities, Red: skegs, Green: cavitators)

5.5 System appendages

The appendages of the DACS system, the skegs, and the cavitators, also cause an additional increase in resistance. Figure 5.5 shows the actual appendages installed on the general cargo ship. See section 3.2 for a more detailed description of the added resistances due to the appendages. Table 5.5 shows the change in shaft power measured during sea trial after the installation of DACS with air off. From the sea trial measurements, no clear conclusion can be drawn on the added resistance of the system appendages. This is probably due to the uncertainty of the sea trial measurements.

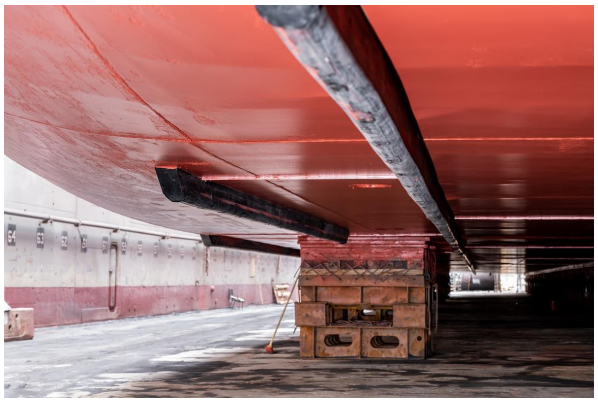

Figure 5.5: DACS appendages installed on the general cargo ship, (Damen Shipyards Group, 2023).

Table 5.5: Cargo ship: change in shaft power measured during sea trials after the installation of DACS with air off.

v_s [kn]	ΔP_s]%]
11.9	2.0
12.5	3.0
12.9	-1.0

A first approximation of the added resistance of the appendages is made, For comparison of the CFD results with air on to the sea trial results with air on. First of all, the added resistance of the skegs with air off is computed using CFD. The computational settings and mesh settings for the CFD simulations of the ship including the skegs are identical to that of the reference case. 11 refinement levels are set for the mesh on the skegs, with as reference length the skeg height. This leads to a mesh with 14.78 mln cells, which is considerably more than the reference case (9.04 mln). This is because multiple skegs are present over the full length of the bottom, see figure 5.4, but the height of the skegs is much lower compared to the their length. Also over the height of the skegs, enough cells should be present. Figure 5.6 shows the surface mesh on one of the skegs.

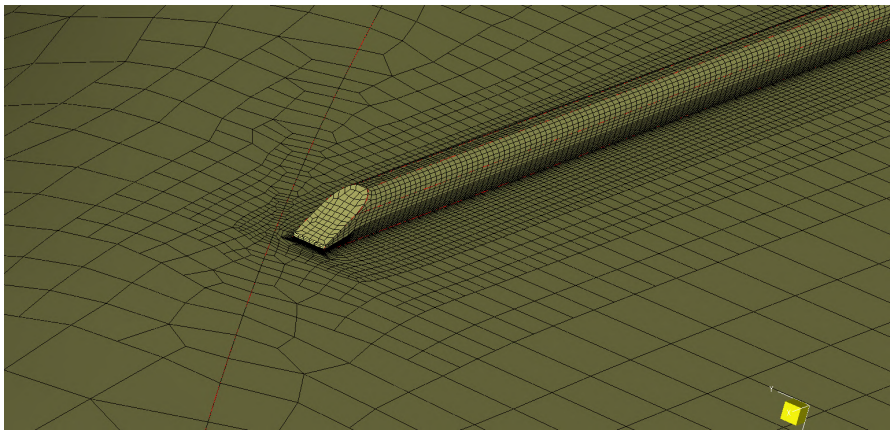

Figure 5.6: Cargo ship: Close up of the surface mesh on one of the skegs.

Table 5.6 compares the ship's resistance between the reference case and the air-off case, determined with CFD. The results show that the skegs cause a 2-3% increase in resistance. Furthermore, one simulation was performed for the air-off case at 12.97, including the actuator disk, to investigate if the skegs affected the thrust deduction. The change in thrust deduction factor between both cases was only 0.1%. The change in nominal wake factor between the reference and air off is approximately 1%. Therefore it is assumed that the thrust deduction effect and the wake factor are not affected by the DACS appendages.

Table 5.6: Cargo ship: comparison of CFD resistance between the reference case and air off (only the skegs included).

	R [kN]			
v_s [kn]	Ref	Air off	Diff. [%]	ΔR [kN]
9.07	79.43	81.64	2.78	2.21
10.67	112.09	115.26	2.83	3.17
11.95	152.05	156.17	2.71	4.12
12.41	181.30	185.08	2.09	3.79
12.97	228.49	232.88	1.92	4.39

With air on the added resistance of the skegs is lower than with air off because in that case the sides of the skegs are partially covered with air which reduces the wetted area, see also section 3.2. An approximation of the effect of the air coverage of the skegs is also made. Zverkhovskyi et al. (2015) stated that the shape of an air cavity can be approximated by a half ellipse. With the given cavity length, thickness, and distance between the cavities the air-covered area of the skegs was approximated to be approximately 47% of the total wetted area of the skegs. This means that the added resistance of the skegs is considerably lower with air on.

Based on this, it is assumed that the added resistance of the skegs with air off equals the total added resistance of the skegs and cavitators together with air on. This would actually mean that the drag of the cavitators with air on equals the wetted area reduction of the skegs. The height of the cavitators is one order of magnitude lower than the height of the skegs. Therefore this assumption seems justified as a first approximation. A more detailed investigation of the added resistance of the cavitators and skegs with air on and air off would require a significant (computational) effort and is out of the scope of the present work.

5.6 Comparison

5.6.1 CFD results

In this section a comparison is made between the CFD results of the reference case and the air on case. Table 5.7 shows a comparison for the different resistance components. The same results are also

depicted graphically in figure 5.7. They show that the resistance is reduced significantly by the air cavities. The reduction (in percentage) is the largest at lower speed. This is because the ratio R_v/R decreases with increasing speed because the wavemaking resistance becomes more dominant. The viscous drag reduction is approximately constant for all speeds. This is due to the constant wetted area reduction. Surprisingly, the pressure resistance of the ship is also reduced by the air cavities. This is investigated in more detail in section 5.6.2. Furthermore, it was observed that the air cavities caused no change in the dynamic trim and sinkage of the ship.

Table 5.7: Cargo ship: CFD results resistance components comparison between the reference case and air on.

	R [kN]			R_p [kN]			R_v [kN]		
v_s [kn]	Ref	Air on	Diff. [%]	Ref	Air on	Diff. [%]	Ref	Air on	Diff. [%]
9.07	79.43	58.48	-26.37	28.57	24.11	-15.62	50.86	34.37	-32.41
10.67	112.09	83.98	-25.08	42.89	37.06	-13.58	69.25	46.92	-32.25
11.95	152.05	118.84	-21.84	66.59	60.91	-8.54	85.51	57.94	-32.25
12.41	181.30	144.55	-20.27	91.86	82.32	-10.38	89.44	62.23	-30.42
12.97	228.49	189.62	-17.01	128.53	121.97	-5.10	99.96	67.65	-32.32

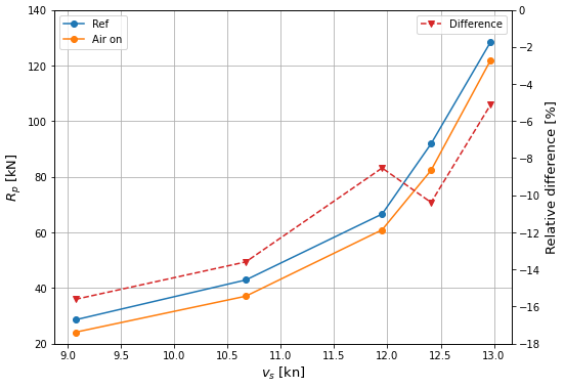

(a) Pressure resistance

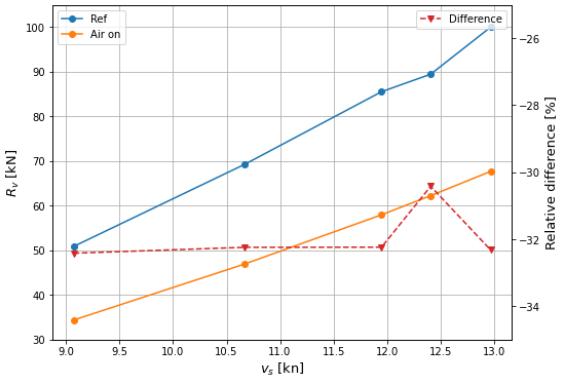

(b) Viscous resistance

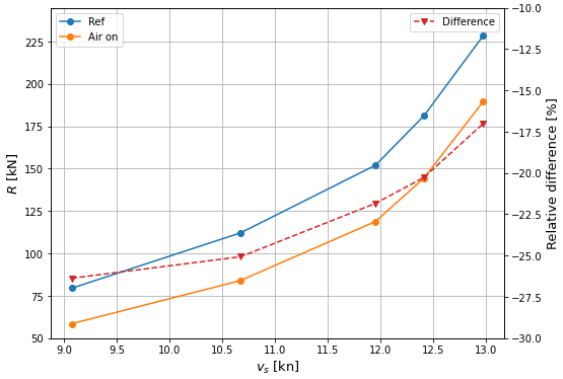

(c) Total resistance

Figure 5.7: Cargo ship: CFD results resistance components comparison between the reference case and air on.

Table 5.8 shows a comparison of the thrust deduction factor and the nominal wake factor, between air on and the reference case. The table shows that the change in the thrust deduction fraction is rather limited. This is also expected because the thrust deduction effect is not related to the boundary layer development over the bottom. Rather, it is present because the propeller suction causes an increased pressure difference and flow velocity at the stern, see also section 2.3.2.

The nominal wake factor however is changed significantly. The wake is approximately 11% lower

with air on. This can be explained in the following way. The boundary layer in the aft region is much thinner due to the air cavities. Due to the air it could not grow as much as it would have done without the air cavities. As a result, the average axial velocity in the wake field is higher. The boundary layer development along the hull is also plotted in figure 5.9. The figure shows a much thinner boundary layer in the stern region when air cavities are present. Figure 5.19 shows the nominal wake field of the ship at 12.97 knots with and without air cavities on the bottom of the ship. The figure shows that the structure of the wake field is approximately similar. However, for the case with air on the axial velocity is higher

Table 5.8: Cargo ship: comparison of the CFD results of the self-propulsion parameters between the reference case and air on.

	$(1-t)$			$(1-w_n)$		
v_s [kn]	Ref	Air on	Diff. [%]	Ref	Air on	Diff. [%]
9.07	0.810	0.806	-0.45	0.610	0.682	11.79
10.67	0.809	0.804	-0.57	0.614	0.684	11.50
11.95	0.809	0.805	-0.55	0.617	0.685	11.15
12.41	0.812	0.806	-0.70	0.614	0.683	11.33
12.97	0.815	0.813	-0.16	0.607	0.677	11.53

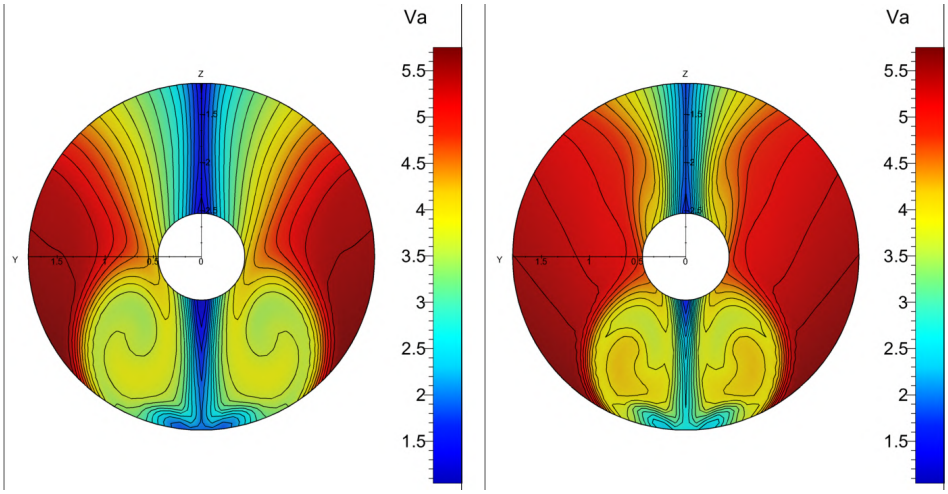

(a) Reference *(b) Air on*

Figure 5.8: Cargo ship: comparison of the nominal wake field at 12.97 knots.

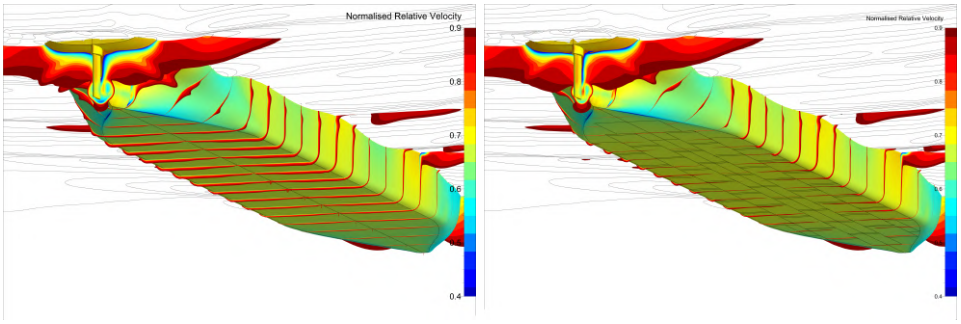

(a) Reference *(b) Air on*

Figure 5.9: Cargo ship: comparison of the boundary layer development (contours of normalized velocity) along the hull at 12.97 knots

5.6.2 Pressure drag reduction

Table 5.7 showed that the pressure drag was also reduced by the air cavities. Clearly a reduction is noticed for all speeds. The reduction tends to decrease with increasing speed. It should be noted, that the grid convergence study showed that there is a considerable numerical uncertainty of 9.5% present for the pressure resistance. However, especially at lower speeds a reduction of up to 15% is noticed which is larger than the numerical uncertainty. No change in the wave profile was noticed with the air cavities so the wave resistance is not affected. Therefore the reduction in pressure resistance is caused by the reduction in viscous pressure resistance. This also explains why the reduction in pressure is larger at lower speeds. At lower speed the importance of the wavemaking resistance is lower.

The hydrodynamic pressure on the ship hull is similar when comparing the reference case with air on, except for the region near the stern. Figure 5.10 shows that the pressure is larger with air on than without air for the region above the gondola. Figure 5.11 shows a comparison of the flow separation being present in the stern region. The figure shows that the amount of flow separation is reduced in the same region where an increase in pressure is observed.

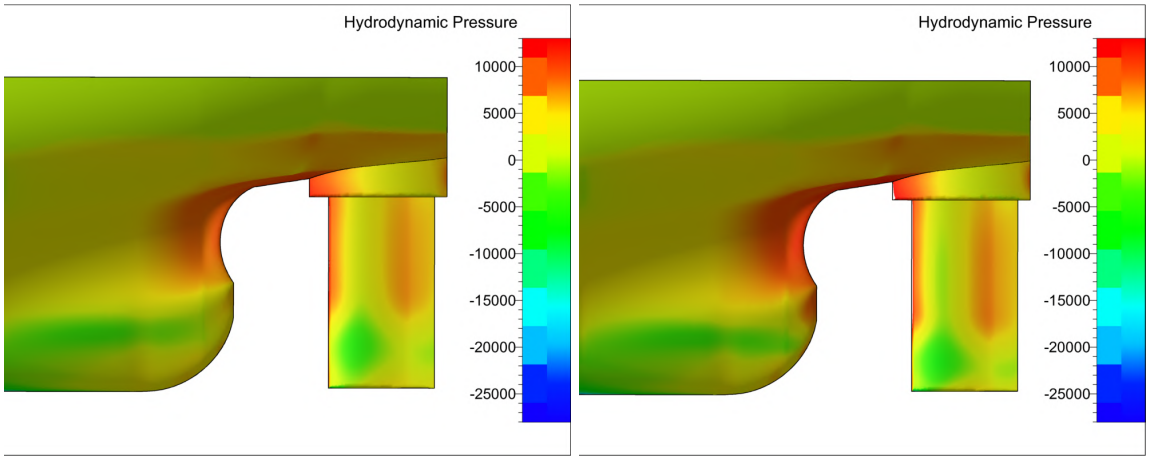

(a) Reference *(b) Air on*

Figure 5.10: Cargo ship: comparison of the hydrodynamic pressure in the stern region at 12.97 knots.

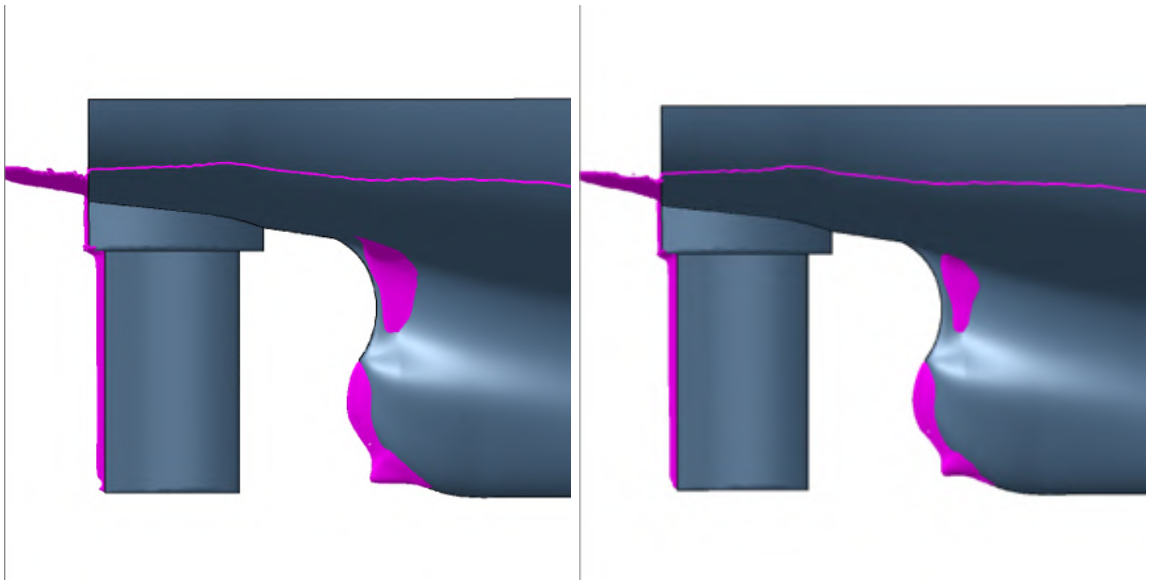

(a) Reference *(b) Air on*

Figure 5.11: Cargo ship: comparison of instantaneous separation in the stern region at 12.97 knots.

This effect can be explained in the following way. Figure 5.12 shows the pressure distribution on a 2D geometry (representing a 2D cut of a ship hull), (Larsson & Raven, 2010). The figure shows that the pressure at the bow and stern is similar for inviscid flow. Consequently, no pressure drag is present. The figure also shows that when a viscous flow is present there is a lower pressure present at the stern. This is because, in a viscous fluid, a boundary layer will develop over length. This will cause an outward displacement of the streamlines at the stern. The streamlines have less curvature and therefore a smaller pressure variation across the streamlines and thus a lower pressure at the stern is present than in an inviscid flow. The difference between the pressure at the bow and stern causes a drag force also known as viscous pressure resistance. When the curvature at the stern is too high the flow will separate. This causes an even larger reduction in pressure at the stern and therefore a larger viscous pressure drag. Generally, a thicker boundary layer will separate more easily than a thinner boundary layer. (Larsson & Raven, 2010).

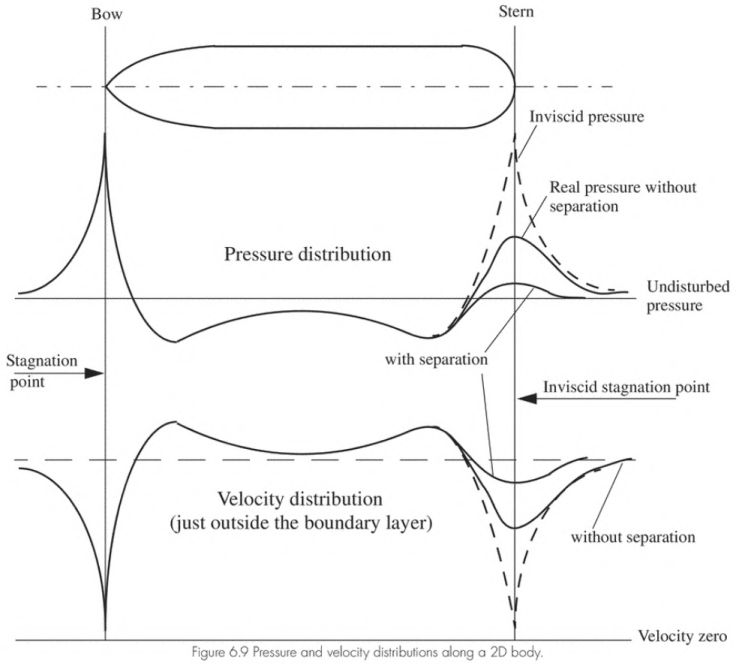

Figure 5.12: Pressure and velocity distribution around a 2D geometry (representing a ship hull) in both viscous and inviscid flow, (Larsson & Raven, 2010).

When air cavities are present they limit the growth of the boundary layer on the bottom resulting in a thinner boundary layer at the stern. Figure 5.13 shows the streamlines in the stern region of the general cargo ship. From the figure, it can be seen that the flow over the (upper region) of the gondola comes from the bottom. Therefore, the boundary layer will be thinner in this area due to the air cavities resulting in less flow separation.

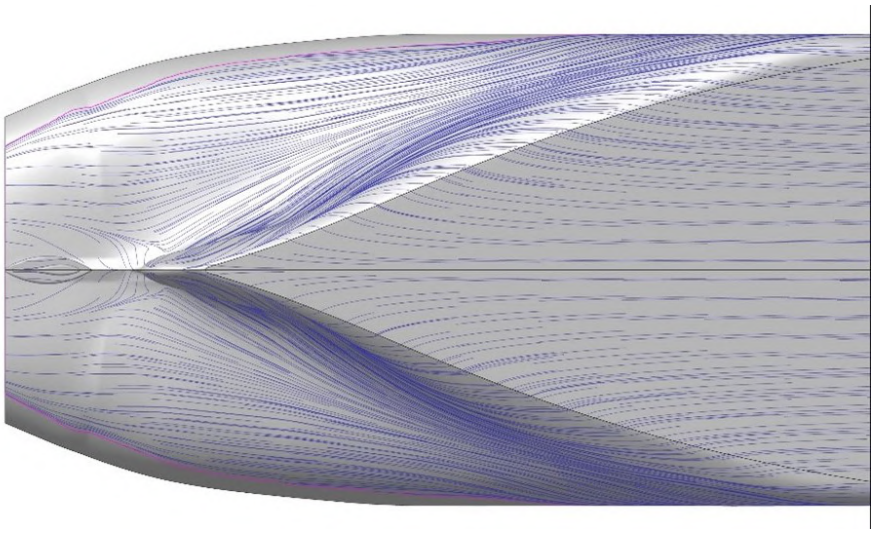

Figure 5.13: Cargo ship: bottom view of the streamlines at the stern, at 12.97 knots.

This could be a possible explanation for the reduction in pressure resistance caused by the air cavities. It should be noted however that a ship hull is a 3D geometry so also 3D boundary layer effects play a role. Furthermore, it is questionable whether the flow separation at the gondola is accurately resolved with a quasi-static simulation and the k-omega SST turbulence model with wall functions. Therefore further research is required to investigate the possible reduction in flow separation caused by air cavities in more detail.

Zverkhovskyi (2023) also performed CFD simulations of a ship with air cavities modeled as slip surfaces. For this ship, no change in the pressure resistance was observed. A possible reason for this could be that this ship has no flow separation at the stern. However one would say based on the explanation above that the air cavities cause a thinner boundary layer at the stern and reduce the outward displacement of the streamlines. This should also slightly reduce the viscous pressure resistance. However, this is not observed in this paper. Also for the cruise ship, see section 6.5, little change in pressure resistance is observed. However, this ship has a much more slender hull form and a lower air-covered area meaning that the boundary layer at the stern is affected less by the air cavities. Furthermore, no flow separation is present at the stern for this ship. Reduced flow separation at the stern was also observed in literature by Sverchkov and Borusevich (2019). A reduction of the amount of flow separation present in the wake field was measured during model tests of an inland ship equipped with an internal air cavity drag reduction system.

5.6.3 Power speed comparison

A power speed computation was also made for both the reference case and the case with air on. The results are shown in tables 5.9, 5.10 and 5.11. The tables show that the reduction in shaft power due to the air cavities is significantly lower than the reduction in resistance. The difference is especially striking at lower speeds. This can be explained by considering the change in propulsive efficiency. Table 5.11 shows that the propulsive efficiency is reduced for all speeds due to the air cavities. The propulsive efficiency is computed from the hull and the open water efficiency. The hull efficiency has a constant reduction of approximately 11% for all speeds due to the reduction in wake fraction. However, the open water efficiency shows a reduction at low speed and an increase at higher speeds. Such a propeller is the most efficient in the design condition. In off-design conditions, the efficiency of the ship decreases more rapidly than for a fixed-pitch propeller because the propeller keeps operating at the same rpm, (Klein Woud & Stapersma, 2017). Therefore the change in propeller efficiency is also larger. Whether the propeller efficiency increases or decreases depends on the location of the propeller working point in the open water diagram. This is explained in more detail in section 8.1. It should be noted that this ship typically sails at a speed of 12-13 knots. At those speeds an increase in propeller efficiency is observed.

Table 5.9: Cargo ship: comparison of corrected resistance R_{cor} and shaft power P_s, predicted using CFD, between the reference case and air on.

	R_{cor} [kN]			P_s [kW]		
v_s [kn]	Ref	Air on	Diff. [%]	Ref	Air on	Diff. [%]
9.07	82.84	63.77	-23.02	1093.7	1017.5	-6.96
10.67	118.07	92.21	-21.90	1355.5	1223.8	-9.72
11.95	160.62	130.74	-18.60	1780.6	1594.6	-10.45
12.41	190.91	156.32	-18.12	2077.7	1844.7	-11.21
12.97	239.47	202.86	-15.29	2598.0	2312.0	-11.01

Table 5.10: Cargo ship: comparison of the propeller pitch ratio P/D and the open water efficiency η_o, predicted using CFD, between the reference case and air on.

	P/D [-]			η_o [-]		
v_s [kn]	Ref	Air on	Diff. [%]	Ref	Air on	Diff. [%]
9.07	0.379	0.373	-1.35	0.266	0.247	-7.09
10.67	0.465	0.458	-1.50	0.363	0.352	-3.00
11.95	0.557	0.552	-0.90	0.423	0.429	1.58
12.41	0.608	0.597	-1.73	0.443	0.458	3.38
12.97	0.679	0.666	-1.78	0.459	0.488	6.33

Table 5.11: Cargo ship: comparison of the hull efficiency η_h and the propulsive efficiency η_d, predicted using CFD, between the reference case and air on,

	η_h [-]			η_d [-]		
v_s [kn]	Ref	Air on	Diff. [%]	Ref	Air on	Diff. [%]
9.07	1.327	1.182	-10.95	0.353	0.292	-17.26
10.67	1.317	1.175	-10.82	0.478	0.414	-13.49
11.95	1.312	1.174	-10.53	0.555	0.504	-9.11
12.41	1.323	1.180	-10.80	0.587	0.541	-7.78
12.97	1.341	1.201	-10.48	0.615	0.585	-4.81

5.7 Comparison to sea trial

The reduction in shaft power caused by the air cavities is predicted using CFD. It was also measured during sea trials. A comparison is made between both prediction methods. The sea trials for the reference case and the case with air on were not performed at the exact same speeds:

- Speeds reference case: 9.07, 10.67, 11.95, 12.41 and 12.97
- Speeds air on: 11.24, 11.86, 12.46, 12.95

A comparison should be made at the same speed. Therefore the results of the case with air on are interpolated to the speeds of the reference case. In this way, a comparison is only made at 11.95, 12.41, and 12.97 knots. For comparison at 10.67 knots, the curve should be extrapolated which gives rise to substantial uncertainty, therefore this point is omitted. The result of 12.95 knots is extrapolated to 12.97. This is an extrapolation of only 0.02 knots which is deemed acceptable. Table 5.12 shows the comparison for shaft power reduction predicted using CFD and measured during sea trials. The results are also depicted in figure 5.14. For CFD results are also present at lower speeds but no comparison with the sea trial results can be made for those data points.

Table 5.12: Cargo ship: comparison of the change in shaft power due to DACS. The comparison is made both for the sea trial measurements and the CFD results.

	Sea trial			CFD		
v_s [kN]	$P_{s,ref}$ [kW]	$P_{s,airon}$ [kW]	ΔP_s [%]	$P_{s,ref}$ [kW]	$P_{s,airon}$ [kW]	ΔP_s [%]
9.07	1095.1	-	-	1093.7	1017.5	-6.96
10.67	1456.0	-	-	1355.5	1223.8	-9.72
11.95	2011.8	1904.8	-5.32	1780.6	1594.6	-10.45
12.41	2398.8	2226.8	-7.17	2077.7	1844.7	-11.21
12.97	3009.9	2809.4	-6.66	2598.0	2312.0	-11.01

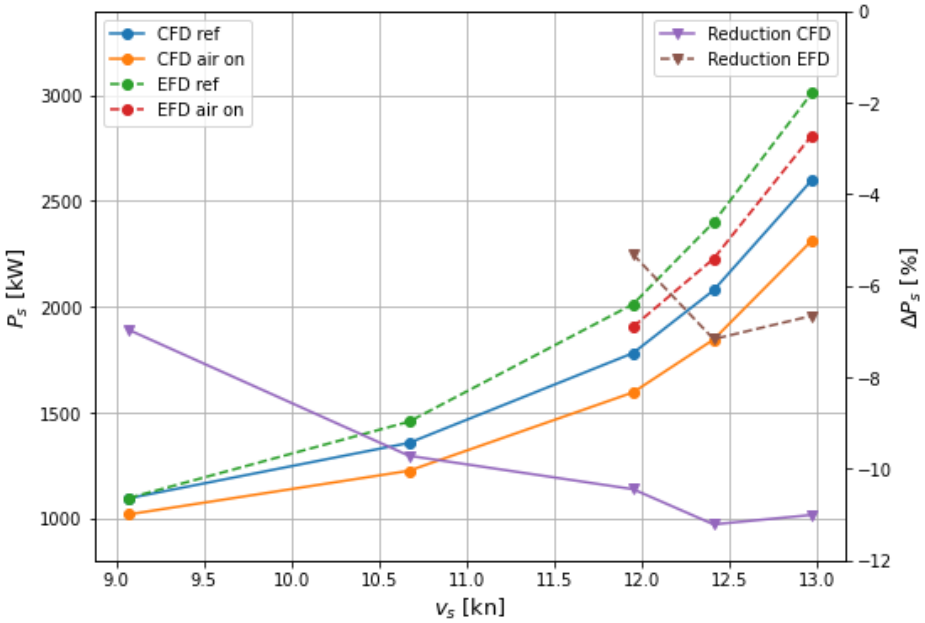

Figure 5.14: Cargo ship: comparison of shaft power for air on and the reference case, predicted with CFD and measured during sea trials (EFD).

The data shows that for both the CFD results and the sea trial results the measured differences are larger than the uncertainty of the predictions (10.2% for CFD and 5% for the sea trials), see also chapter 4. This shows that the air cavity system is capable of reducing the required power of the cargo ship. However, a big difference is visible between the reduction predicted using CFD and the measured prediction (5-7% vs 10-11%). There could be multiple reasons for this difference. The first reason could be the uncertainty of both the sea trial and the CFD predictions. However, for both methods no larger scatter in the data is visible. Another reason could be the prediction of the added resistance of the appendages with air on. It was approximated based on the added resistance of the skegs with air on. This is only a simple approximation, however, it is not expected that this approximation causes a difference of up to 5% in power savings between CFD and sea trials. For the cruise ship an added resistance of only 2% was measured with air off during the model tests, see section 6.4.

Besides this, the difference could also be caused by a possible difference in hull roughness before and after the installation of the DACS system. However, due to the low fouling pressure in the Baltic Sea it is not expected that this will have a big impact, see also section 5.5. A last reason could be the prediction of the air-covered area on the bottom of the ship. It could be that not all air cavities were formed correctly. Another option could be that the average cavity length was lower than predicted. During the sea trial, no monitoring of the air cavities was performed. The cavity length was predicted, assuming that the air cavities have a constant aspect ratio. This assumption is in line with the experimental findings of Zverkhovskyi (2014). However, during recent experimental measurements of Damen, it was found that the cavity thickness and aspect ratio differ for different types of cavitators. This is in contrast with the findings from Zverkhovskyi (2014). For the general cargo ship, the cavity

length could be shorter if the aspect ratio of the cavities is lower than predicted (meaning that the air cavities are thicker). In that case, air escapes over the skegs, which limits the growth of the cavities.

5.8 Shorter cavities

Based on the discussion above it seems most likely that the difference in power reduction predicted by sea trials and CFD is caused by the prediction of the cavity length. However, it could also be a combination of multiple different effects. In this section, a variation in the cavity length is made to quantify the influence of the cavity length. Three different cases are investigated:

- The original assumed cavity length;
- A 13% shorter cavity length;
- A 26% shorter cavity length

Figure 5.18 shows the cavity layout for the three different cases. Some properties of the three cases are shown in table 5.13.

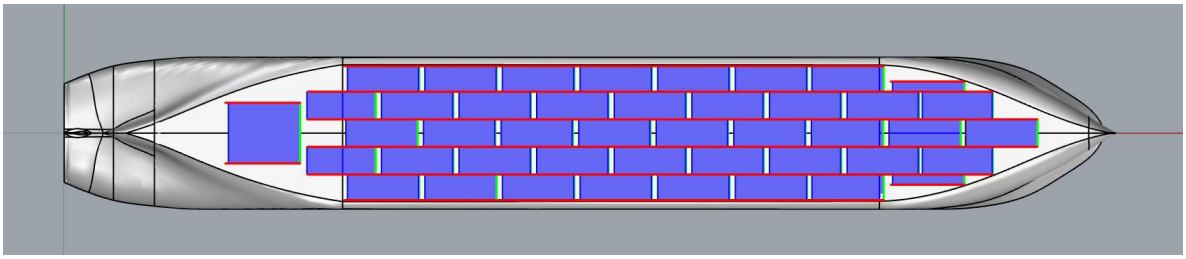

Figure 5.15: Original cavity length

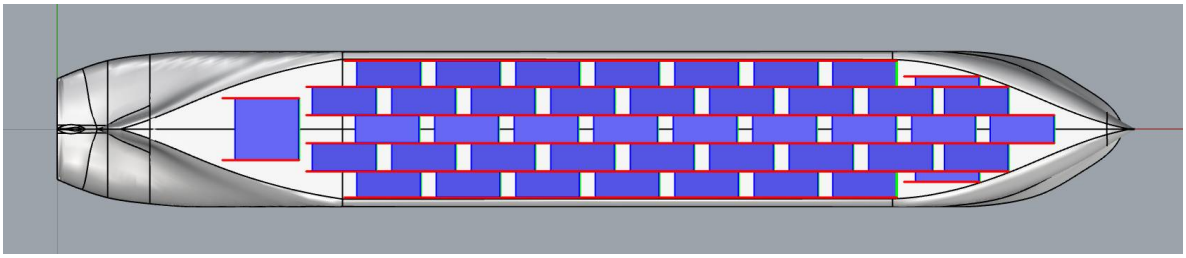

Figure 5.16: 13% shorter length

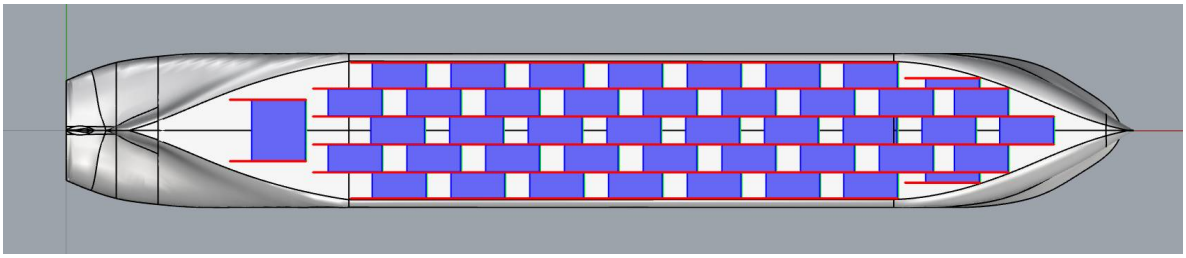

Figure 5.17: 26% shorter length

Figure 5.18: Cargo ship: schematic layout of the air cavity system on the bottom for different cavity lengths. (Blue: air cavities, Red: skegs, Green: cavitators)

Table 5.13: Cargo ship: properties of the three different cavity layouts.

Case	S_{cav}/S_{bottom} [-]	S_{cav}/S_{wet} [-]
Original	0.587	0.285
13% shorter	0.689	0.334
26% shorter	0.792	0.384

5.8.1 Results

The CFD simulations were repeated for the two other cavity lengths. In section 5.6 it was shown that the thrust deduction effect was almost not affected by the air cavities. Therefore only resistance simulations were performed for the shorter air cavities. A comparison for the resistance components and the nominal wake factor is made in tables 5.14, 5.15, 5.16 and 5.17. In these tables "Air on 100%" refers to the case air on with a cavity length of 100& and so on. Similar trends can be observed for the shorter cavities as for the original approximated cavity lengths, see also section 5.6. However, with decreasing cavity length all changes due to the air cavities reduce, which is also expected.

Table 5.14: Cargo ship: change in total resistance for different cavity lengths, compared to the reference case.

	R [kN]						
v_s [kn]	Ref	Air on 100%	Diff. [%]	Air on 87%	Diff. [%]	Air on 74%	Diff. [%]
9.07	79.43	58.48	-26.37	61.74	-22.28	63.24	-20.38
10.67	112.09	83.98	-25.08	88.24	-21.27	92.96	-17.07
11.95	152.05	118.84	-21.84	124.08	-18.39	129.77	-14.66
12.41	181.30	144.55	-20.27	149.70	-17.43	155.97	-13.97
12.97	228.49	189.62	-17.01	194.89	-14.70	201.49	-11.82

Table 5.15: Cargo ship: change in pressure resistance for different cavity lengths, compared to the reference case.

	R_p [kN]						
v_s [kn]	Ref	Air on 100%	Diff. [%]	Air on 87%	Diff. [%]	Air on 74%	Diff. [%]
9.07	28.57	24.11	-15.62	24.59	-13.92	23.48	-17.84
10.67	42.84	37.06	-13.48	37.61	-12.21	38.80	-9.43
11.95	66.54	60.91	-8.46	61.58	-7.46	62.93	-5.42
12.41	91.86	82.32	-10.38	82.57	-10.11	84.19	-8.35
12.97	128.53	121.97	-5.10	121.93	-5.14	123.46	-3.94

Table 5.16: Cargo ship: change in viscous resistance for different cavity lengths, compared to the reference case.

	R_v [kN]						
v_s [kn]	Ref	Air on 100%	Diff. [%]	Air on 87%	Diff. [%]	Air on 74%	Diff. [%]
9.07	50.86	34.37	-32.41	37.14	-26.97	39.77	-21.81
10.67	69.25	46.92	-32.25	50.64	-26.88	54.16	-21.79
11.95	85.51	57.94	-32.25	62.51	-26.90	66.84	-21.84
12.41	89.44	62.23	-30.42	67.13	-24.94	71.78	-19.75
12.97	99.96	67.65	-32.32	72.96	-27.01	78.03	-21.94

Table 5.17: Cargo ship: change in nominal wake factor for different cavity lengths, compared to the reference case.

	$(1 - w_n)$ [-]						
v_s [kn]	Ref	Air on 100%	Diff. [%]	Air on 87%	Diff. [%]	Air on 74%	Diff. [%]
9.07	0.610	0.682	11.79	0.670	9.73	0.660	8.13
10.67	0.614	0.684	11.50	0.672	9.47	0.662	7.92
11.95	0.617	0.685	11.15	0.673	9.14	0.664	7.62
12.41	0.614	0.683	11.33	0.671	9.33	0.661	7.72
12.97	0.607	0.677	11.53	0.666	9.63	0.656	7.96

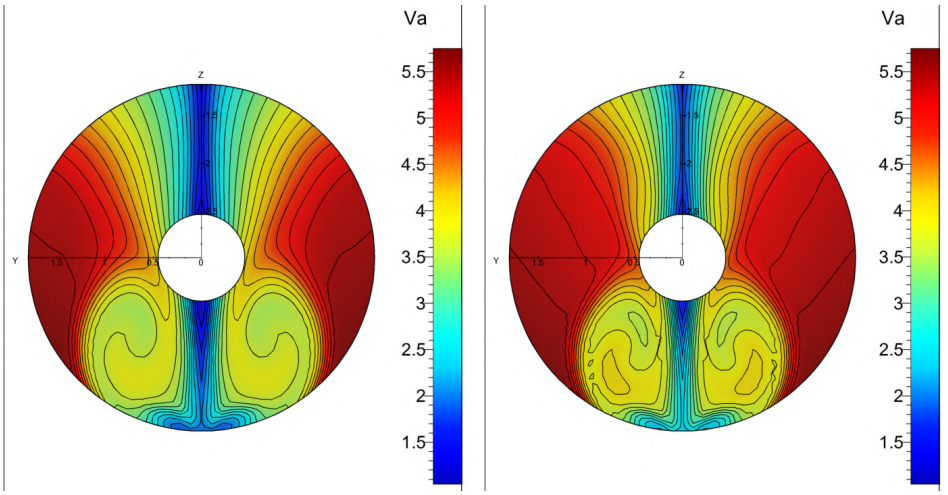

(a) Reference

(b) 74% cavity length

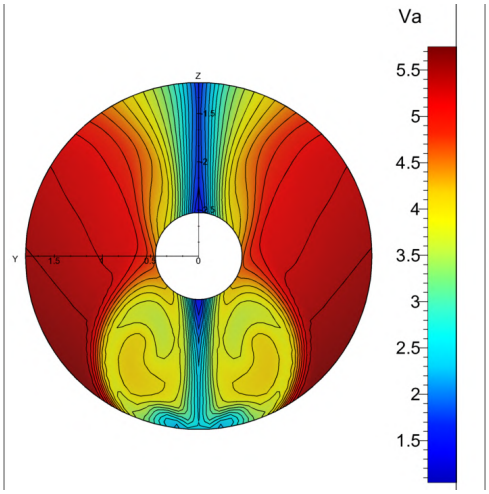

(c) 87% cavity length

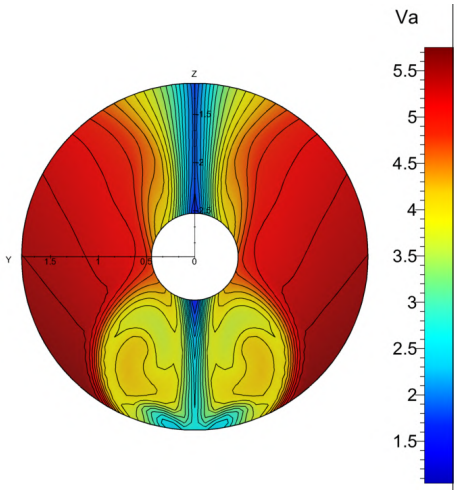

(d) 100% cavity length

Figure 5.19: Cargo ship: comparison of the nominal wake field at 12.97 knots for different cavity lengths.

5.8.2 Power speed comparison

A comparison is also made on the effect of the cavity length on the power speed prediction. Tables 5.18, 5.19, 5.20 and 5.21 show a comparison for corrected resistance, open water efficiency, and propulsive efficiency. In these tables "Air on 100%" refers to the case air on with a cavity length of 100& and so on. Again similar trends are visible for all cavity lengths. All changes increase if the cavity length is larger.

Table 5.18: Cargo ship: change in corrected resistance for different cavity lengths, compared to the reference case.

	R_{cor} [kN]						
v_s [kn]	Ref	Air on 100%	Diff. [%]	Air on 87%	Diff. [%]	Air on 74%	Diff. [%]
9.07	82.84	63.77	-23.02	67.07	-19.04	68.62	-17.16
10.67	118.07	92.21	-21.90	96.61	-18.18	101.45	-14.07
11.95	160.62	130.74	-18.60	136.20	-15.20	142.10	-11.53
12.41	190.91	156.32	-18.12	161.72	-15.29	168.25	-11.87
12.97	239.47	202.86	-15.29	208.44	-12.96	215.34	-10.08

Table 5.19: Cargo ship: change in open water efficiency for different cavity lengths, compared to the reference case.

	η_o [-]						
v_s [kn]	Ref	Air on 100%	Diff. [%]	Air on 87%	Diff. [%]	Air on 74%	Diff. [%]
9.07	0.266	0.247	-7.09	0.251	-5.61	0.252	-5.32
10.67	0.363	0.352	-3.00	0.355	-2.29	0.359	-1.03
11.95	0.423	0.429	1.58	0.429	1.55	0.431	1.87
12.41	0.443	0.458	3.38	0.456	2.87	0.456	2.75
12.97	0.459	0.488	6.33	0.484	5.45	0.480	4.69

Table 5.20: Cargo ship: change in propulsive efficiency for different cavity lengths, compared to the reference case.

	η_d [-]						
v_s [kn]	Ref	Air on 100%	Diff. [%]	Air on 87%	Diff. [%]	Air on 74%	Diff. [%]
9.07	0.353	0.292	-17.26	0.304	-13.98	0.309	-12.44
10.67	0.478	0.414	-13.49	0.427	-10.75	0.438	-8.29
11.95	0.555	0.504	-9.11	0.516	-6.96	0.525	-5.34
12.41	0.587	0.541	-7.78	0.552	-5.91	0.560	-4.62
12.97	0.615	0.585	-4.81	0.592	-3.82	0.596	-3.03

Table 5.21: Cargo ship: change in shaft power for different cavity lengths, compared to the reference case.

	P_s [kW]						
v_s [kn]	Ref	Air on 100%	Diff. [%]	Air on 87%	Diff. [%]	Air on 74%	Diff. [%]
9.07	1093.7	1017.5	-6.96	1029.4	-5.88	1034.7	-5.39
10.67	1355.5	1223.8	-9.72	1242.7	-8.32	1270.1	-6.30
11.95	1780.6	1594.6	-10.45	1622.8	-8.86	1664.3	-6.53
12.41	2077.7	1844.7	-11.21	1870.6	-9.97	1919.6	-7.61
12.97	2598.0	2312.0	-11.01	2351.0	-9.51	2409.2	-7.27

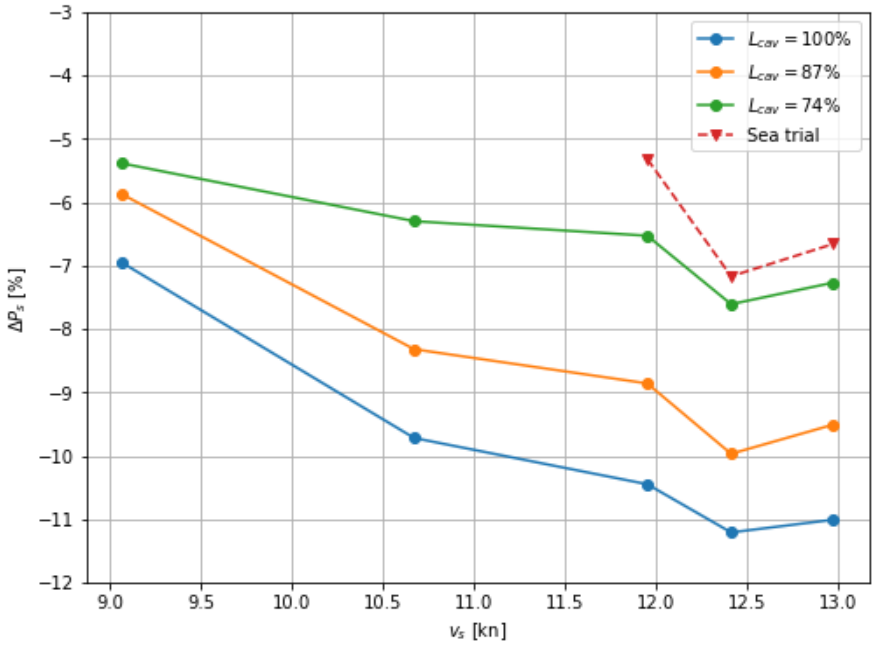

Figure 5.20: Cargo ship: shaft power reduction for different cavity lengths

Figure 5.20 and table 5.21 show the reduction in shaft power for different cavity lengths and also from the sea trial measurements. They show the CFD results are much closer to the sea trial measurements with a 26% shorter cavity length. However, both methods have considerable uncertainty, therefore it is not possible to predict the actual shape of the cavities formed on the bottom accurately. But most likely, the air-covered area of the bottom is significantly lower than originally predicted. This claim can also be supported by the sensitivity analysis, see section 4.2.2. That analysis showed that the thrust prediction has the largest influence on the uncertainty of the power prediction.

5.9 Conclusion

The following conclusions were made for the general cargo ship. Next to a reduction in frictional drag due to the wetted area caused by the cavities, also a reduction in pressure drag was found. Probably this is caused because flow separation on the gondola is reduced by the air cavities. Furthermore, it was found that the power reduction caused by the air cavities was lower than the resistance reduction. This is because the propulsive efficiency is also decreased. The reduction in propulsive efficiency is caused because the wake fraction is influenced significantly by the air cavities due to a different boundary layer development on the bottom. The air cavities also cause a change in propeller efficiency. It decreases at low speeds and increases at higher speeds. The air cavities only had a minor impact on the thrust deduction effect.

A comparison was also made between the CFD results and sea trial data. It was found that the power is underpredicted when using CFD, especially at higher speeds. Next to this, a larger reduction in power due to the air cavities was predicted with CFD than measured during the sea trials. Most likely the wetted area reduction is lower than predicted. Therefore a comparison was also made between three different cavity lengths. It was observed that also changes caused by the air cavities reduce for shorter air cavities.

Chapter 6
Cruise ship

6.1 Description

This case study is performed on a cruise vessel. The ship is a 220-passenger luxury expedition cruise ship. The ship is different to the other two vessels that are studied because it has a more slender hull shape, and also a smaller flat bottom area. Therefore it is an interesting case study for the project to investigate the effects of the air cavity system for a more slender vessel.

Table 6.1 shows some general properties of the vessel. Figure 6.1 shows the hull shape of the vessel. The figures are retrieved from a model test report of the ship. The figure also shows that the ship is a twin-screw vessel with podded propulsion. Table 6.2 shows the primary dimensions of the propellers.

Table 6.1: Cruise ship: general properties

Length L_{wl} [m]	160.7
Beam B [m]	21.4
Draft T [m]	5.15
Displacement Δ [ton]	11844.7
Block coefficient C_b [-]	0.652

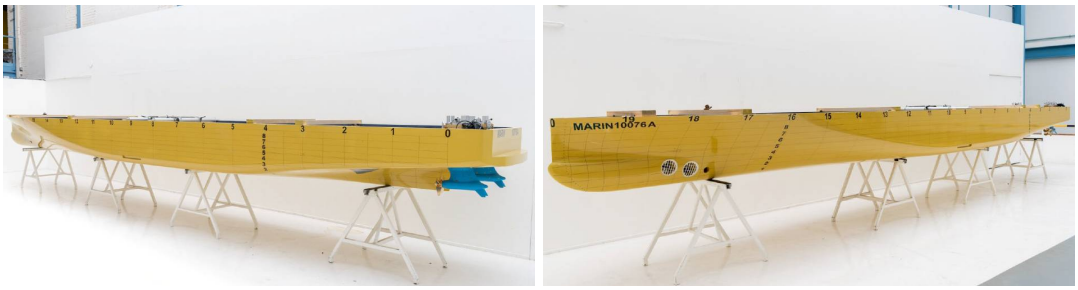

Figure 6.1: Cruise ship: overview of the model.

Table 6.2: Cruise ship: propeller properties.

Diameter D [m]	3.6
Pitch ratio P/D	1.215
Blade area ratio A_e/A_0	0.544
Number of blades	45
# propellers k_p	2

6.2 Model tests

Model tests of the cruise ship were performed at the Maritime Research Institute Netherlands (MARIN). The investigation aimed to optimize and determine the gain in propulsive power of the Damen Air Cavity System (DACS). Resistance and propulsion tests were performed. Also, some runs were made with an underwater camera being present. Propeller open water tests were already performed earlier. Three cases were investigated:

- Reference case
- Ship including DACS appendages but with air off

- Air on

The measurements for the reference case were performed for the speeds 9-17 knots in steps of 1 knot. For the air off and air on case measurements were only performed at 11, 14, and 17 knots. For those cases, only self-propulsion tests were performed. The model tests for the reference case were performed earlier. For that case also resistance tests were performed.

6.2.1 Scale effects

The results of the resistance and propulsion tests have been extrapolated to full-scale values according to the so-called "MARIN form-factor method". This method approximately follows the ITTC 1978 performance prediction method, (ITTC, 2017a). The results were presented for the ideal trial condition of the ship. Additional allowances to the resistance were added for roughness (125 μm AHR) and for wind resistance (wind coefficient $C_x = 0.8$ and Frontal area $A_T = 321\ m^2$). Furthermore, an additional correlation factor was added accounting for the bilge keels which were not present during the model tests. Lastly, a correlation factor is added which is based on statistical analysis of previous model tests and sea trial results.

The model report states that the correlation values reflect the true average involving a 50 percent probability that the actual ship's speed will be less than predicted. Therefore a small additional allowance is usually added to be on the conservative side. It should also be noted that during the propulsion tests, larger scale effects than usual were found. This is due to low Reynolds effects on the propeller blades. Therefore additional scale effect corrections have been applied.

For the extrapolation of the tests with airflow the extrapolation procedure of the resistance and propulsion tests was slightly different. In this process, several assumptions were made. First of all, it was assumed that the wave resistance and the form drag are not changed by the air lubrication system. Furthermore, for the case with air flow on propulsion tests were performed. Therefore the resistance value is calculated based on the thrust values, assuming that the thrust deduction is not changed by the air lubrication. Also, an additional scale correction is applied accounting for the fact that the boundary layer development is interrupted by the air cavities and therefore the frictional coefficient will increase. This affects the scale effects on frictional resistance.

Lastly for the case with airflow and for the reference case including the DACS appendages an additional correction was made. The height of the cavitators is not scaled geometrically between model scale and full scale. In fact, the cavitor height on model scale was too high. The drag contribution of the additional cavitator height in the model tests was computed based on internal research at MARIN.

6.2.2 Observations

During the tests, several interesting observations were made. Using the underwater camera it was observed that the volume of air bubbles shedding from the air cavities is rather small and seems not to enter the propeller plane. The air bubbles shedding from the cavities follow the hull. This can be seen in figure 6.2. This observation is in agreement with other findings from literature on the possible air inflow into the propeller plane due to air lubrication, see also section 2.6. From this observation, it can be concluded that the propeller efficiency is not influenced by air bubbles entering the propeller plane.

Figure 6.2: Cruise ship: propeller observations with air on at 14 knots during model tests.

Furthermore, it was observed that the air cavities were shorter than expected. The reason for this is that the aspect ratio of the air cavities was lower than expected (the cavities were thicker). As a result, the air leaked sideways over the skegs, which prevented the growth of the cavities, see also figure 6.3. This effect leads to a large area in between the end of the cavity and the next cavitator that was not covered by air, making the system less efficient. To improve the system's performance the distance between the cavitators (in longitudinal direction) was reduced. This increases the air-covered area and the drag reduction.

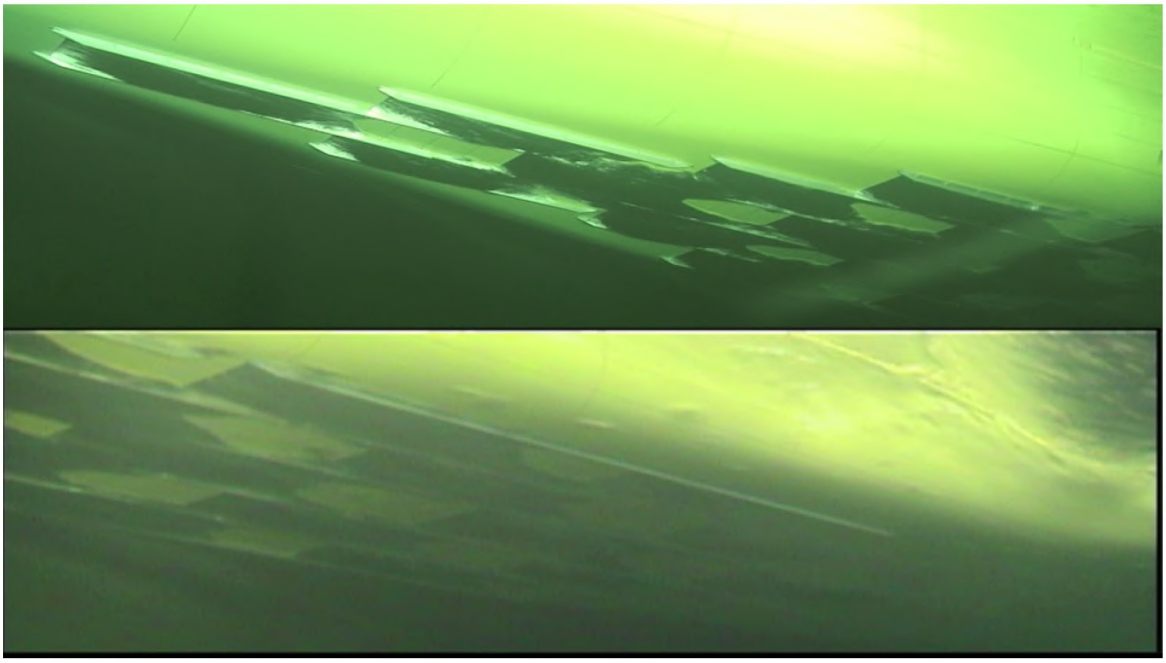

Figure 6.3: Cruise ship: picture made with an underwater camera during the model tests at 14 knots, for the first version of cavity layout.

6.3 Reference case

First of all, CFD simulations of the reference case (the ship without airflow and DACS appendages) were performed. The investigated speeds are 9,11,14,17 and 19 kn. The speed range was chosen in such a way that the model test measurements were covered and also such that the flow around the vessel could be investigated over a broad speed range. The hull geometry used is identical to the one used for the model tests. However, not all appendages that were present during the model tests are included in the simulations. During the model tests the following appendages were present:

- Two bow thruster tunnels
- One anti-suction tunnel
- One stabilizer fin recess on both sides of the vessel
- Two pods
- Two headboxes for the pods

The bow thrusters were not included in the CFD model. The reason for this is that the bow thrusters are covered by a grid. It would require a very fine mesh in that region to accurately resolve the flow. However, it is expected that the bow thrusters will not affect the wake field and the flow over the bottom. Therefore it seemed acceptable to neglect the bow thrusters in the CFD model. The headboxes for the pods were also not included in the CFD model. This is because their geometry could not be retrieved. In the available geometry of the pod, a different connection between the pod and the hull was present. Figure 6.4 shows the difference between the CFD geometry and the ship model. The headboxes have a larger wetted area, so they will have a larger frictional drag. However, the pod shaft is a blunt body and will probably cause the flow to separate behind, leading to some additional pressure drag. The pod shafts are located at the stern so it is not expected that they will influence the wake field and the flow over the bottom. All other appendages were included.

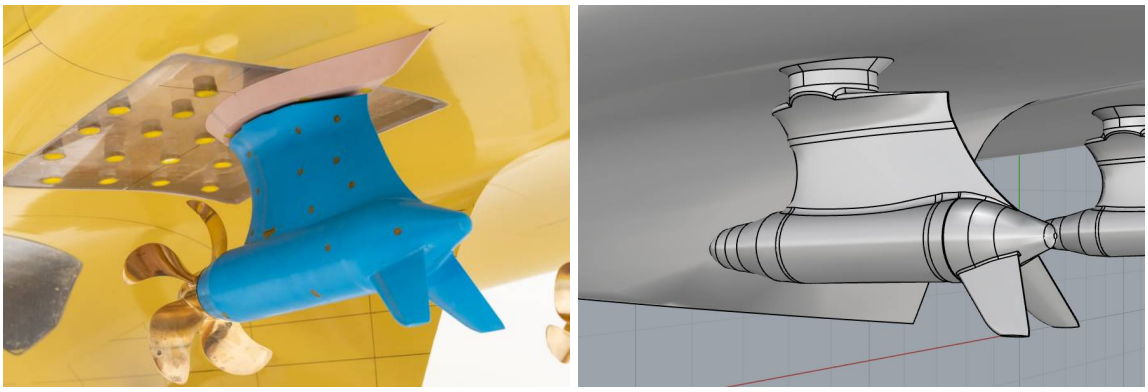

Figure 6.4: Cruise ship: pod and headbox in the model test and the CFD geometry.

Table 6.3 shows the CFD results of the cruise ship before the installation of the air cavity system. The results show that the biggest portion of the ship's resistance is of a viscous nature. However, with increasing speed, the fraction of viscous resistance over total resistance decreases. Furthermore, the ship has a low (nominal) wake factor and thrust deduction factor. This is because the ship is a twin-screw vessel. Their values are comparable to that of other twin-screw vessels described in literature, (Larsson & Raven, 2010). Figure 6.5 shows the nominal wake field of the ship at 17 knots. The figure shows that the wake field is asymmetric. This is because the ship is a twin-screw vessel. Furthermore, it is visible that the velocity in the wake field is close to the freestream velocity, especially in the bottom part of the wakefield. This is due to the location of the propeller, which is located for a large part outside of the ship's boundary layer. Consequently, the nominal wake fraction w_n is rather low.

Table 6.3: Cruise ship reference case: CFD results.

v_s [kn]	Fr [-]	R [kN]	R_p [kN]	R_v [kN]	R_v/R [-]	(1-w_n) [-]	(1-t) [-]
9	0.12	96.12	21.46	74.66	0.78	0.914	0.914
11	0.14	143.45	34.42	109.03	0.76	0.914	0.911
14	0.18	232.00	59.36	172.64	0.74	0.916	0.905
17	0.22	356.90	106.82	250.08	0.70	0.915	0.899
19	0.25	479.77	170.32	309.45	0.64	0.917	0.895

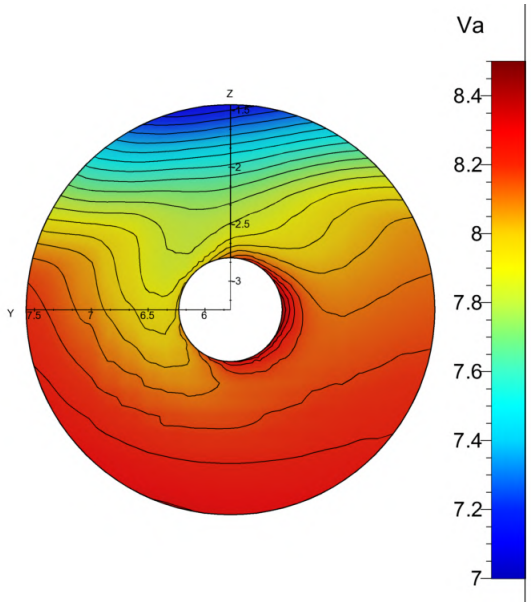

Figure 6.5: Cruise ship reference case: nominal wake field at 17 knots.

With the results of the CFD simulations, a power prediction can be made following the procedure described in section 3.3. The open water diagram of the propeller was not available, therefore it was obtained from the Wageningen B-series. The working point was obtained using the Damen propeller performance tool, which contains all the polynomials of the Wageningen B-series. The corrections made on the resistance for wind and roughness were identical that of the extrapolated model test results. Table 6.4 shows the results of the power prediction for the cruise ship.

Table 6.4: Cruise ship reference case: power speed computation.

v_s [kn]	R_{cor} [kN]	P_s [kW]	η_o [-]	η_h [-]	η_d [-]
9	101.32	672.5	0.697	1.000	0.698
11	153.36	1248.3	0.698	0.996	0.695
14	251.96	2630.1	0.698	0.988	0.690
17	390.64	5009.7	0.694	0.982	0.682
19	524.85	7632.3	0.688	0.976	0.672

6.4 Air cavity system

As already explained in section 6.2 it was observed during the model tests that the aspect ratio of the cavities was lower than expected, see also figure 6.3. Also for this ship, the cavity length is limited by the skeg height rather than by the ship speed. The cavity length cannot be estimated in the same way as was done for the general cargo ship, see section 5.4, due to the lower aspect ratio of the cavities Therefore, the cavity length is approximated based on the observations during the model tests. The last iteration of the cavity system that was tested is modeled with the CFD. During the model tests, it was observed that the cavity length was approximately 80% of the distance between to cavitators for all the three speeds tested. Figure 6.6 shows the schematic layout of the air cavity system on the bottom of the cruise ship. During the design of the system, it was tried to minimize the drag of the skegs by aligning them with the streamlines over the bottom. The streamlines are not completely parallel with the incoming flow due to the slender hull form. The skegs are therefore positioned under a slight angle. As a result, the air cavities have a more trapezoidal shape rather than a rectangular shape.

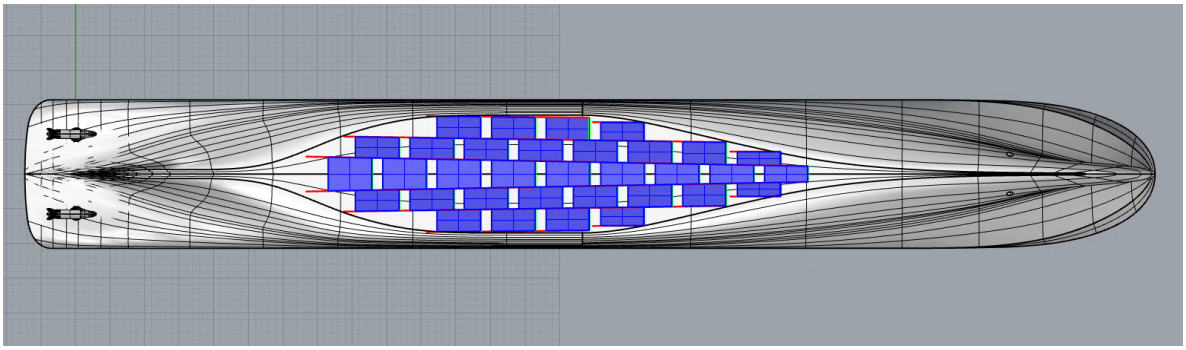

Figure 6.6: Cruise ship: schematic layout of the air cavity system on the bottom. (Blue: air cavities, Red: skegs, Green: cavitators)

6.4.1 System appendages

The DACS system requires appendages to be installed on the bottom of the ship: skegs in the longitudinal direction and cavitators in the transverse direction. Figure 6.7 shows a close-up picture of the appendages of the DACS system on the model of the cruise ship. These appendages cause an increase in drag. Furthermore, it was also observed during the model tests that the relative rotative efficiency η_r is reduced by 1.5% for the case air off when comparing to the reference case. According to the model test report this is probably due to more vorticity in the flow coming from the cavitators and the skegs.

Table 6.5 shows a comparison of the change in (extrapolated) shaft power obtained from the model tests, between the reference and the air off case. The increase in power is 0.2-2.0%. The model test report states however that there is a high uncertainty in these values because they are corrected for fact that the cavitator size is not geometrically similar on model scale an full scale, see also section 6.2. In the CFD simulations, the appendages are not included. This reduces the complexity and computational costs of the simulations. The added resistance of the appendages is estimated to be 2% of the resistance of the reference case, based on the results presented in table 6.5. This increase in resistance is added to the resistance results for the case air on. The correction is made for resistance rather than for power because η_r is kept constant for all results. It should be noted that in reality, with air on, the added resistance due to the appendages is lower. The sides of the skegs are partially covered with air. Next to this, an air cavity is formed behind each cavitator. Figure 6.7 shows the appendages of the DACS system on the model of the cruise ship.

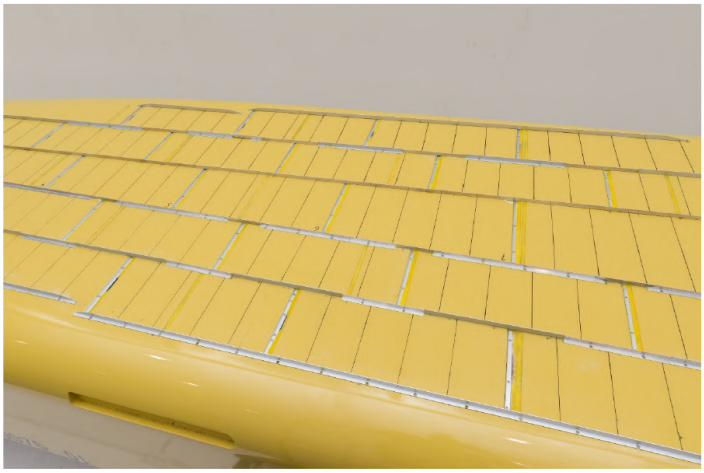

Figure 6.7: Cruise ship: appendages of the DACS system used for the model tests.

Table 6.5: Cruise ship: change in shaft power (extrapolated) measured during model tests after the installation of DACS with air off.

v_s [kN]	ΔP_s [%]
11	2.1
14	2.0
17	0.2

6.5 Comparison

6.5.1 CFD results

First, a comparison is made of the CFD results for the reference case and the case air on. Table 6.7 shows a comparison of the total, pressure and viscous resistance. The table shows that the decrease in viscous resistance is approximately constant within the speed range simulated. Furthermore, only a minor decrease in pressure resistance is observed. This is in contrast with the result of the general cargo ship, see section 5.6. The cruise ship has a much more slender hull form and a lower air-covered area than the cargo ship. As a result, the boundary layer at the stern is affected less by the air cavities. Furthermore, no flow separation is present at the stern for this ship. At 9 knots the decrease in R_p is significantly larger than for the other speeds. The reason for this is unknown, probably it is due to random scatter in the data. The decrease in total resistance decreases with increasing ship speed. The reason for this is that the pressure resistance becomes more dominant. The results are also plotted in figure 6.8.

Table 6.7 shows a comparison between the thrust deduction factor and the nominal wake factor between the reference case and with air on. Again very little change is observed for the thrust deduction

effect. Also, the nominal wake factor is almost identical, the difference is only 0.2%. This is because the propellers are located mostly out of the ship's boundary layer. A change in the boundary layer due to the air cavities will therefore not cause a big change in the wake field. Figure 6.9 shows a comparison for the nominal wake field. Almost no change can be observed.

Table 6.6: Cruise ship: CFD results resistance components comparison between the reference case and air on.

	R [kN]			R_p [kN]			R_v [kN]		
vs [kn]	Ref	Air on	Diff. [%]	Ref	Air on	Diff. [%]	Ref	Air on	Diff. [%]
9	96.12	86.36	-10.16	21.46	20.77	-3.21	74.66	65.58	-12.16
11	143.45	130.02	-9.36	34.42	34.18	-0.69	109.03	95.84	-12.10
14	232.00	210.48	-9.27	59.36	58.99	-0.61	172.64	151.48	-12.25
17	356.90	325.53	-8.79	106.82	106.18	-0.60	250.08	219.35	-12.29
19	479.77	440.88	-8.11	170.32	169.34	-0.57	309.45	271.54	-12.25

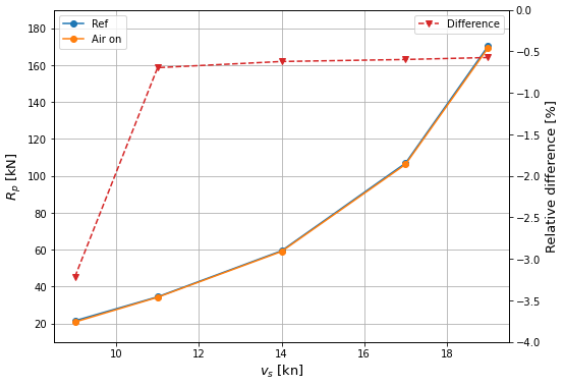

(a) Pressure resistance

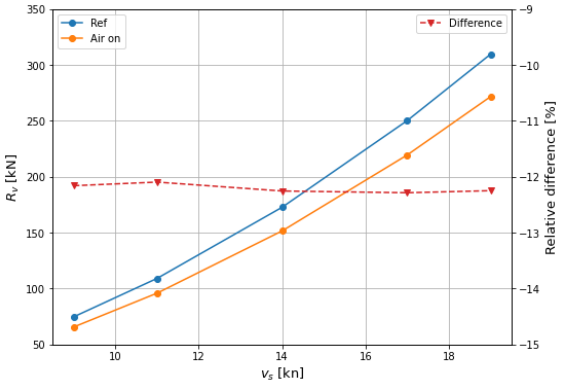

(b) Viscous resistance

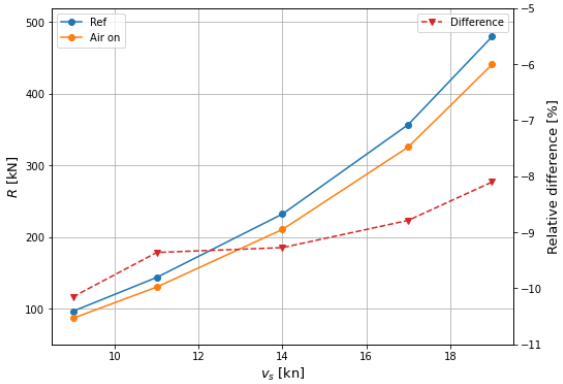

(c) Total resistance

Figure 6.8: Cruise ship: CFD results resistance components comparison, reference, and air on.

Table 6.7: Cruise ship: comparison of the CFD results of the self-propulsion parameters between the reference case and air on.

	$(1-t)$			$(1-w_n)$		
v_s [kn]	Ref	Air on	Diff. [%]	Ref	Air on	Diff. [%]
9	0.914	0.915	0.05	0.914	0.916	0.19
11	0.911	0.912	0.15	0.914	0.916	0.22
14	0.905	0.907	0.18	0.916	0.918	0.16
17	0.899	0.900	0.10	0.915	0.917	0.20
19	0.895	0.896	0.11	0.917	0.919	0.18

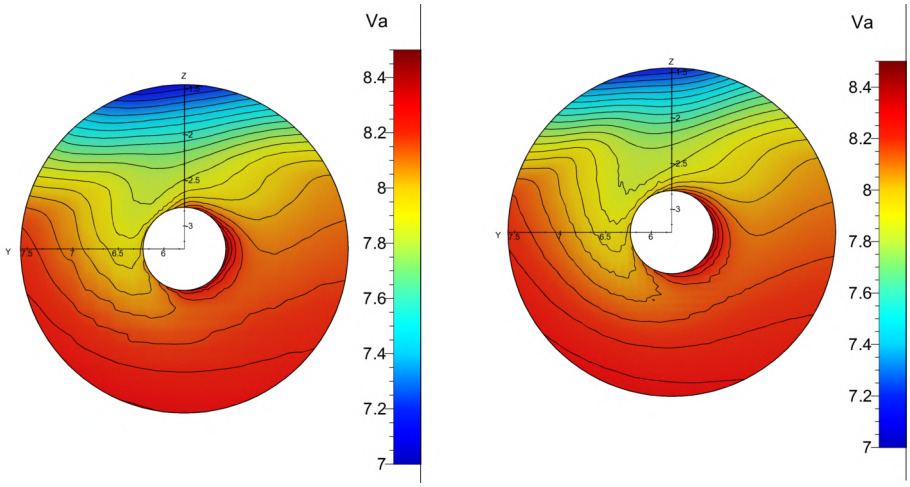

(a) Reference *(b) Air on*

Figure 6.9: Cruise ship: comparison of the nominal wake field at 17 knots.

6.5.2 Power speed comparison

A power speed computation has been made for both the reference case and the case with air on. The corrected resistance R_{cor} includes roughness, wind resistance, and the resistance of the DACS appendages for the case with air on. Tables 6.8 and 6.9 show a comparison for the computed results (R_{cor}, η_o, η_h, η_d, and P_s). It turns out for this ship that the resistance reduction due to the air cavities is very close to the reduction in shaft power. The reduction in shaft power is approximately 1% larger because the propeller open water efficiency η_o is increased by 1 percent. The hull efficiency η_h is almost not affected by the air cavities, because the thrust deduction factor and the wake factor are also almost not changed. η_o is slightly increased due to the change in the propeller working point, see also section 8.1 for a more detailed analysis of the change in propeller efficiency due to air cavities.

Table 6.8: Cruise ship: comparison of the hull efficiency η_h, open water efficiency η_o, and the propulsive efficiency η_d, predicted using CFD, between the reference case and air on.

	η_h [-]			η_o [-]			η_d [-]		
v_s [kn]	Ref	Air on	Diff. [%]	Ref	Air on	Diff. [%]	Ref	Air on	Diff. [%]
9	1.000	0.999	-0.14	0.697	0.704	0.88	0.698	0.703	0.74
11	0.996	0.996	-0.07	0.698	0.704	0.86	0.695	0.701	0.78
14	0.988	0.988	0.01	0.698	0.704	0.88	0.690	0.696	0.90
17	0.982	0.981	-0.10	0.694	0.701	0.94	0.682	0.688	0.84
19	0.976	0.976	-0.07	0.688	0.695	0.94	0.672	0.678	0.87

Table 6.9: Cruise ship: comparison of corrected resistance R_{cor} and shaft power P_s, predicted using CFD, between the reference case and air on.

	R_{cor} [kN]			P_s [kW]		
v_s [kn]	Ref	Air on	Diff. [%]	Ref	Air on	Diff. [%]
9	101.32	93.37	-7.84	672.5	615.8	-8.42
11	153.36	142.29	-7.22	1248.3	1150.9	-7.80
14	251.96	233.60	-7.29	2630.1	2420.9	-7.95
17	390.64	363.49	-6.95	5009.7	4627.7	-7.63
19	524.85	491.42	-6.37	7632.3	7092.1	-7.08

6.6 Comparison with model tests

A comparison is also made between the extrapolated model test results and the CFD results. All presented results are for the ideal trial condition.

6.6.1 Reference case

First of all, a comparison is made between the corrected CFD results and the extrapolated model test results for the Reference case. A comparison is made for Resistance, shaft power, all self-propulsion parameters, and efficiencies. The results are shown in tables 6.10, 6.11, and 6.12. The comparison error is lower than the validation uncertainty for all results, except the resistance at 9 knots. See chapter 4 for an explanation of how the experimental uncertainty, the numerical uncertainty of the parameters computed with CFD, and the uncertainty of the power prediction were computed for the cruise ship.

The tables show that the resistance and as a result also the shaft power is underpredicted by CFD. This is also shown in figure 6.10A possible reason could be that the extrapolated model test results also include a statistical correlation factor. The difference in the wake factor between the CFD results and the model test results is rather low, even though the CFD prediction is made based on the nominal wake factor. This could be because the difference between the nominal and the effective wake field is usually small for twin-screw vessels. The thrust deduction factor and the open water efficiency are also accurately predicted. The difference in relative rotative efficiency η_r is 3-4%, indicating that the assumption that η_r equals 1 is somewhat inaccurate in this case.

Table 6.10: Cruise ship reference case: comparison of corrected resistance R_{cor} and shaft power P_S between CFD and extrapolated model test results (EFD).

	R_{cor} [kN]			P_s [kW]		
v_s [kn]	EFD	CFD	Diff. [%]	EFD	CFD	Diff. [%]
9	111.23	101.25	-8.97	746.0	672.4	-9.86
11	167.17	153.36	-8.26	1356.0	1248.4	-7.94
14	271.03	251.96	-7.04	2804.0	2630.2	-6.20
17	419.65	390.64	-6.91	5295.0	5009.6	-5.39

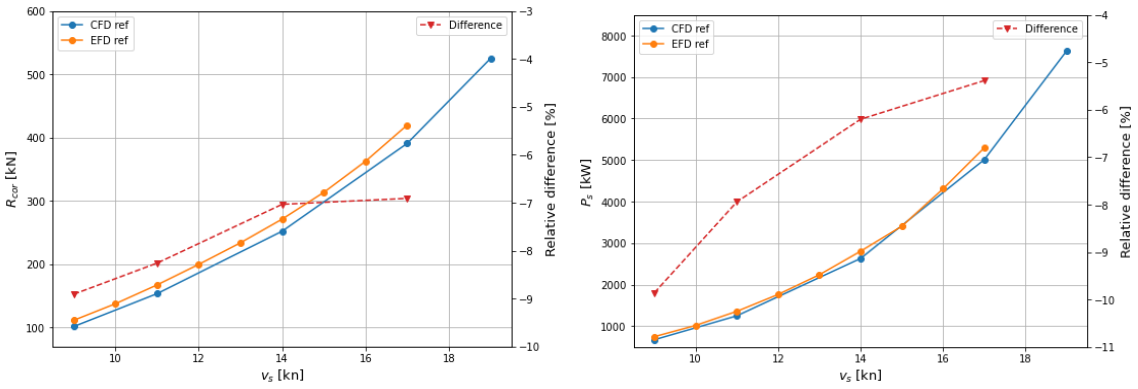

(a) Corrected resistance *(b) Shaft power*

Figure 6.10: Cruise ship reference case: comparison reference case between CFD results and extrapolated model test results (EFD).

Table 6.11: Cruise ship reference case: comparison of thrust deduction factor $(1-t)$, wake factor $(1-w)$ and hull efficiency η_h between CFD and extrapolated model test results (EFD).

	$(1-t)$ [-]			$(1-w)$ [-]			η_h [-]		
v_s [kn]	EFD	CFD	Diff. [%]	EFD	CFD	Diff. [%]	EFD	CFD	Diff. [%]
9	0.895	0.914	2.13	0.935	0.914	-2.27	0.957	1.000	4.50
11	0.903	0.911	0.89	0.932	0.914	-1.90	0.971	0.996	2.63
14	0.898	0.905	0.84	0.930	0.916	-1.47	0.975	0.988	1.35
þ17	0.891	0.899	0.89	0.927	0.915	-1.25	0.978	0.982	0.40

]

Table 6.12: Cruise ship reference case: comparison of relative rotative efficiency η_r, open water efficiency η_o, and propulsive efficiencyη_d between CFD and extrapolated model test results (EFD).

	η_r [-]			η_o [-]			η_d [-]		
v_s [kn]	EFD	CFD	Diff. [%]	EFD	CFD	Diff. [%]	EFD	CFD	Diff. [%]
9	1.041	1.0	-3.94	0.695	0.697	0.34	0.693	0.698	0.73
11	1.038	1.0	-3.66	0.694	0.698	0.53	0.699	0.695	-0.60
14	1.035	1.0	-3.38	0.694	0.698	0.61	0.700	0.690	-1.48
17	1.031	1.0	-3.01	0.690	0.694	0.65	0.696	0.682	-1.99

6.6.2 Comparison for air on

A comparison is also made between corrected CFD results and extrapolated model test results for the case with air on. The change caused by the air cavities (w.r.t. the reference case) is compared for this case. Tables 6.13, 6.14, and 6.15. The results show that the model tests predict a 1-2% larger drag reduction than the CFD results. For the cruise ship, the uncertainty of the predictions with air on is lower than for the cargo ship. There is no change in hull roughness between the different cases. The cavity length is determined based on model test observation as well as the added resistance of the appendages. This means that modeling the air cavities as surfaces with a slip boundary condition results in a reasonably accurate prediction of the drag reduction.

For the model tests it is assumed that the thrust deduction is not changed due to the air cavities so no comparison can be made for it. It seems to be a good approximation based on the CFD results. The model test results predict an increase in the wake factor of 1-2%. This is larger than for the CFD results, but it is still a small change. Both methods also predict only a small increase in open water efficiency. During the model tests a small decrease in η_r was observed due to the DACS appendages, this is already explained 6.2. For the CFD analysis, η_r is assumed to be 1.0 for all cases.

CFD predicts a small increase in propulsive efficiency, whereas the model test results predict a small decrease in propulsive efficiency. The propulsive efficieny η_d is computed from η_r, η_o and η_h. All the differences in the individual efficiencies lead to the difference in the prediction in change of η_d. Still, both methods predict a rather small change in propulsive efficiency in the order of 1-2%.

The CFD results predict a slightly larger shaft power reduction than drag reduction as the model tests, however, the model tests predicted a slightly lower shaft power reduction than drag reduction. This is because CFD predicts a small increase in propulsive efficiency, whereas the model tests predict a small decrease in propulsive efficiency. This is also illustrated in figure 6.11. Still, for both methods, the shaft power reduction is only 1-2% different from the drag reduction. Therefore, for this ship is a good approximation to assume that the drag reduction equals the shaft power reduction.

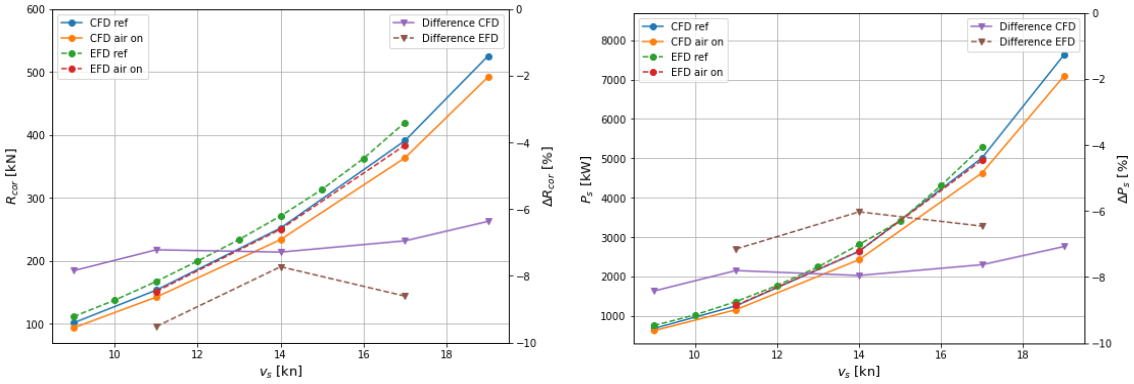

(a) Resistance *(b) Shaft power*

Figure 6.11: Cruise ship: comparison of corrected resistance R_{cor} and shaft power P_s and corrected resistance for the reference case an air on. Results are presented both for extrapolated model test (EFD) and CFD results

Table 6.13: Cruise ship: comparison of the change in resistance R, shaft power P_s, and wake factor $(1-w)$ due to DACS. The comparison is made both for the extrapolated model test results (EFD) and the CFD results.

	ΔR [%]		ΔP_s [%]		$\Delta(1-w)$ [%]	
v_s [kn]	EFD	CFD	EFD	CFD	EFD	CFD
11	-9.52	-7.22	-7.15	-7.80	0.97	0.22
14	-7.73	-7.29	-6.03	-7.95	1.30	0.16
17	-8.61	-6.95	-6.46	-7.63	1.87	0.20

Table 6.14: Cruise ship: comparison of the change in thrust deduction factor $(1-t)$ and relative rotative efficiency η_r due to DACS. The comparison is made both for the extrapolated model test results (EFD) and the CFD results.

	$\Delta(1-t)$ [%]		$\Delta\eta_r$ [%]	
v_s [kn]	EFD	CFD	EFD	CFD
11	0	0.15	-1.73	0
14	0	0.18	-1.06	0
17	0	0.10	-1.07	0

Table 6.15: Cruise ship: comparison of the change in open water efficiency η_o, hull efficiency η_h, and propulsive efficiency η_d due to DACS. The comparison is made both for the extrapolated model test results (EFD) and the CFD results.

	$\Delta\eta_o$ [%]		$\Delta\eta_h$ [%]		$\Delta\eta_d$ [%]	
v_s [kn]	EFD	CFD	EFD	CFD	EFD	CFD
11	0.43	0.86	-0.96	-0.07	-2.26	0.78
14	0.43	0.88	-1.30	0.01	-1.93	0.90
17	0.72	0.94	-1.75	-0.10	-2.10	0.84

6.7 Conclusion

For the cruise ship, it can be concluded that the reduction in power caused by the air cavities is approximately equivalent to the reduction in resistance. However, a small increase in propeller efficiency was observed. The hull efficiency was almost not influenced, because the propellers operate mainly out of the wake of the ship. Furthermore, a good comparison was visible between the CFD results and the extrapolated model test results. This means that the modeling method of the air cavities (slip surfaces) is relatively accurate, provided that the cavity length is known.

Chapter 7
Inland ship

7.1 Description

The last case study is performed on an inland tanker. The ship sails in both inland waterways and coastal areas. Table 7.1 shows the properties of the vessel in the design loading condition. No experimental data of this ship is available so it is a pure case study. However, validation was already performed for the other two ships.

Table 7.1: Inland ship: general properties

Length L_{wl} [m]	119.59
Beam B [m]	17.5
Draft T [m]	3.65
Displacement Δ [ton]	7010.7
Block coefficient C_b [-]	0.919
Design speed [kn]	10.4

The ship's propulsion system consists of two FPP Kaplan propellers, both in a Damen Optima 2000 nozzle. The propellers are each driven by a separate diesel engine. Table 7.2 shows the most important properties of the propellers.

Table 7.2: Inland ship: propeller properties.

Diameter D [m]	2.0
Pitch ratio P/D	1.098
Blade area ratio A_e/A_0	0.8
Number of blades	4
# Propellers k_p	2
Nozzle type	Optima 2000

The vessel has a full hull shape and therefore a high block coefficient. Figure 7.1 shows a bottom view of the bow and stern of the vessel. The figure shows that the ship has 4 rudders, two behind each nozzle.

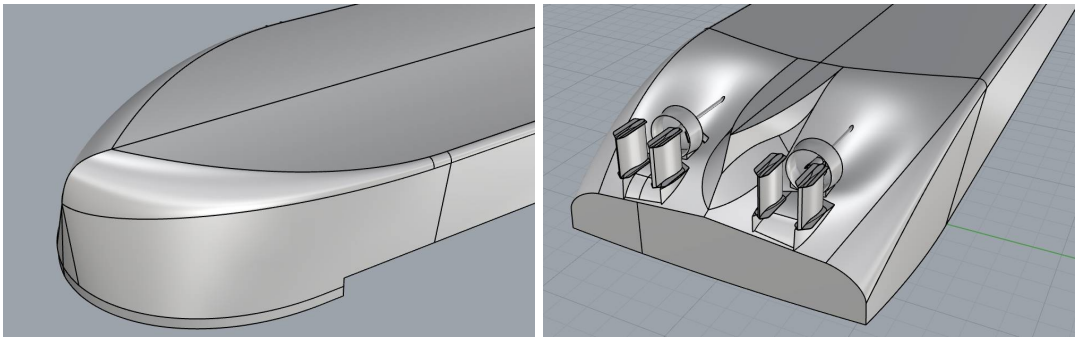

Figure 7.1: Inland ship: bottom view of the bow and stern shape.

7.2 Reference case

First of all, the reference case is modeled (the ship without the DACS system). For simplicity reasons, the top and bottom plates of the rudders were not included in the CFD simulations. This improves the

quality of the mesh and reduces the computational cost. The rudders are located behind the propeller, so they are not expected to affect the flow over the bottom and the propeller wake field. Table 7.3 shows the CFD results for the reference case. The table shows that although the ship is sailing at low speed, a significant portion of the resistance is due to pressure drag.

Table 7.3: Inland ship reference case: CFD results.

v_s [kn]	Fr [-]	R [kN]	R_p [kN]	R_v [kN]	R_v/R [-]	(1-w_n) [-]
7	0.11	56.7	23.5	33.2	0.58	0.893
8	0.12	74.2	31.5	42.7	0.58	0.896
9	0.14	96.0	42.5	53.5	0.56	0.899
10	0.15	128.9	63.6	65.2	0.51	0.901
10.4	0.16	141.9	71.6	70.2	0.50	0.900
11	0.17	174.1	96.1	78.0	0.45	0.902

Figure 7.2 shows the nominal wake field of the ship. The ship has an asymmetric wake field and also a low wake because it is a twin screw ship. The shadow of the shaft support struts is clearly visible in the wake field.

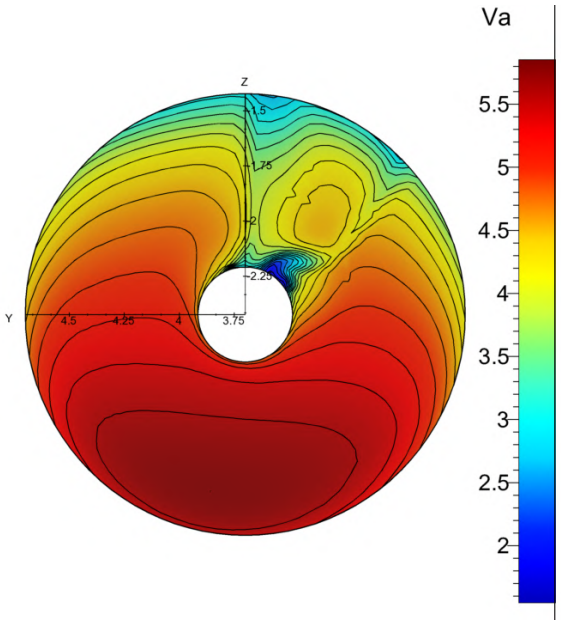

Figure 7.2: Inland ship reference case: nominal wake field at 10.4 knots.

7.2.1 Flow separation

The relatively high pressure resistance of the ship is caused by flow separation. Figure 7.3 shows a plot of the instantaneous flow separation at the stern. The figure shows that there is a little bit of separation present at the trailing edges of the rudders and nozzle. However, a large amount of separation is present behind the rudder headboxes. Lastly, there is also a large flow separation region behind the transom. This is because the transom of the ship is partially submerged. Typically a recirculation region is present behind a (partially submerged) transom, because of the sudden jump in the flow. This type of flow is similar to the flow through a backward-facing step. (K. B. Korkmaz et al., 2022).

No grid convergence study was performed for this ship because this was already done for the general cargo ship. K. B. Korkmaz et al. (2022) did an extensive CFD study on the flow around a container ship with a partially submerged transom. They found a rather large numerical uncertainty for the pressure resistance in the order of 15%. Also, large differences in numerical uncertainty were found between model scale and full scale, and between different turbulence models. The numerical uncertainty for the viscous resistance was significantly lower, between 1% and 2%.

Moreover, it is uncertain whether the CFD flow models used can accurately capture the extensive separated flow at the ship's stern. A quasi-static approach was used for the CFD simulations. The turbulence was modeled using an eddy viscosity 2-equation model (k-w SST), and the boundary layer was resolved using wall functions, see also section 3.4. Typically, eddy viscosity turbulence models are not capable of accurately modeling separated flows over 3D geometries, (Spalart, 2000). Furthermore, wall functions are also invalid in regions of separated flow, (Eça & Hoekstra, 2011). Lastly, flow separation is an unsteady process, e.g. due to periodic shedding of vortices. This unsteady process cannot be modeled with a quasi-static simulation. This would require e.g. URANS (unsteady RANS) or scale-resolving simulations. (Spalart, 2000), (Iaccarino et al., 2003), and (Shevchuk et al., 2016). For the inland ship, it was observed that the standard deviation of the pressure force was less than 1% despite the unsteady nature of the flow separation. Based on the above discussion, it can be concluded that the computed pressure resistance for this ship is likely to be highly uncertain, primarily due to modeling errors and numerical inaccuracies. A more detailed investigation into the accuracy of the flow separation and pressure resistance modeling is out of the scope of this work. For this research, the viscous resistance and the wake field of the ship are of main interest.

The mass fraction at the stern of the ship is shown in figure 7.3. At and also below the transom, near the headboxes, a mass fraction between 0 and 1 is observed. This shows that the ship suffers from ventilation. It is probably due to the low pressure in the separated flow region. It is doubtful whether the ventilation on the stern is simulated correctly using the VoF model, which is an interface model, (Gray-Stephens et al., 2021). In addition, the ventilation is a direct consequence of the flow separation at the stern, which is also subject to considerable uncertainty as explained above. The ventilation at the stern affects the viscous resistance because it reduces the wetted area. It is not expected however that this will have a large impact. The area on the ship hull with a mass fraction lower than 1 is rather small compared to the total wetted area.

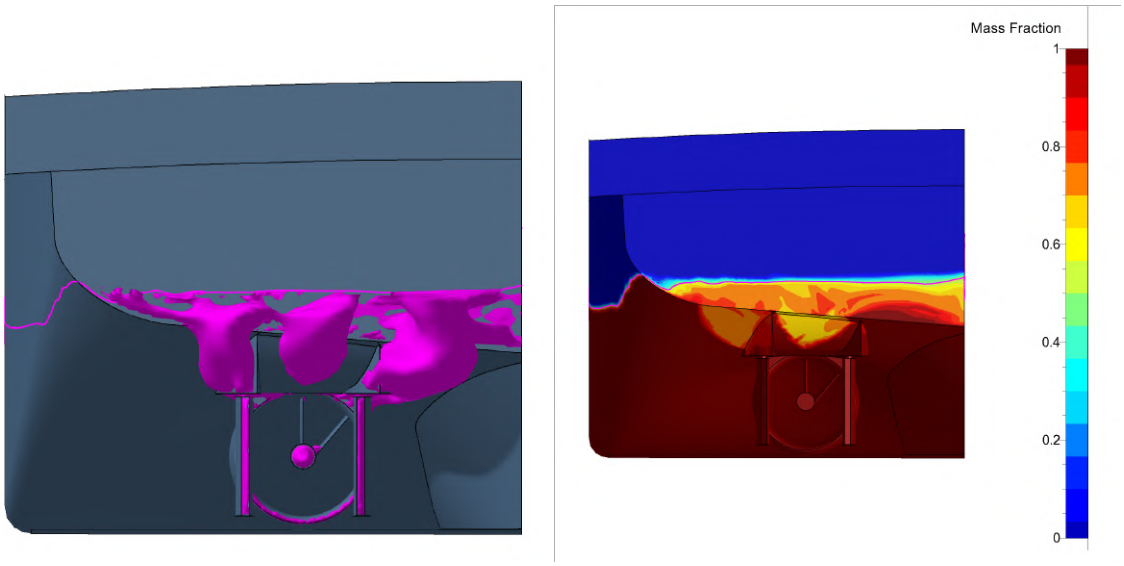

Figure 7.3: Inland ship reference case: plots of the instantaneous flow separation and the mass fraction at the stern at 10.4 knots.

Possibly, the flow separation at the stern is also influenced by the action of a propeller. Therefore also one simulation is performed including the actuator disk model to investigate the propeller effect on the flow separation at the stern. Figure 7.4 shows a comparison of instantaneous flow separation at the stern with and without the actuator disk. The figure shows that flow separation at the transom is not affected. The separation at the rudder headboxes is still present but reduced with the actuator disk on. Generally speaking, no significant reduction of the flow separation at the stern is observed with the actuator disk on. This is also expected because all area's of separated flow are located behind the propeller. The ventilation at the transom also remains present with the actuator disk on. It should be noted that the figure only shows an instantaneous, but that flow separation is an unsteady process. Therefore the comparison is only indicative.

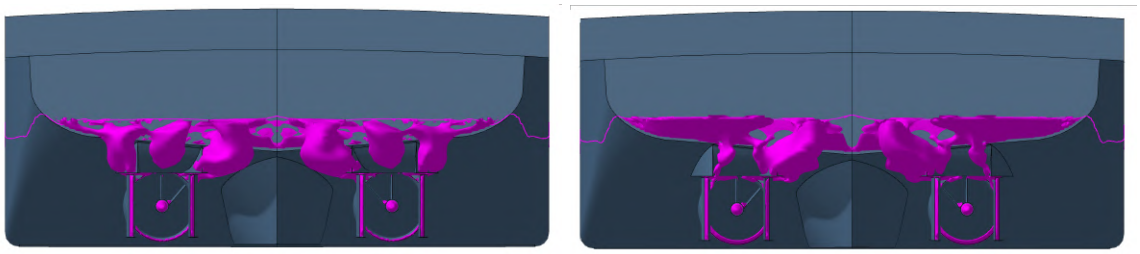

(a) Without actuator disk *(b) With actuator disk*

Figure 7.4: Inland ship reference case: comparison of instantaneous flow separation at the stern at 10.4 knots with and without actuator disk

7.2.2 Power prediction

A power speed prediction was also performed for the inland ship before the installation of the air cavity system. The computation is made using the approach described in section 3.3. The propeller working point was obtained using the Damen propeller performance tool which contains the propeller polynomials of the Kaplan propeller corrected for the Optima nozzle. The computation was made using the nominal wake fraction, similar to the other ships. It was observed from the two previous ships that the thrust deduction effect is barely influenced by the air cavities. Therefore it seemed unnecessary to also perform a detailed investigation including the actuator disk model for this ship. Only one simulation in deep and in shallow water was performed to investigate the effect of the propeller action on the flow separation. For the power speed calculation a thrust deduction fraction of 0.1 was assumed which is a typical value for twin-screw ships, see also section 2.3.2. The results are shown in table 7.4. For this ship, the power speed prediction gives an indication of the required power of the ship. No comparison is made with experimental data because this is already done for the other two ships. The same calculation procedure is used both with air on and for the reference case so the results can be used for comparison.

Table 7.4: Inland ship reference case: power speed computation.

v_s [kn]	R [kN]	P_s[kW]	η_o [-]	η_h [-]	η_d [-]
7	56.7	352.5	0.574	1.008	0.579
8	74.2	528.9	0.574	1.005	0.577
9	96.0	773.0	0.574	1.001	0.575
10	128.9	1162.5	0.571	0.999	0.570
10.4	141.9	1332.7	0.570	1.000	0.570
11	174.1	1746.4	0.565	0.998	0.564

7.3 Air cavity system

In practice, this inland vessel does not have the Damen Air Cavity System installed. Therefore a conceptual layout of the air cavities on the bottom of the ship was made according to Damen's best design practice. The design of the system for this ship is different compared to the general cargo ship and the cruise ship. The reason for this is that an inland ship often sails in shallow water. The cargo capacity (and the ship's) draft is often limited by the water depth. Therefore, the height of the skegs under the bottom is lower than for normal ships.

As explained earlier, see section 2.1.4, the cavity length is limited either by the skeg height or by the ship speed. In this case, with a lower skeg height, the cavity length is already at the lowest simulated speed (7 knots) limited by the skeg height. In this case, the cavity length is 80% of the distance between the cavitators to prevent interaction between the cavities, in case the cavity length is longer than predicted. Figure 7.5 shows a schematic drawing of the cavity layout on the bottom of the inland ship.

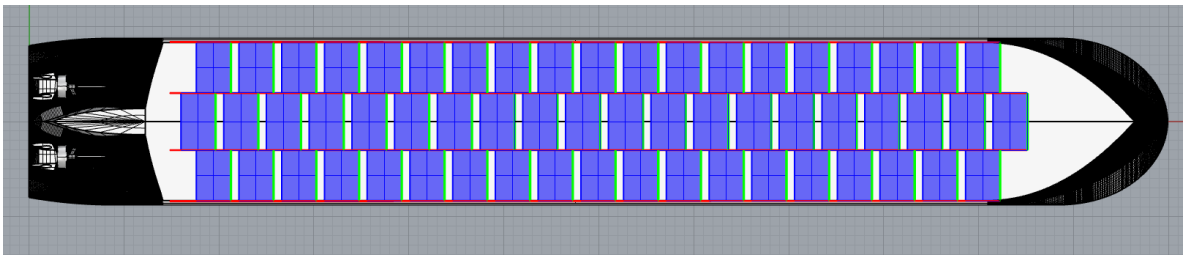

Figure 7.5: Inland ship: schematic layout of the air cavity system on the bottom. (Blue: air cavities, Red: skegs, Green: cavitators)

7.4 Comparison

A comparison is made between the CFD results of the reference case and with air on. The comparison for the resistance is shown in table 7.5 and also in figure 7.6. A stable 30% reduction in viscous resistance is observed for all cases.

Table 7.5: Inland ship: CFD results resistance components comparison between the reference case and air on.

	R [kN]			R_p [kN]			R_v [kN]		
v_s [kn]	Ref	Air on	Diff. [%]	Ref	Air on	Diff. [%]	Ref	Air on	Diff. [%]
7	56.68	48.07	-15.19	23.52	24.87	5.73	33.15	23.20	-30.03
8	74.18	63.29	-14.68	31.49	33.43	6.17	42.69	29.86	-30.07
9	95.96	83.31	-13.18	42.51	45.86	7.87	53.45	37.45	-29.93
10	128.85	108.09	-16.11	63.62	62.22	-2.20	65.23	45.87	-29.69
10.4	141.87	125.36	-11.64	71.63	76.19	6.36	70.24	49.17	-30.00
11	174.08	149.08	-14.36	96.09	94.38	-1.78	77.99	54.71	-29.85

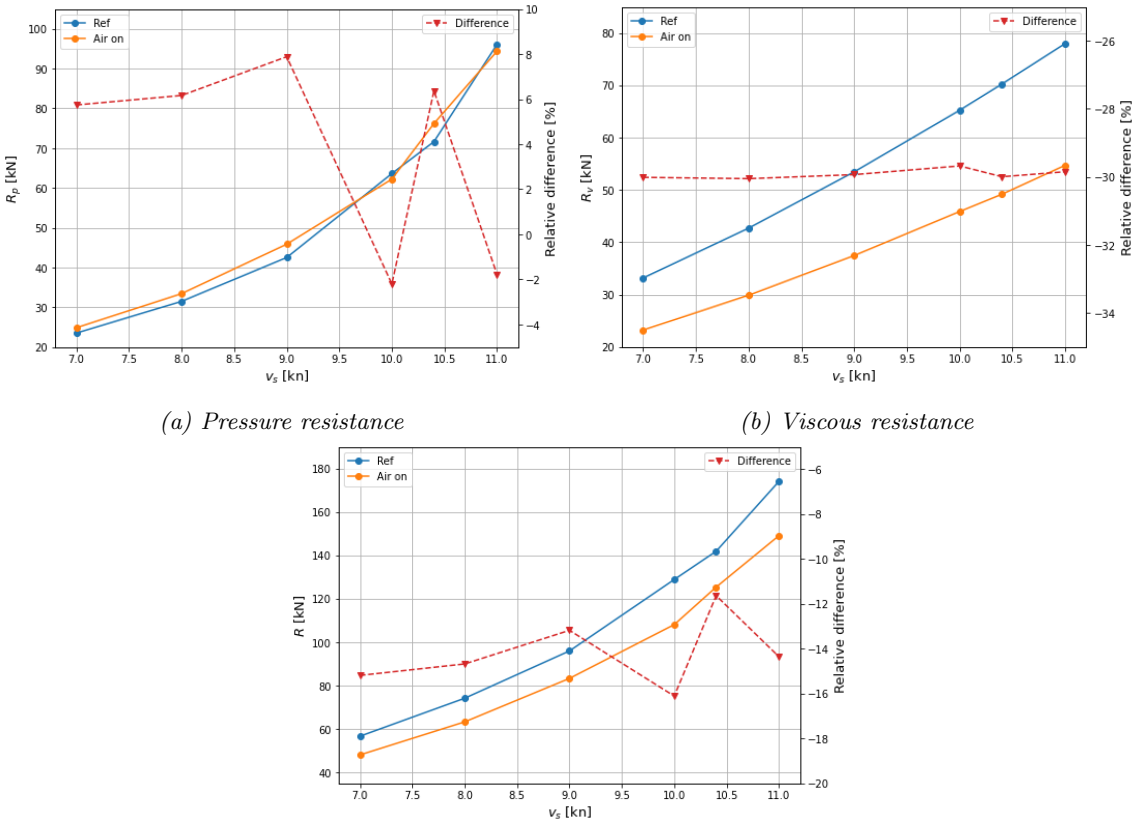

(a) Pressure resistance

(b) Viscous resistance

(c) Total resistance

Figure 7.6: Inland ship: CFD results resistance components comparison, reference, and air on.

The results show that the pressure resistance is also changed when comparing the reference case with air on. However, no clear trend can be observed. At two speeds there is a small reduction of 1-2%. In contrast, pressure resistance is increased by 5-7% at the other speeds. It should be noted that no significant differences in iterative convergence were observed between the different simulations. The standard deviation of the pressure resistance was lower than 1% in all cases The wave profile is identical for both cases so the wavemaking resistance is not affected by the air cavities as expected. Therefore the change is pressure resistance is caused by a change of the viscous pressure resistance. Figures 7.7 and 7.8 show a comparison of the flow separation and the mass fraction at the stern of the ship. Both figures are only indicative of the differences between the two cases, as they are instantaneous snapshots. Flow separation is an unsteady process, see also in section 7.2.1, so no firm conclusions on the change in flow separation can be made by only comparing instantaneous flow separation which is computed from a quasi-static simulation. In this case figure 7.7 only shows a minor difference in instantaneous flow separation.

Those observations are different from those of the general cargo ship, see section 5.6. For that ship, a clear trend was observed: a decrease in pressure resistance, because the cavities reduce the separation at the gondola. However, the flow separation at the gondola is clearly affected by the boundary layer development over the bottom of the hull. For the flow separation at the transom, this is less evident. For the inland ship, it is therefore questionable whether the pressure resistance is affected due to the air cavities. It could also be caused by the numerical and modeling uncertainty of the used CFD method. Further research into how flow separation and ventilation at the transom could be affected by air cavities is recommended.

The ventilation also causes a slight change in the wetted area at the stern, which in turn affects the frictional drag prediction, see figure 7.8. The change in ventilation behavior between the reference case and air on is rather small compared to the total wetted area of the ship. Therefore it is not expected that this will change the accuracy of prediction of the frictional drag reduction.

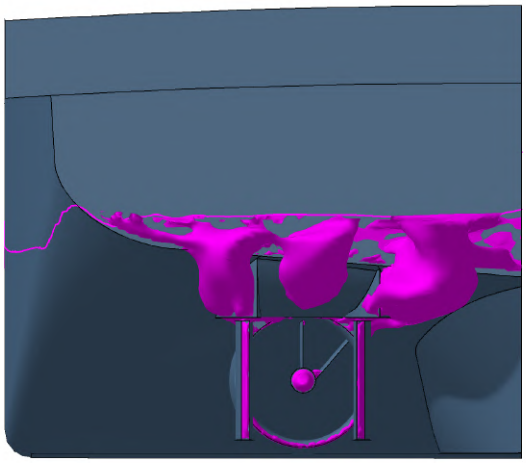

(a) Reference, back view

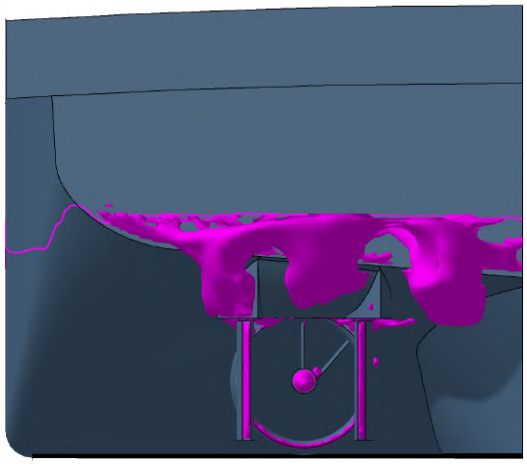

(b) Air on. back view

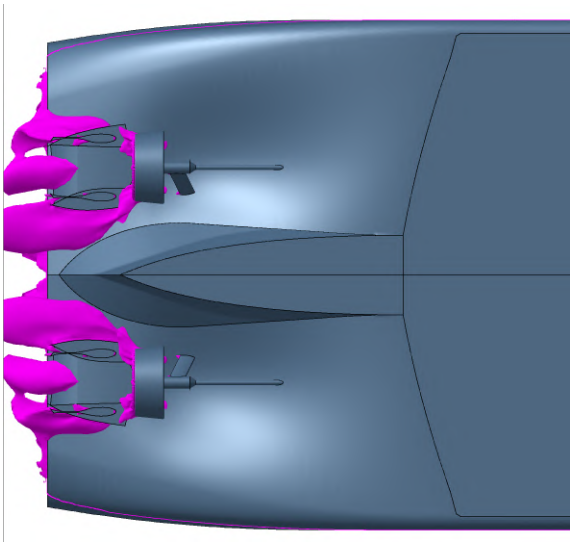

(c) Reference, bottom view

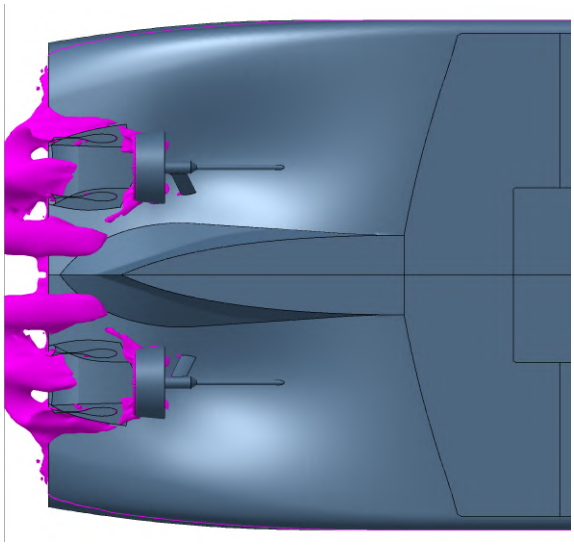

(d) Air on. bottom view

Figure 7.7: Inland ship: comparison of instantaneous flow separation at the stern at 10.4 knots.

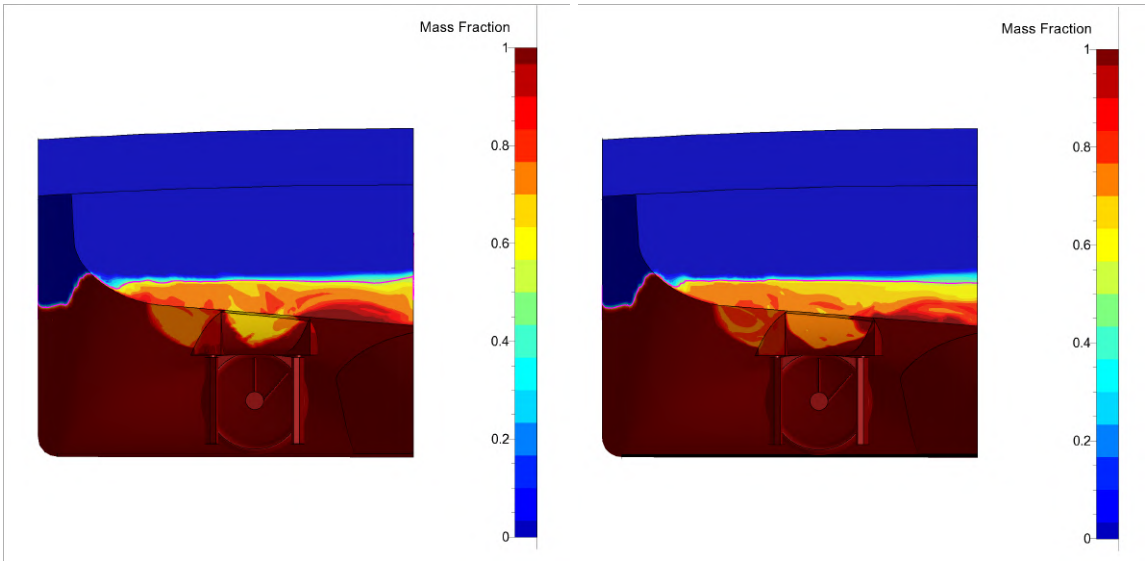

(a) Reference *(b) Air on*

Figure 7.8: Inland ship: comparison of the mass fraction at the stern at 10.4 knots.

Table 7.6 shows a comparison for the nominal wake factor. Figure 7.9 shows a comparison for the nominal wake field. Again it is observed that the profile of the wake field is not affected. However, the wake is reduced by 5-6% due to the air cavities. This is still a considerable reduction, despite the ship having a twin-screw propulsion configuration. With air on the axial velocity in the upper part of the wake field is increased. It is also a different observation compared to the cruise ship, which is also a twin-screw vessel, see section 6.5. For that ship, only a very little change in the wake field was observed. The different observations for those two ships are due to the location of the propellers. The cruise ship has an even lower wake field. Furthermore, it also has podded propulsion, whereas the inland ship has an open shaft line configuration. The propellers of the cruise ship are located further away from the boundary layer of the hull.

Table 7.6: Inland ship: comparison of the nominal wake factor between the reference case and air on.

	$(1 - w_n)$		
v_s [kn]	Ref	Air on	Diff. [%]
7	0.893	0.944	5.76
8	0.896	0.950	6.01
9	0.899	0.949	5.60
10	0.901	0.952	5.65
10.4	0.900	0.950	5.49
11	0.902	0.956	6.03

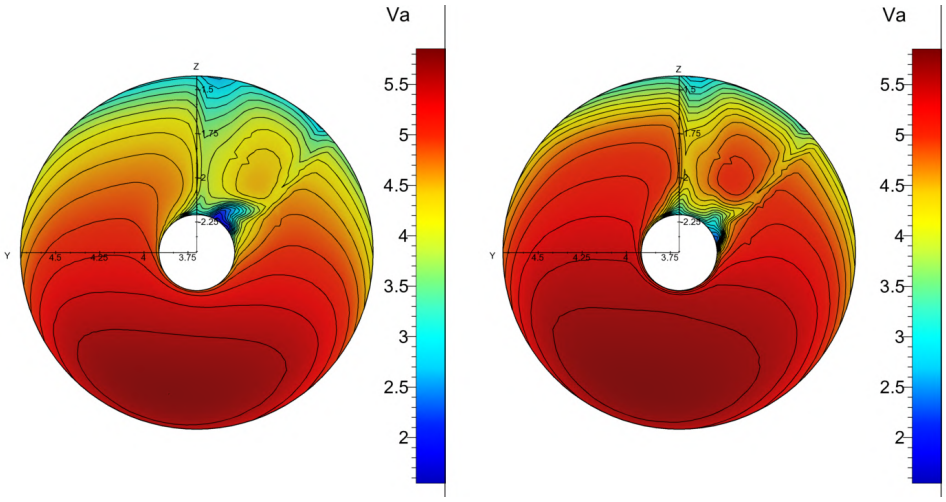

(a) Reference *(b) Air on*

Figure 7.9: Inland ship: comparison of the nominal wake field at 10.4 knots.

7.4.1 Power speed comparison

A power speed computation has been made for both the reference case and the case with air on. The added resistance of the appendages is assumed to be 3% of the resistance. This is a conservative approximation and it is based on the results of the general cargo ship and the cruise ship. Tables 7.7 and 7.8 show a comparison of the computed results (R_{cor}, η_o, η_h, η_d, and P_s). A reduction in hull efficiency of approximately 5% is present due to the drop in hull efficiency. In contrast, the propeller efficiency is increased by 1-2% due to the change of the propeller working point. Consequently, the total propulsive efficiency is reduced by approximately 4% due to the air cavities. As a result, the power reduction is lower than the resistance reduction. This observation is similar to that of the cargo ship, see also section 5.6.

Table 7.7: Inland ship: comparison of the hull efficiency η_h, open water efficiency η_o, and the propulsive efficiency η_d, predicted using CFD, between the reference case and air on.

	η_h [-]			η_o [-]			η_d [-]		
v_s [kn]	Ref	Air on	Diff. [%]	Ref	Air on	Diff. [%]	Ref	Air on	Diff. [%]
7	1.008	0.953	-5.45	0.574	0.580	0.97	0.579	0.553	-4.53
8	1.005	0.948	-5.67	0.574	0.580	0.94	0.577	0.550	-4.78
9	1.001	0.948	-5.31	0.574	0.579	0.96	0.575	0.550	-4.39
10	0.999	0.946	-5.35	0.571	0.579	1.42	0.570	0.548	-4.01
10.4	1.000	0.948	-5.21	0.570	0.577	1.28	0.570	0.548	-3.99
11	0.998	0.941	-5.69	0.565	0.576	1.85	0.564	0.543	-3.95

Table 7.8: Cargo ship: comparison of corrected resistance R_{cor} and shaft power P_s, predicted using CFD, between the reference case and air on.

	R_{cor} [kN]			P_s [kW]		
v_s [kn]	Ref	Air on	Diff. [%]	Ref	Air on	Diff. [%]
7	56.7	49.8	-12.19	352.5	324.2	-8.02
8	74.2	65.5	-11.68	528.9	490.6	-7.25
9	96.0	86.2	-10.18	773.0	726.2	-6.05
10	128.9	112.0	-13.11	1162.5	1052.2	-9.49
10.4	141.9	129.6	-8.64	1332.7	1268.2	-4.84
11	174.1	154.3	-11.36	1746.4	1611.7	-7.72

7.5 Shallow water

The flow around the inland ship is also studied in shallow water with and without air lubrication. Inland ships often sail in shallow water; a better understanding of the air lubrication performance in shallow water is required. In chapter 2.4 it was already explained that shallow water effects have to be considered when at least one of the following two indicators has been reached, shallow water effects have to be considered, (ITTC, 2021):

- Depth-based Froude number $Fr_h = \frac{V}{\sqrt{g \cdot h}} > 0.5$
- Water-depth to ship-draft ratio $H/T < 4.0$

where V is ship's speed, g the gravitational acceleration, h the water depth, and T the ship's draft. First of all, it should be decided which water depths will be investigated. Rotteveel (2019) performed an extensive study into the optimization of the stern shape of inland waterway vessels. He states that the water depths that are frequently encountered along the main inland waterway transport route from Rotterdam to Germany (the Waal and Rhine rivers) correspond to a water depth to ship draft ratio h/T between 2.0 and 3.0. Another frequently used canal is the Amsterdam-Rhine canal that connects Amsterdam to the Waal. The guaranteed water depth in the Amsterdam-Rhine canal is 6.0 meters, whereas the maximum allowed draft is 4.0 meters. This corresponds to a h/T ratio of 1.5. Therefore those three h/T ratios will be investigated. Furthermore, one very shallow case is also considered: $h/T = 1.35$, because inland ships could also encounter very shallow water depths, e.g. in shallow parts of the river or during periods of drought. The four water depths are studied at three speeds: 8, 9 and 10 knots to increase the amount of data points. No speeds are modeled larger than 10 knots because the design speed of the ship is 10.4 knots. In shallow water the resistance of a ship increases, meaning that the ship will probably not be able to reach a speed of 10.4 knots in practice. Table 7.9 gives an overview of the different water depths investigated and of the predicted sinkage in each case. The sinkage prediction is described in the next section.

7.5.1 Description

Table 7.9: Water depth H, under keel clearance (UKC), and predicted sinkage for the H/T ratios that are studied.

			Predicted sinkage [m]		
H/T [-]	H [m]	UKC [m]	8 [kn]	9 [kn]	10 [kn]
3.0	10.95	7.30	0.12	0.15	0.19
2.0	7.30	3.65	0.18	0.24	0.32
1.5	5.48	1.83	0.26	0.35	0.47
1.35	4.93	1.28	0.30	0.40	0.55

7.5.2 Numerical setup

The numerical setup for the shallow water simulations is explained in detail in section 3.4.7. For each water depth and speed the ship is meshed at its expected location of sinkage. This is done to prevent excessive grid deformation due to the squat effect. The expected sinkage is predicted using the method of Tuck (1966). This method provides a relation for the sinkage of the ship as a function of the depth-based Froude number and geometry parameters of the ship. Based on this method, Vermeer (1977) found a practical relation for the sinkage i:

$$\frac{i}{L} = c_i \cdot \frac{\nabla}{L^3} \cdot \frac{Fr_h^2}{\sqrt{1 - Fr_h^2}} \tag{7.1}$$

$$c_i = \frac{1}{6\pi c_w c_p} \cdot (32 - 40c_w - 40c_p + 75c_w c_p - 980 i_w i_p c_w c_p) \tag{7.2}$$

with prismatic coefficient c_p, waterplane coefficient c_w, longitudinal center of buoyancy i_p, and longitudinal center of flotation of the waterline i_w. i_w and i_p have been non-dimensionalized with respect

to L and are measured sternward from $L/2$. According to Vermeer (1977), the last term of c_i can be neglected for calculation purposes. The expected trim of the ship can also be predicted with the method of Tuck (1966). However, the ship is not meshed at the expected location of trim. because it is expected that the trim due to the squat effect will be low because the ship has a very high block coefficient and a long parallel midship.

Unfortunately, problems occurred for multiple CFD simulations despite the modification in the simulation settings according to the guidelines of Numeca and Damen RD&I. Multiple simulations crashed because of negative volumes occurring in the domain due to the mesh deformation. Several attempts were made to solve this issue. $y+$ was increased on the bottom to reduce the impact of the mesh deformation on the bottom cells. However, the problems could not be solved with this modification. Furthermore, the simulations that crashed were also run without trim and sinkage of the ship. However, in that case, the simulations all diverged due to an explosion of the turbulent kinetic energy. The reason for this could not be explained. Probably excessive grid deformation is not the only cause of the crashes of the simulations with free trim and sinkage.

Because of this, no results could be obtained at $H/T = 2.0$ for both air on and air off and at $H/T = 1.5$ for air on. At the other water depths, almost all simulations run successfully, besides a few exceptions. Surprisingly, no crashes were obtained at the most shallow water depth ($H/T = 1.35$) whereas in less shallow cases crashes were reported. At the deepest and the most shallow ($H/T = 3$ and $H/T = 1.35$) case still, a comparison can be made between the results of the reference case and that with air on. Therefore, the research question of this research can still be answered.

It is not expected that the issues occurring at the other water depths can be easily resolved. Probably the guidelines from Damen RD&I should be revisited first to prevent future crashes of CFD simulations in shallow water. This is out of the scope of this thesis and should be a subject for further research.

7.5.3 Comparison reference case

First of all, a comparison is made of the ship without air between the different water depths. Table 7.10, 7.11, 7.12 show a comparison between the viscous resistance, the pressure resistance, and the total resistance at 8, 9, and 10 knots for all available data points. The relative increase of the different resistance components between different water depths is also plotted in figure 7.10.

Regarding the viscous resistance, a low increase of 3-5% is visible at $H/T = 3$. This difference increases to 20-30% at $H/T = 1.35$. This can be explained by the fact that the flow speed under the bottom is increased in shallow water, resulting in an increase in friction. For the pressure resistance shows a slight increase at $H/T = 3$. However, in more shallow water a significant increase in the pressure resistance is observed. The pressure resistance is partially increased due to an increase in the wavemaking resistance. It is observed that the amplitude of the ship waves is increased. However, the maximum depth-based Froude number modeled is 0.74. At this Froude number the wavemaking resistance and wave pattern are not yet significantly affected by the shallow water effect, (Larsson & Raven, 2010). Therefore the increase in pressure resistance is mainly due to the increase of the viscous pressure resistance.

Table 7.10: Inland ship reference case: comparison of the resistance components for different water depths at 8 knots.

	Resistance		Pressure resistance		Viscous resistance		
H/T [-]	Value [kN]	Diff. [%]	Value [kN]	Diff. [%]	Value [kN]	Diff. [%]	R_v/R [-]
Deep	74.2	-	31.5	-	42.7	-	0.58
3	79.9	7.7	34.6	9.8	45.3	6.1	0.57
1.35	120.3	62.1	68.7	118.3	51.5	20.7	0.43

Table 7.11: Inland ship reference case: comparison of the resistance components for different water depths at 9 knots.

	Resistance		Pressure resistance		Viscous resistance		
H/T [-]	Value [kN]	Diff. [%]	Value [kN]	Diff. [%]	Value [kN]	Diff. [%]	R_v/R [-]
Deep	96.0	-	42.5	-	53.4	-	0.56
3	104.6	9.0	47.7	12.3	56.9	6.4	0.54
1.5	141.6	47.6	76.8	80.7	64.8	21.2	0.46
1.35	196.4	104.7	130.5	207.1	65.8	23.2	0.34

Table 7.12: Inland ship reference case: comparison of the resistance components for different water depths at 10 knots.

	Resistance		Pressure resistance		Viscous resistance		
	Value [kN]	Diff. [%]	Value [kN]	Diff. [%]	Value [kN]	Diff. [%]	R_v/R [-]
Deep	128.9	-	63.6	-	65.2	-	0.51
3	135.6	5.2	66.0	3.8	69.5	6.6	0.51
1.5	251.6	95.3	170.6	168.1	81.0	24.2	0.32
1.35	369.7	186.9	284.1	346.6	85.6	31.2	0.23

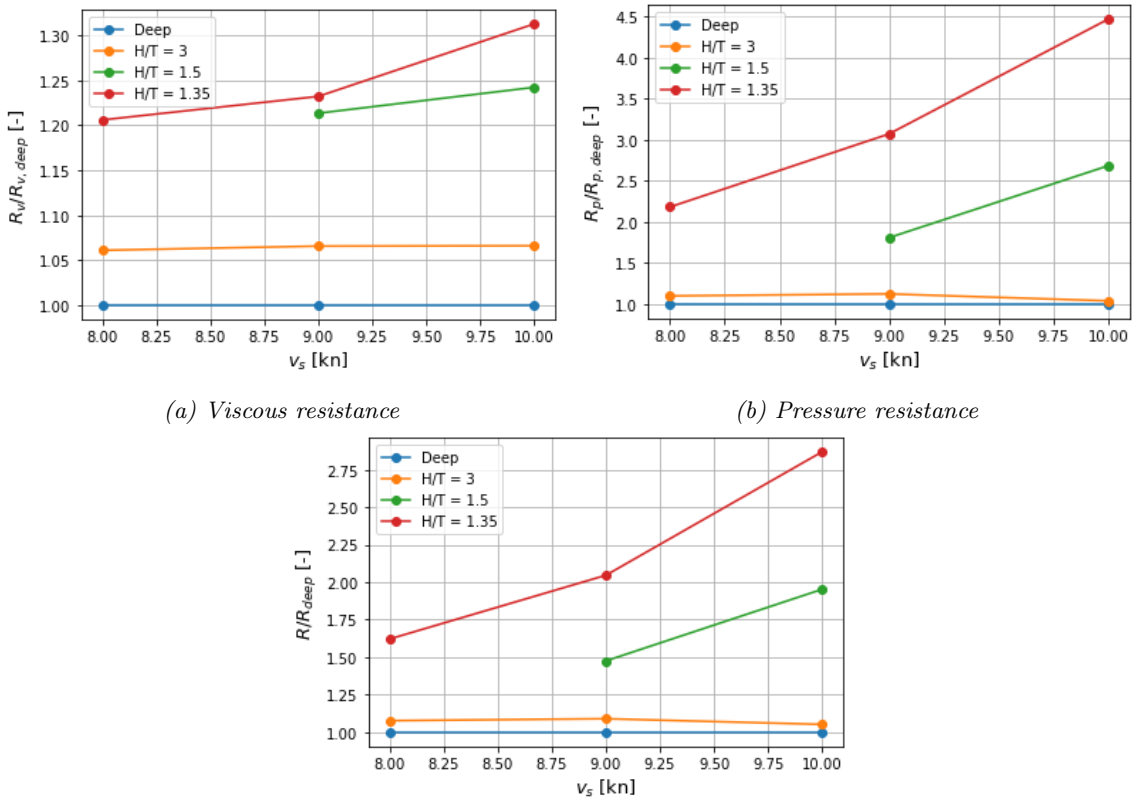

(a) Viscous resistance

(b) Pressure resistance

(c) Total resistance

Figure 7.10: Inland ship reference case: comparison of relative increase for the different resistance components between different water depths

In figure 7.11 the instantaneous flow separation at the stern is shown for different water depths at 9 knots. The figure shows that the amount of separation is increased significantly in shallow water. In very shallow water ($H/T = 1.35$ and 1.5) a lot of flow separation is present behind the skeg and also behind the shaft lines. This can be explained from theory. The effect of water depth on the viscous flow is an increased flow velocity along the hull and larger pressure gradients. If the flow gets more

shallow the flow is forced to pass along the sides of the hull rather than under the bottom. As a result, the flow will follow a more horizontal path. Usually this results in more streamline curvature and larger pressure gradients. The frictional resistance is larger due to the increased flow velocity. The viscous pressure resistance increases due to the changed pressure distribution. This is expressed by a larger form factor. Furthermore, due to the larger pressure gradients, the ship's boundary layer thickness increases which can lead to (increased) flow separation at the stern. (Zeng, 2019) and (Raven, 2022) A more detailed explanation of the flow around a ship in shallow water is described in section 2.4.

It was already explained earlier that no firm conclusions on the change in flow separation can be made by only comparing instantaneous flow separation which is computed from a quasi-static simulation because flow separation is a highly unsteady process. However, in this case, figure 7.11 shows large differences in flow separation between the most shallow and the deep water case. Therefore it can still be concluded that the pressure resistance and flow separation are increased significantly in shallow water, due to the large differences in instantaneous flow separation and because an increase in flow separation in shallow water can also be explained from theory.

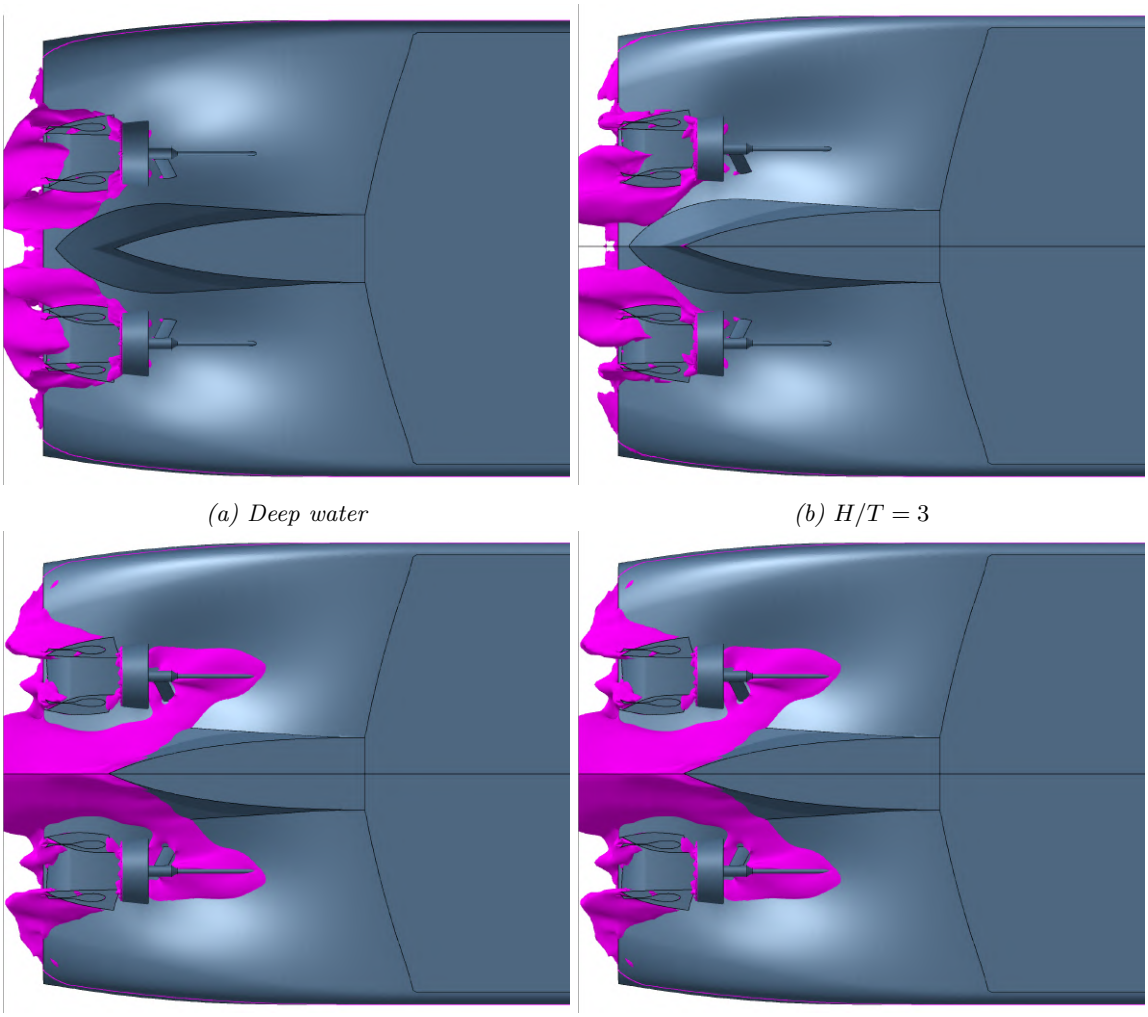

(a) Deep water *(b) $H/T = 3$*

(c) $H/T = 1.5$ *(d) $H/T = 1.35$*

Figure 7.11: Inland ship reference case: comparison of instantaneous flow separation at the stern for different water depths at 9 knots.

Table 7.13 shows the trim, sinkage, for all water depths and deep water. The sinkage of the ship increases significantly in shallow water, also in the not-so-shallow case of $H/T = 3$. This is due to the squat effect, see section 2.4 for a more detailed explanation on the squat effect. The trim of the ship also increases in shallow water due to the squat effect. It turned out that the sinkage could be predicted reasonably accurately using the method of Tuck (1966), which was used for an initial prediction of the sinkage to reduce grid deformation. Usually, this method predicted the sinkage within a 5-10%

difference of the CFD result. The difference increased for a higher depth-based Froude number.

Table 7.13 also shows the nominal wake fractions for different water depths. A comparison of the instantaneous nominal wake field for different water depths is present in figure 7.12. The table also shows that the nominal wake factor $(1 - w_n)$ changes significantly in shallow water. A small increase is observed at $H/T = 3$ probably due to an increase of the boundary layer thickness. The structure of the wake field at this water depth is still very similar compared to deep water. In more shallow water, however, the structure of the wake field changes completely. A lot of flow separation is present in the top part of the wake field at the lowest water depth $H/T = 1.35$. This can also be seen from figure 7.11 At $H/T = 1.5$, the axial part in the upper part of the wake is already very close to zero. It should be noted that the presented nominal wake fields are instantaneous. Flow separation is an unsteady process. Therefore the nominal wake field for the water depths $H/T = 1.35$ and $H/T = 1.5$ will also be time-varying. The comparison of the nominal wake factor in table 7.13 is therefore only indicative.

Table 7.13: Inland ship reference case: sinkage, trim, and nominal wake factor for different water depths.

	Sinkage [m]			Trim [deg]			$(1 - w_n)$ [-]		
H/T [-]	8 kn	9 kn	10 kn	8 kn	9 kn	10 kn	8 kn	9 kn	10 kn
Deep	0.050	0.065	0.082	0.026	0.033	0.041	0.896	0.899	0.901
3	0.11	0.14	0.18	0.028	0.037	0.048	0.874	0.880	0.879
1.5	-	0.36	0.53	-	0.085	0.19	-	0.693	0.600
1.35	0.30	0.44	0.70	0.087	0.20	0.44	0.342	0.278	0.403

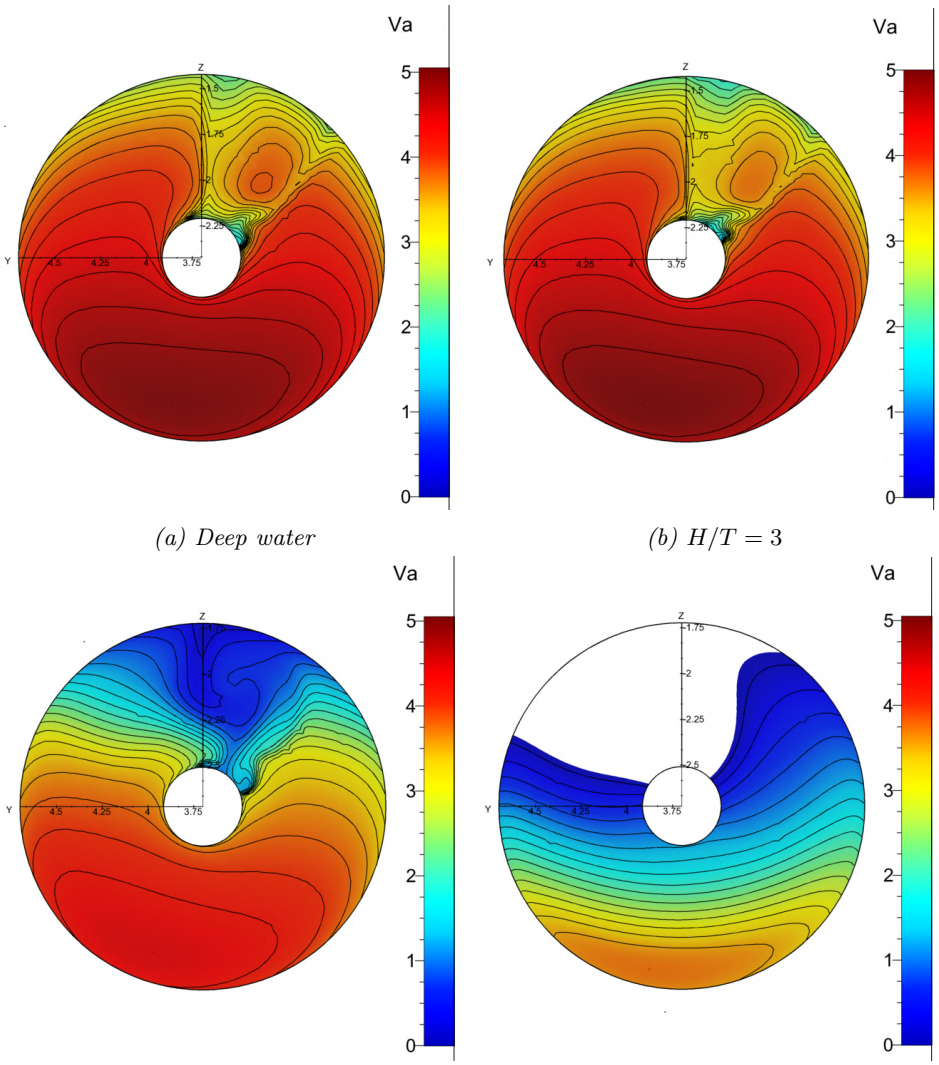

(a) Deep water *(b) $H/T = 3$*

(c) $H/T = 1.5$ *(d) $H/T = 1.35$*

Figure 7.12: Inland ship reference case: comparison of the instantaneous nominal wake field between different water depths at 9 knots. The white areas represent flow separation.

It is visible in figures 7.11 and 7.12 that flow separation is present in front and inside of the propeller plane in very shallow water ($H/T = 1.5$ and $H/T = 1.35$). The nominal wake field is consequently dominated by flow separation. However, those results were obtained from CFD simulations without propeller action. In reality, a ship always operates with propeller action. Therefore one CFD simulation was performed including the actuator disk in shallow water ($H/T = 1.35$, $v_s = 9$ knots and no air cavities) to investigate if flow separation is also present in the propeller plane with air on. Figure 7.13 shows a comparison of the nominal wake field (without actuator disk) and the total wake field (with actuator disk). The figure shows that flow separation is no longer present in the wake field with the actuator disk on. The suction of the propeller removes the flow separation in front and inside of the propeller plane.

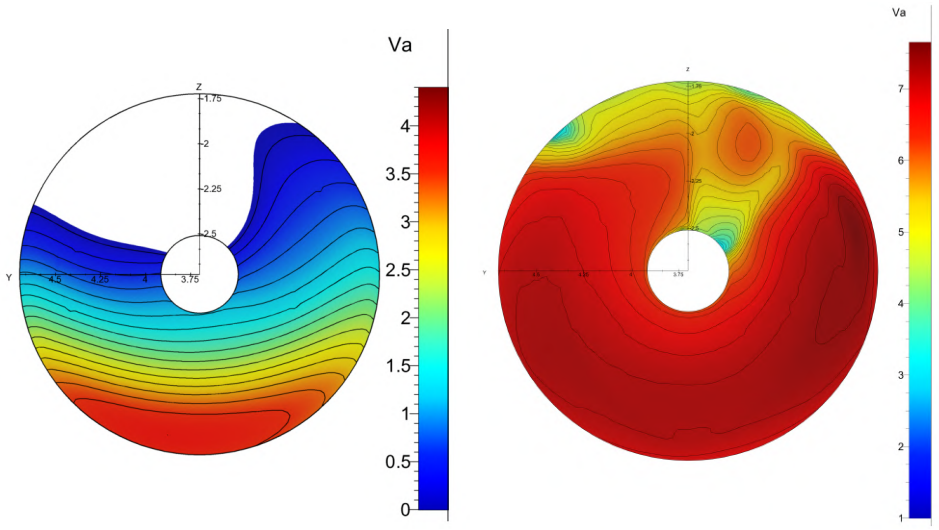

(a) Nominal wake field *(b) Total wake field*

Figure 7.13: Inland ship reference case: comparison of the nominal (without actuator disk) and total wake field (with actuator disk) at 9 knots, $H/T = 1.35$.

No power speed calculation is performed for the ship in shallow water. For the inland ship, it seemed unnecessary to repeat a detailed investigation including the actuator disk model, see also section 7.4.1. However, in shallow water, the thrust deduction effect also changes, especially in very shallow water, (Raven, 2022). Furthermore, according to Rotteveel (2019) the difference between nominal and effective wake field increases in shallow water. All previous power predictions were made assuming that the nominal wake factor is equal to the effective wake factor. This assumption would be less accurate in shallow water. However, it should be evident that the propeller efficiency will also change significantly, especially in very shallow water due to the large change in the resistance and the wake field.

7.5.4 Air lubrication in shallow water

In section 2.7 it is explained in detail that the maximum stable cavity increases in shallow water as a function of the depth-based Froude number. It should be evident that the air cavity length increase should be computed for the depth-based Froude number based on the under-keel clearance $Fr_{h,cav}$ and not based on the total water depth because the cavities are formed under the bottom of the hull. The air cavities become supercritical when $Fr_{h,cav} > 1$. Theoretically, the cavity length approaches infinity in that case, this was also observed during experimental tests, (Zverkhovskyi, 2014). In table 7.14 the depth-based Froude number for the ship Fr_h, for the air cavities $Fr_{h,cav}$ and the theoretical cavity length increase are given. The table shows that air cavities can be supercritical whereas the flow around the ship is not yet supercritical.

Table 7.14: Depth-based Froude number and cavity length for the different water depths and speeds.

	Fr_h [-]			$Fr_{h,cav}$ [-]			$L_{cav,s}/L_{cav,d}$ [-]		
H/T [-]	8 kn	9 kn	10 kn	8 kn	9 kn	10 kn	8 kn	9 kn	10 kn
3	0.397	0.447	0.496	0.486	0.547	0.608	1.000	1.003	1.009
2	0.486	0.547	0.608	0.688	0.774	0.860	1.034	1.101	1.269
1.5	0.562	0.632	0.702	0.973	1.094	1.216	2.542	∞	∞
1.35	0.592	0.666	0.740	1.163	1.308	1.453	∞	∞	∞

For the present analysis, the cavity length is not modified in shallow water but kept the same as in deep water. It is assumed that the aspect ratio of the cavities is unchanged by the shallow water effect. As a result, the cavity length is limited by the skeg height for all cases similar to the deep water case. The assumption of a fixed cavity aspect ratio might be correct for cases where the shallow water effect is not so strong (e.g. $H/T = 3.0$). However Zverkhovskyi (2014) that the aspect ratio of a cavity

might increase significantly (the cavity gets thinner) when approaching supercritical flow. However, due to the low skeg height of the inland ship (6cm) the cavity length in deep water is already limited by the skeg height at 6.5 knots. The investigation is made at 8,9 and 10 knots. Therefore the cavity length might still be limited by the skeg height although its aspect ratio increases in shallow water. Furthermore, no proper comparison can be made when both the cavity length and the water depth change. Therefore the cavity length is approximated constant. Further research is required on how the cavity length under a ship can accurately be predicted in shallow water.

In table 7.15 the reduction in resistance caused by the air cavities is given for different water depths. The values are also plotted in figure 7.14. For viscous resistance, a clear trend can be seen. Apart from some spread in the data, the friction reduction in percentage seems to be approximately constant irrespective of the water depth. The absolute friction drag reduction increases in shallow water due to the increase of the viscous drag. If only a frictional drag reduction had been present, the total resistance reduction would have increased in shallow water, because more frictional resistance is present in shallow water (no air). Whereas the percentage of frictional drag reduction stays approximately constant in shallow water. It should be noted that the added resistance of the DACS appendage will also increase in shallow water. It was also found that the trim and sinkage of the ship in shallow water was not affected by the air cavities. This observation was also made by Galushina et al. (2020).

Table 7.15: Inland ship: change in resistance for different water depths. Each result is a comparison between air on and air off at its respective water depth.

	ΔR_v [%]			ΔR_p [%]			ΔR [%]		
H/T [-]	8 kn	9 kn	10 kn	8 kn	9 kn	10 kn	8 kn	9 kn	10 kn
Deep	-30.1	-29.9	-29.7	6.2	7.9	-2.2	-14.7	-13.2	-16.1
3	-	-30.6	-30.5	-	-1.4	2.8	-	-17.3	-14.3
1.35	-30.0	-28.7	-	-5.8	-6.1	-	-16.2	-13.6	-

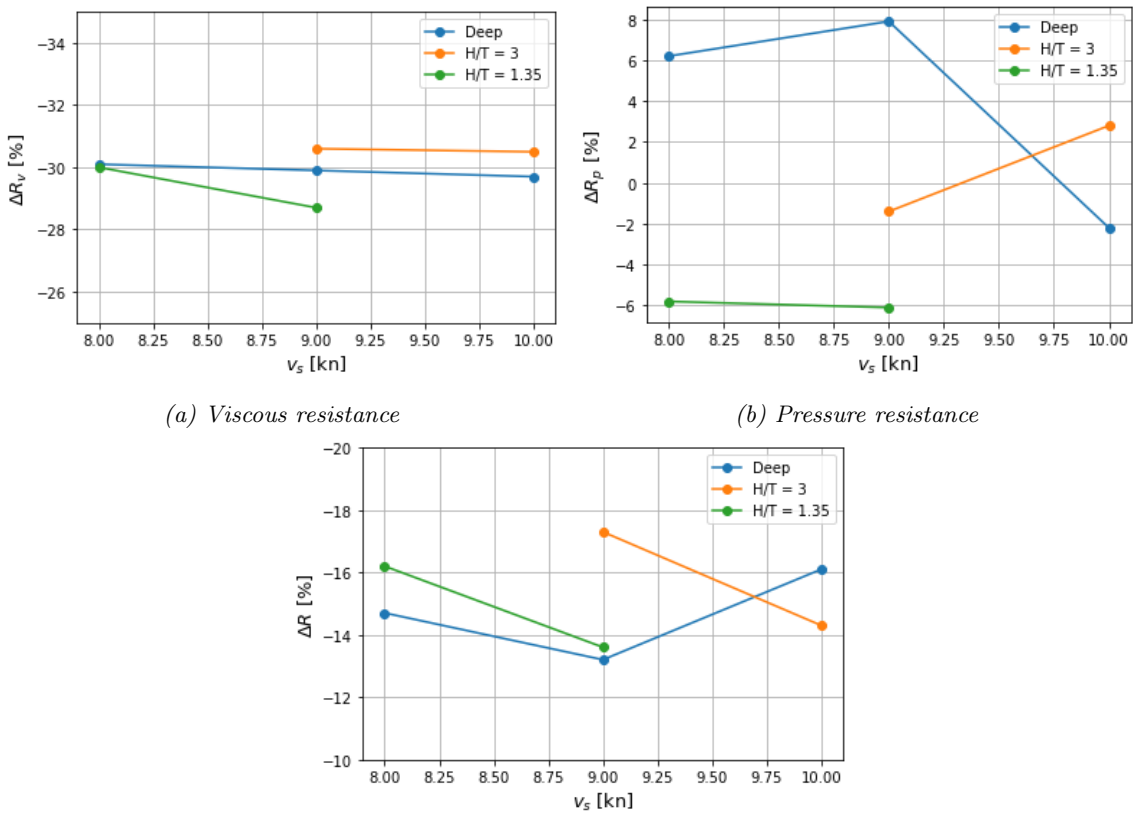

(a) Viscous resistance

(b) Pressure resistance

(c) Total resistance

Figure 7.14: Inland ship: change in the resistance due to the air cavities for different speeds and water depths.

There is a big spread in the data for the pressure resistance. This spread was also present in deep water. A slight decrease in the pressure resistance is observed for most data points in shallow water. In deep water, there is a slight increase of the pressure resistance for most data points. However, the reverse is also visible for a few other points. Figures 7.15 and 7.15 show a comparison of the instantaneous flow separation at the stern between air on and air off for different water depths. No significant changes are observed between the reference case and air on.

The same statements regarding the differences in pressure resistance and flow separation between the reference case and air-on conditions, as discussed in the deep water results (see section 7.4), also apply to the shallow water results. It is not possible to judge the change in flow separation from an instantaneous comparison of a quasi-static simulation. Furthermore, the uncertainty on the pressure resistance and the flow separation prediction is probably significant. Again, no comprehensive conclusions can be drawn about whether the pressure resistance and flow separation at the stern in shallow water are affected by the air cavities. These effects could also be due to numerical and modeling uncertainties.

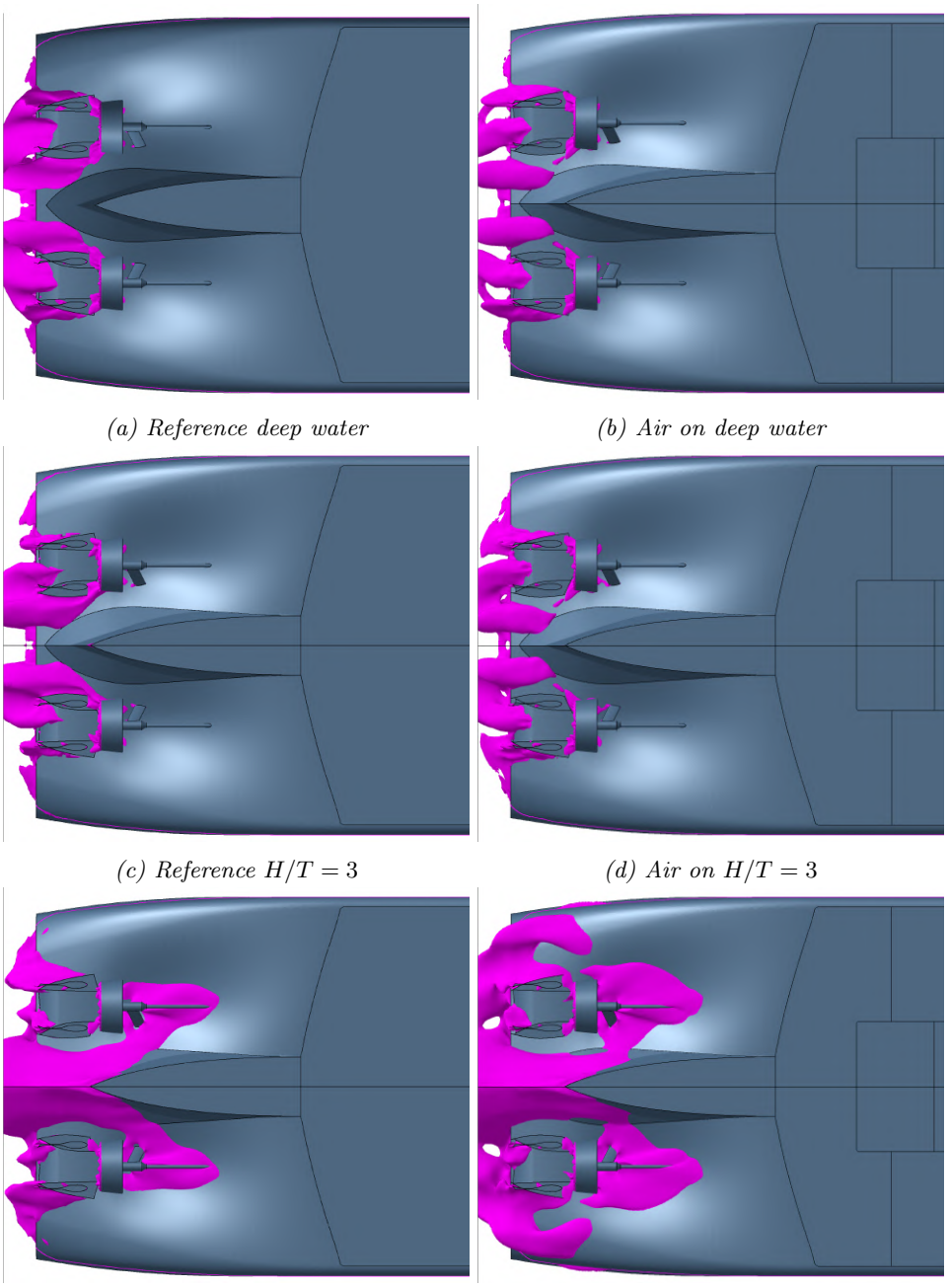

(a) Reference deep water *(b) Air on deep water*

(c) Reference $H/T = 3$ *(d) Air on $H/T = 3$*

(e) Reference $H/T = 1.35$ *(f) Air on $H/T = 1.35$*

Figure 7.15: Inland ship: comparison of instantaneous flow separation between different water depths between the reference case and air on, bottom view.

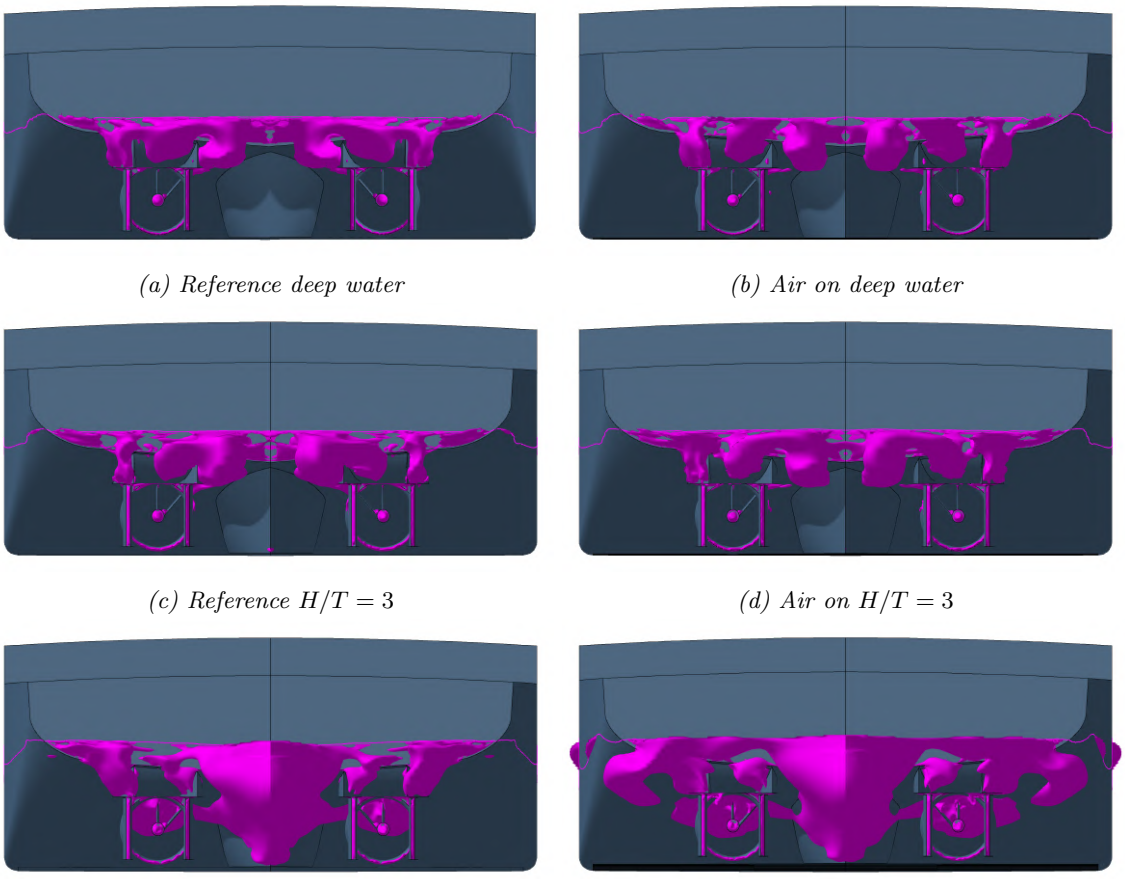

(a) Reference deep water

(b) Air on deep water

(c) Reference $H/T = 3$

(d) Air on $H/T = 3$

(e) Reference $H/T = 1.35$

(f) Air on $H/T = 1.35$

Figure 7.16: Inland ship: comparison of instantaneous flow separation between different water depths between the reference case and air on, stern view.

Table 7.16 shows a comparison of the nominal wake factor with air on and air off in deep and in shallow water. For a speed of 9 knots the instantaneous nominal wake fields are also plotted in figure 7.17. The table shows that the air cavities cause a slightly larger change of the nominal wake factor at $H/T = 3$ than in deep water. At $H/T = 1.35$ a much larger difference is visible. At this water depth the nominal wake field is strongly influenced by flow separation. It appears as if less flow separation is present in the wake field with air on. "However, as explained in Section 7.5.3, flow separation is an unsteady process, making the nominal wake field also unsteady. Therefore no firm conclusions on the change in flow separation in the nominal wake field can be made by only comparing the instantaneous flow wake field which is computed from a quasi-static simulation. The comparison of the nominal wake factor in table 7.16 at $H/T = 1.35$ is therefore only indicative.

Table 7.16: Inland ship: comparison of the nominal wake factor for different speeds and water depths between air on and air off.

	8 kn			9 kn			10 kn		
H/T [-]	Ref	Air on	Diff. [%]	Ref	Air on	Diff. [%]	Ref	Air on	Diff. [%]
3	0.874	-	-	0.880	0.943	7.2	0.879	0.942	7.2
1.35	0.342	0.703	105.6	0.278	0.622	123.8	0.403	-	-
Deep	0.896	0.950	6.0	0.899	0.949	5.6	0.901	0.952	5.7

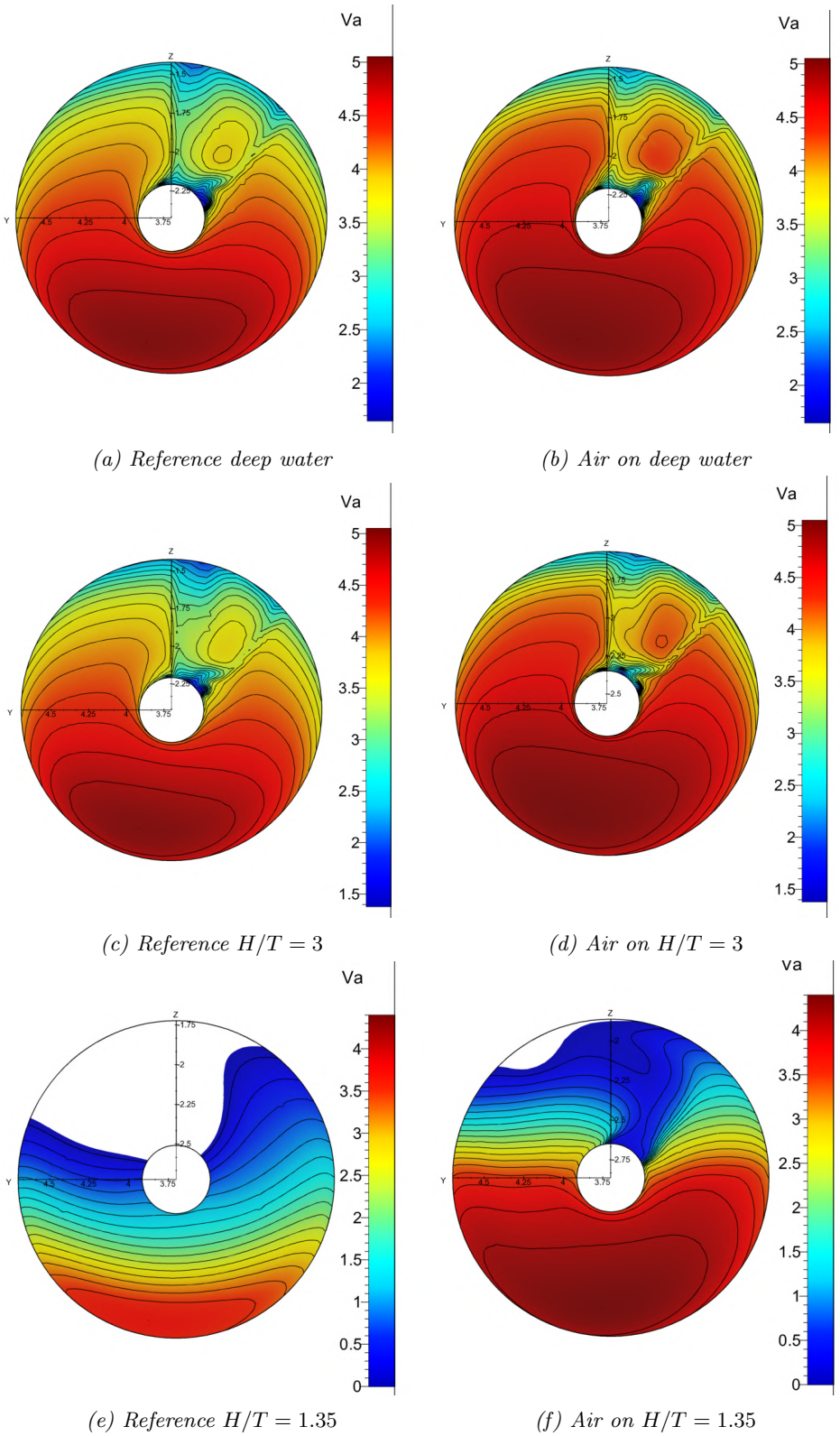

(a) Reference deep water *(b) Air on deep water*

(c) Reference $H/T = 3$ *(d) Air on $H/T = 3$*

(e) Reference $H/T = 1.35$ *(f) Air on $H/T = 1.35$*

Figure 7.17: Inland ship: comparison of the instantaneous nominal wake field between different water depths between the reference case and air on. The white areas represent flow separation.

7.6 Conclusion

A case study was performed for an inland ship with an air cavity system both in deep and shallow water. The frictional resistance of the ship was reduced by 30% in deep water due to the large reduction of the wetted area. For the pressure resistance, no clear trend was observed due to scatter in the data. The flow separation at the stern and transom of the ship was slightly changed with air on. However, it is unclear if the change in pressure drag and flow separation is caused by the air cavities. It could also be caused by the numerical and modeling uncertainty of the used CFD method. Furthermore, a decrease of the nominal wake field of 5% was observed, although the ship is a twin-screw vessel. The propeller efficiency was slightly increased (1-2%) by the air cavities. Consequently, the power reduction caused by the air cavities is lower than the reduction in resistance due to a slight decrease in propulsive efficiency.

In shallow water, not all CFD simulations finished successfully, despite the effort made to reduce grid deformation due to the squat effect. Still, enough data points were obtained to draw conclusions. More research is recommended, to improve the guidelines for CFD simulations in shallow water. Without air, an increase in friction drag of up to 30% was observed depending on the water depth. The increase in pressure drag was more significant due to excessive flow separation at the most shallow water depth. The wake factor increased in shallow water. In the most shallow case, separated flow is present in the wake field.

The relative reduction of the frictional drag caused by the air cavities is approximately constant for all water depths. The absolute reduction in frictional drag is larger because more frictional drag is present in shallow water. No comprehensive conclusion could be made for the pressure drag, because of the spread in the available data. The reduction of the nominal wake field is increased by the air cavities in shallow water. However, the change in nominal wake field in very shallow water is less evident due to separation being present in the wake field.

Chapter 8
Discussion

In this chapter some drawbacks and limitations of the methods used in this research are studied. Furthermore, several observations made in other chapters are investigated in more detail. First of all the change in propeller efficiency due to air cavities is studied. Afterwards, a comparison of the drag reduction efficiency of all four ships is considered. Lastly, the effect of the air cavities on the draft of the ship is studied.

8.1 Propeller efficiency

For all ships studied it was observed that the propeller efficiency changed due to the air cavities. For the cruise ship and the inland ship, a minor increase in efficiency of 1-2% was obtained. However, for the cargo ship changes up to 5% were found (decrease at low speed and increase at higher speeds). The change in propeller efficiency depends on several factors: the resistance reduction, the change in wake field, and the propeller operating point for the ship without air cavities. In this section, the influence of all parameters is investigated.

For a fixed pitch propeller the propeller open water efficiency η_o can be obtained from the propeller open water diagram. For each ship speed a $K_{T,ship}$ curve can be constructed using equation 8.1. The propeller working point is located at the intersection point between the $K_{T,ship}$ curve and the propeller K_T curve in the open water diagram. η_o can be read from the advance ratio at the propeller operating point. (Klein Woud & Stapersma, 2017).

$$K_{T,ship} = c_7 \cdot J^2 \tag{8.1}$$

$$c_7 = \frac{R_{cor}}{\rho D^2 k_p (1-t)(1-w)^2 v_s^2} \tag{8.2}$$

The calculations will be made for the inland ship. This ship has 2 4-bladed Kaplan propellers in a nozzle. Table 8.1 shows the values used in the calculation procedure. The values have been approximated from the results of the inland ship. However, the calculations in this section are purely presented for explanation purposes and could be performed for any ship and propeller.

Table 8.1: Properties used for the calculation of the propeller efficiency.

Ship speed v_s [kn]	10.4
Resistance R [kN]	140
Wake factor $(1-w)$ [-]	0.9
Thrust deduction factor $(1-t)$ [-]	0.9
Blade area ratio A_e/A_0 [-]	0.8
Pitch ratio P/D [-]	1.028

First of all, the propeller working point is computed for the reference case (the ship without drag reduction) and for the ship with 5, 10, 15, and 20% drag reduction. The change in the working point of the propeller depends on the original working point of the propeller. Three cases are considered:

- Case 1: original working point slightly before the peak of the propeller efficiency curve (10.4 knots).
- Case 2: original working point at a lower efficiency, before the peak of the propeller efficiency curve (8 knots)
- Case 3: original working point approximately at maximum propeller efficiency (13 knots)

All cases could occur in practice depending on the design and loading condition of the ship. The original working point is varied by varying the ship speed, while keeping all other parameters, including the resistance fixed. The results of this analysis are presented in table 8.2 and figure 8.1. The results show that the change in propeller efficiency increases if the drag reduction increases. Furthermore, the change also depends on the original working point. An increase in efficiency is found for cases 1 and 2. For case 2 the increase in propeller efficiency is larger because in that region the propeller efficiency curve has a steeper slope. For case 3, a decrease in efficiency is obtained, because the ship without air cavities was operating at the maximum propeller efficiency. It should be noted that the exact change in propeller efficiency is different for each propeller. However, the trend will be similar.

Table 8.2: Comparison of the change in the propeller efficiency for different original working points and different drag reduction rates.

	Case 1		Case 2		Case 3	
	η_o [-]	Diff. [%]	η_o [-]	Diff. [%]	η_o [-]	Diff. [%]
Ref	0.569	-	0.533	-	0.580	-
$0.95 \cdot R$	0.572	0.41	0.537	0.83	0.580	-0.04
$0.9 \cdot R$	0.574	0.80	0.542	1.68	0.579	-0.14
$0.85 \cdot R$	0.576	1.15	0.546	2.54	0.578	-0.32
$0.8 \cdot R$	0.577	1.45	0.551	3.40	0.577	-0.59

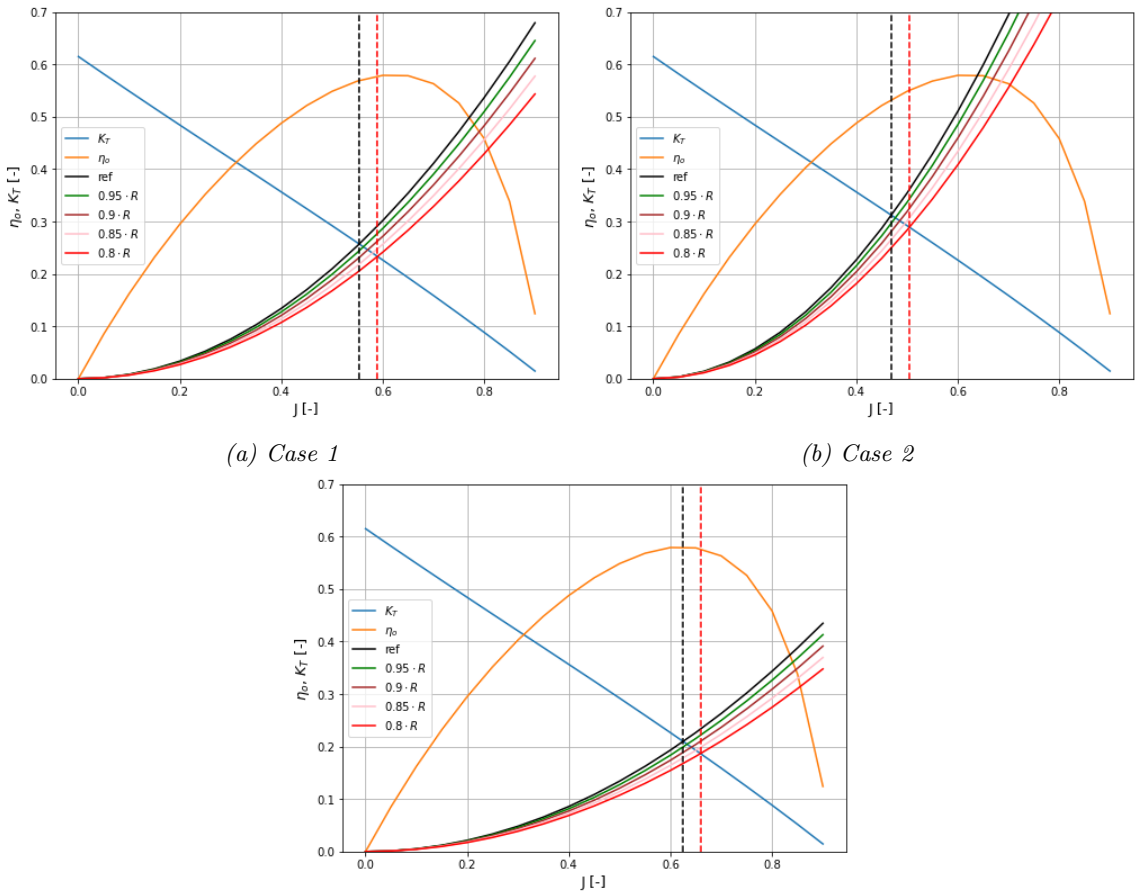

(a) Case 1

(b) Case 2

(c) Case 3

Figure 8.1: Comparison of the change in the propeller working point for different original working points.

8.1.1 Change in wake fraction

For the cargo ship and the inland ship, it was observed that the air cavities also caused a decrease of the wake fraction w. The propeller working point is also a function of the wake fraction, see equation 8.2. This is illustrated in table 8.3 and figure 8.2. The computation was made for case 1. The table and figure show that the change in propeller efficiency is increased if both the wake fraction and the resistance are reduced.

Table 8.3: Comparison of the change in propeller efficiency in case of both a resistance reduction and a change of the wake fraction.

	η_o [-]	Diff. [%]
Ref	0.569	-
$0.9 \cdot R$	0.574	0.80
$0.9 \cdot R$ and $1.05 \cdot (1 - w)$	0.577	1.36
$0.8 \cdot R$	0.577	1.45
$0.8 \cdot R$ and $1.1 \cdot (1 - w)$	0.579	1.72

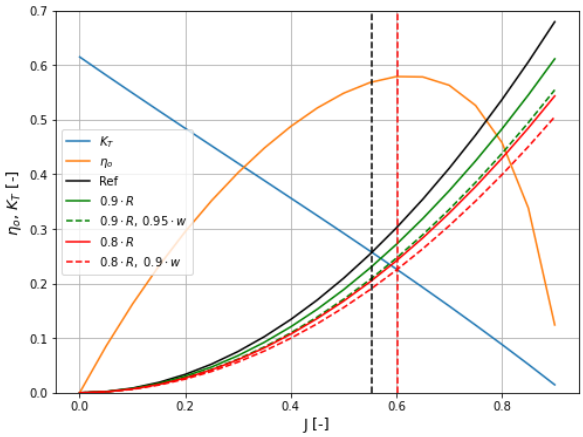

Figure 8.2: Comparison of the change in the propeller working point in the open water diagram in case of both a resistance reduction and a change of the wake fraction.

8.1.2 Controllable pitch propeller

For the general cargo ship, a larger difference in propeller efficiency was observed than for the other ships (up to 5% increase at the highest speed). This can be explained by the fact that the ship has a controllable pitch propeller operating at a fixed rpm. Such a propeller is the most efficient in the design condition. In off-design conditions, the efficiency of the ship decreases more rapidly than for a fixed-pitch propeller because the propeller keeps operating at the same rpm, (Klein Woud & Stapersma, 2017). Therefore the change in propeller efficiency is also larger. Furthermore, the cargo ship has both a significant change in the wake field and resistance.

8.1.3 Propeller optimization

It could also be a possibility to optimize the propeller in combination with the air lubrication system. Whether changing the propeller design is useful depends on the original working point of the ship. For a new-build ship the propeller should operate at the working point with the highest efficiency in the design condition. The air lubrication will then cause a decrease in propeller efficiency if the propeller is designed without the air lubrication system, see case 3. However, the propeller efficiency curve is relatively flat in the region close to the optimum. Table 8.2 showed that even a 20% reduction in resistance causes only a 0.6% decrease of propeller efficiency. Therefore, it is most likely not worth it to change the propeller design for a new-build ship or for a refit of a ship with a propeller operating at the optimum point without the air lubrication system.

This is a different story for a ship that is not operating at maximum propeller efficiency. In that case, the propeller efficiency might increase due to the air cavities (case 1 and case 2). However, in such a case it might be worth changing the propeller anyway, regardless of the installment of an air lubrication system. This could e.g. be relevant for a ship of which the typical operational condition is no longer the same as the design condition.

8.2 Drag reduction efficiency

In section 2.1.4 it was already explained that the frictional drag reduction caused by the air cavities is lower than when the frictional drag reduction would be computed based on the reduction in wetted area. This is because a new boundary layer is formed behind each cavity, resulting in higher local skin friction. This phenomenon can be modeled by the drag reduction efficiency coefficient EF. EF is defined as the ratio of the actual friction drag caused by the air cavities over the wetted area reduction:

$$EF = \Delta R_. \frac{S_{wet}}{S_{cav}} \tag{8.3}$$

with ΔR_v the frictional drag reduction, S_{wet} the wetted area and S_{cav} the area covered by the air cavities. Table 8.4 shows the value of EF for all the different air cavity layouts that were modeled in this thesis. These values could be used for design and fuel-saving predictions for new air cavity systems. The results show that EF can be increased by maximizing the air-covered area of the bottom and minimizing the distance in between the air cavities.

Table 8.4: Drag reduction efficiency coefficient for different air cavity layouts.

	S_{cav}/S_{bottom} [-]	S_{cav}/S_{wet} [-]	$\Delta R_{v,avg}$ [-]	EF
Inland ship	0.722	0.407	0.299	0.736
Cruise ship	0.602	0.168	0.122	0.728
General cargo ship $L_{cav} = 100\%$	0.792	0.384	0.319	0.831
General cargo ship $L_{cav} = 87\%$	0.689	0.334	0.265	0.794
General cargo ship $L_{cav} = 74\%$	0.587	0.285	0.214	0.753

8.3 Change in draft

Zverkhovskyi (2023) suggested that the draft of a ship will decrease if air cavities are created under the bottom of the hull. This is not included in the modeling method, because the cavities are modeled as flat surfaces. A simple calculation can be made to estimate the consequences of this effect. The relation between the displacement ∇ and the mass of a ship m is determined by Archimedes' principle:

$$m = \rho \cdot \nabla \tag{8.4}$$

The mass of the ship will not change. Therefore, the total displaced volume of water ∇ will also be constant when the air supply is on and air cavities are formed on the bottom of the ship, assuming that the mass of air is negligible compared to the mass of the ship. However, the air cavities also have a certain volume. As a result, the hull will be lifted slightly up. This causes a slight reduction of the draft. Therefore, the total volume of displaced water ∇ will stay constant, whereas the underwater volume of the hull V_{ship} will decrease. This can be expressed with the following relation:

$$\nabla = V_{ship,0} = V_{ship,1} + V_{cav} \tag{8.5}$$

with ∇ the total displacement, $V_{ship,0}$ the underwater volume of the hull without air supply, $V_{ship,1}$ the underwater volume of the hull with air on, and V_{cav} the volume of the cavities. The change in the underwater volume of the hull ΔV can then be expressed as:

$$\Delta V_{ship} = V_{ship,0} - V_{ship,1} = V_{cav} \tag{8.6}$$

For small changes in underwater volume ΔV_{ship}, it can be usually assumed that the waterline area A_{wl} of a ship stays constant. A small change in draft ΔT can then be computed as:

$$\Delta T = \frac{\Delta V_{ship}}{A_{wl}} \tag{8.7}$$

In this case, the change in underwater volume of the hull ΔV_{ship} equals the cavity volume V_{cav}. Therefore the change in draft ΔT due to air cavities equals:

$$\Delta T = \frac{V_{cav}}{A_{wl}} \tag{8.8}$$

With the above-described relations, an approximation can be made for the general cargo ship. The volume of the air cavities should be approximated to do this. Zverkhovskyi et al. (2015) suggested that the shape of an air cavity can be approximated as an ellipse (looking from a 2D perspective). The area of the half ellipse can be computed as:

$$A_{ellipse} = \pi/4 \cdot L_{cav} \cdot t_{cav} \tag{8.9}$$

V_{cav} can then be computed as the sum of the width of each cavity multiplied by the area of half an ellipse:

$$V_{cav} = A_{ellipse} \cdot \sum_{n} W_{cav,n} \tag{8.10}$$

A computation is made for the cargo ship based on the above-described derivation. The results are presented in table 8.5. It should be noted that the general cargo ship has a relatively large air-covered area. Furthermore, the assumed air-covered area is an optimistic approximation and a best-case scenario. Still, the draft of the ship decreases by only 0.76 %. Therefore it seems a valid approximation to neglect this change in draft in the CFD simulations.

Table 8.5: Changes caused by the cavity volume under the general cargo ship.

Cavity volume V_{cav} [m^3]	61.26
Change in draft ΔT [m]	0.037
Change in draft ΔT [%]	-0.76

Chapter 9
Conclusion

The goal of this thesis was to answer the main research question:

How does an external air cavity system affect the propeller performance of a ship?

The main research question is divided into several subquestions. They are answered based on the results of the three case studies.

9.1 Propeller-hull interaction

How does the propeller-hull interaction change? Firstly, it was found that the thrust deduction effect is not significantly influenced by the air cavity system. While minor variations in the thrust deduction factor were observed, these changes were typically less than 1%. Therefore it can be concluded that the change in thrust deduction caused by the air cavities is insignificant. The wake field, however, can be influenced significantly by the air cavity system. For all three ships, it was observed that the structure of the nominal wake field remains similar. In contrast, the average axial velocity in the wake field (the wake fraction) was affected. The physical interpretation for the lower wake fraction is that a friction reduction (due to air cavities) is always associated with changes in the hull boundary layer and wake. The change in wake fraction depends on the ship type. For a full single-screw vessel a large decrease in the nominal wake fraction was observed, 7-12% decrease depending on the cavity length. For twin-screw vessels, this effect is less stringent. For a slender cruise ship with podded propulsion, the wake field was almost not affected. However, for a twin-screw inland ship with a large air-covered area still a 5% decrease in wake fraction was observed.

Based on these results some qualitative statements on the wake fraction reduction can be made. First of all, the reduction increases for a larger air-covered area. This is clearly visible from the results of the general cargo ship. Secondly, the reduction increases for ships with a larger wake fraction, because the effect of the boundary layer is more prominent in the wake field. Consequently, also a change in the boundary layer will be more prominently visible in the wake field. A ship with a high block coefficient (full hull form) will typically have a larger reduction of the wake fraction than a more slender ship. Usually, such a ship has a higher wake fraction and a larger flat bottom area. Lastly, for twin-screw ships, the reduction is usually low, because the propellers mainly operate outside of the ship's boundary layer. However, this depends on the exact propeller location and the influence of the bottom boundary layer on the propeller wake field.

9.2 Propeller efficiency

How does the propeller efficiency change? The propeller efficiency is affected because the propeller working point in the open water diagram is changed. The change depends on the resistance reduction, the change in the wake field, and the original working point of the propeller (without air). A larger drag reduction also causes a larger change of the propeller efficiency. If the wake fraction is decreased by the air cavities, the change in propeller efficiency is larger. The propeller efficiency can either increase or decrease depending on the original working point of the propeller. For a ship with a CPP propeller operating at a fixed rpm it was found that the propeller efficiency decreased at low speed and increased at a higher speed. It should be noted however that such a ship typically sails at a fixed speed.

Depending on the original working point of the propeller it might or might not be beneficial to also consider optimization of the propeller in combination with the DACS system. It was found that the change in propeller efficiency due to air lubrication is small for a ship of which the propeller is operating at the optimum point without the air lubrication system. This is because the propeller efficiency curve is relatively flat in the region close to the optimum. For a refit case, (for a ship with

a non-optimal propeller) it might be more rewarding to also refit the propeller. However, in that case it could be also rewarding without considering the air lubrication system.

9.3 Power saving predictions

How does the change in propeller performance affect the estimated power savings of the system? Typically, a power saving estimation for an air lubrication system is made by assuming that only the frictional drag is changed, (Mäkiharju et al., 2012) and (Kim & Steen, 2023). However, this research shows that it is not always a good assumption because the propeller efficiency and the wake fraction also change. The reduction in wake fraction causes a decrease of the hull efficiency and hence a lower reduction in power than when only the resistance reduction would be considered. The change in propeller efficiency also plays a role. For all ships, it was observed that the reduction in propulsive efficiency was secondary compared to the resistance reduction so still power savings can be made. However, for more accurate predictions the change in propulsive efficiency should be considered. From a commercial perspective, it is important to include the change in propulsive efficiency in power-saving predictions to not make too optimistic promises on the reduction in fuel consumption.

9.4 Shallow water

What is the influence of the shallow-water effect? Observations in shallow water are made assuming a fixed cavity length (independent of the water depth). It was found that the relative frictional drag reduction caused by the air cavity system is approximately constant. In shallow water, the frictional drag of a ship increases so a larger absolute frictional drag reduction can be obtained. It was found that for the inland ship that was investigated in this research, the pressure drag increase in shallow water is larger than the frictional drag increase. Consequently, the total resistance reduction in percentage will be lower in shallow water, however, the absolute value of the total resistance reduction will be larger. It should be noted that the added resistance of the appendages will also increase in shallow water. It was also observed that the air cavities affect the pressure drag. This effect is different in shallow water than in deep water. However, a larger spread in the data is observed so no conclusions can be made. Regarding the wake field it was found that the change in the nominal wake field caused by the air cavities is larger in deep water than in shallow water.

9.5 Other observations

Some other observations can also be made. For the general cargo ship, it was observed that air cavities also cause a reduction of the pressure drag. This is most likely because flow separation on the aft ship and gondola is reduced due to the thinner boundary layer. For the inland ship, it was found that the flow separation at the transom was also changed, however, no comprehensive conclusions can be made for it due to the large spread in the data. Therefore there is a strong hypothesis that air cavities can also reduce the viscous pressure resistance and the flow separation at the stern of a ship. However more research, e.g. with more advanced CFD models, is required to strengthen this statement, see also next chapter.

Furthermore, the case study of the cruise ship showed that the resistance reduction, change in propeller hull interaction, and propeller efficiency can be predicted reasonably accurately (1-2% difference) by modeling the air cavities as surfaces with a slip boundary condition given that the cavity length is known. However, for the cruise ship, the cavity length could be observed from model tests. For other ships, the uncertainty is larger because the aspect ratio of the air cavities is not always constant. However the results of the cruise ship show that still accurate predictions can be made for for an assumed cavity length.

Chapter 10
Recommendations

This study's results highlight several opportunities for further research. First of all, the predictions in this thesis are based on an assumed cavity length, which introduces uncertainty. For example, during model tests of the cruise ship, a shorter cavity length than expected was observed, see section 6.2. Therefore, a more accurate prediction of the cavity length is required.

Related to this is the fact that it is currently not feasible to resolve the airflow of the cavities underneath a ship using CFD, see section 2.5. Further research into the numerical modeling of the two-phase flow for air cavities is recommended. Ideally, a two-phase RANS model should be developed that can be applied to ships with air cavities for both design and research purposes.

The added resistance of the air lubrication system appendages could also be investigated in more detail. Currently, only a prediction of the added resistance of the skegs is made for the cargo ship. However, the cavitators also cause a drag increase. For the cruise ship the added resistance was approximated based on model test results. A more accurate prediction will also improve the accuracy of power-saving predictions.

Additionally, this thesis found that air cavities can affect the pressure drag and flow separation behavior of a ship both in deep and in shallow water. It is questionable whether these effects are accurately resolved with the employed modeling method (quasi-static simulation, k-omega SST turbulence model with wall functions). A considerable spread in the results was observed, particularly for the inland ship. Therefore, a more detailed study into if and how air cavities change the flow separation of a ship in deep and shallow water is necessary. This can be achieved by e.g. comparing the results of different turbulence models.

In this study, the propeller-hull interaction is modeled using simplified models. The thrust deduction effect is modeled using an actuator disk model, and the wake fraction is retrieved from the nominal wake field. The actuator disk model is a simplified model and the nominal wake field excludes the effects of the propeller. Repeating one of the case studies with a more sophisticated model, such as the RANS-BEM method or simulating a fully discretized propeller using a sliding mesh technique, would be worthwhile. This could yield a more detailed understanding of the effects of air lubrication on propeller-hull interaction.

Furthermore, this thesis investigated two twin-screw ships and one single-screw vessel. It is recommended to study more single-screw ship types, such as container ships. This could provide a better understanding of the relationship between hull form, air-covered area, and propulsion configuration on the effects of air cavities on the propeller wake field. Consequently, this would allow for more accurate predictions for future installations of the air cavity system.

This study provides an initial exploration of air lubrication in shallow water. However, several challenges arose when modeling the flow around a ship in such conditions. Issues included the occurrence of negative cells due to ship motions and diverging simulations during the CFD analysis in shallow water. These problems could not be resolved, making it necessary to troubleshoot these issues before further numerical analysis in shallow water can be performed.

Currently, comparisons are made at two different water depths. Studying a wider range of water depths would provide a more comprehensive understanding of flow physics. Additionally, considering the operational profile of an actual inland ship—specifically, how often shallow water effects are encountered—would result in more accurate power-saving predictions.

Lastly, during the research on shallow water, it was assumed that the aspect ratio of an air cavity does not change due to the shallow water effect. However, previous research indicates that the aspect ratio of a cavity can change when approaching supercritical flow, (Zverkhovskyi, 2014). A supercritical air cavity can easily occur within the typical operational profile of an inland ship. Therefore, further research is needed on air cavities in and near supercritical flow conditions.

Reference list

Amromin, E. (2016). Analysis of interaction between ship bottom air cavity and boundary layer. *Applied Ocean Research*, *59*, 451–458. https://doi.org/10.1016/j.apor.2016.03.009

Arakawa, D., Kawasima, H., & Kawakita, C. (2018). Numerical Estimation of Self-Propulsion Factors for Ship With Air Lubrication. *Proceedings of the International Ocean and Polar Engineering Conference*, 855–862. https://onepetro.org/ISOPEIOPEC/proceedings-abstract/ISOPE18/All-ISOPE18/ISOPE-I-18-195/20391

Barbaca, L., Pearce, B. W., & Brandner, P. A. (2017). Numerical analysis of ventilated cavity flow over a 2D wall mounted fence. *Ocean Engineering*, *141*, 143–153. https://doi.org/10.1016/j.oceaneng.2017.06.018

Cadence. (n.d.). FINE/Marine documentation platform. https://www.cadence.com/en_US/home/tools/system-analysis/computational-fluid-dynamics/fidelity/marine.html

Carlton, J. (2007). *Marine propellers and propulsion* (second). Elsevier. https://doi.org/10.1016/B978-0-7506-8150-6.X5000-1

Coleman, H. W., & Steele, W. G. (2018). *Experimentation, validation, and uncertainty analysis for engineers* (Fourth). https://doi.org/10.1002/9780470485682

Cucinotta, F., Guglielmino, E., Sfravara, F., & Strasser, C. (2018). Numerical and experimental investigation of a planing air cavity ship and its air layer evolution. *Ocean Engineering*, *152*, 130–144. https://doi.org/10.1016/j.oceaneng.2018.01.071

Damen Shipyards Group. (2023). *Damen Air Cavity System (DACS)*. https://www.damen.com/equipment/green-solutions/damen-air-cavity-system

Dyne, G. (1995). *The principles of propulsion optimization* (tech. rep.). The Royal Institution of Naval Architects.

Eça, L., & Hoekstra, M. (2011). On the application of wall functions in ship viscous flows. *IV International Conference on Computational Methods in Marine Engineering (MARINE 2011)*, 585–604. https://upcommons.upc.edu/handle/2117/333287

Eça, L., & Hoekstra, M. (2014). A procedure for the estimation of the numerical uncertainty of CFD calculations based on grid refinement studies. *Journal of Computational Physics*, *262*, 104–130. https://doi.org/10.1016/j.jcp.2014.01.006

Elbing, B. R., Mäkiharju, S., Wiggins, A., Perlin, M., Dowling, D. R., & Ceccio2, S. L. (2013). On the scaling of air layer drag reduction. *Journal of Fluid Mechanics*, *717*, 484–513. https://doi.org/10.1017/jfm.2012.588

Elbing, B. R., Winkel, E. S., Lay, K. A., Ceccio, S. L., Dowling, D. R., & Perlin, M. (2008). Bubble-induced skin-friction drag reduction and the abrupt transition to air-layer drag reduction. *Journal of Fluid Mechanics*, *612*, 201–236. https://doi.org/10.1017/S0022112008003029

European Commission Directorate-General for Environment. (2023). *Baltic sea shipping should avoid copper in antifouling paints and open-loop scrubbers to mitigate pollution.* https://environment.ec.europa.eu/news/baltic-sea-shipping-should-avoid-copper-antifouling-paints-and-open-loop-scrubbers-mitigate-2023-05-24_en

Foeth, E. (2008). Decreasing frictional resistance by air lubrication. *Proceedings of the 20th International HISWA Symposium on Yacht Design and Yacht Construction.* http://resolver.tudelft.nl/uuid:0bf34719-30cd-4685-8c04-9a62832d2f3d

Forgach, K. M. (2002). *Measurement uncertainty analysis of ship model resistance and self propulsion tests* (tech. rep.). David Taylor Model Basin. https://apps.dtic.mil/sti/tr/pdf/ADA409338.pdf

Galushina, M., Sverchkov, A., Chicherin, I., Fomichev, D., Schemelinin, L., & Cok, L. (2020). Ahydrodynamic parameters of air-cavity ship in a narrow fairway [in Russian]. *Transactions from the Krylov State Research Centre*, *1*(391), 11–28. https://doi.org/10.24937/2542-2324-2020-1-391-11-28

Goldstein, S. (1929). On the vortex theory of screw propellers. *Proceedings of the Royal Society of London. Series A, Containing Papers of a Mathematical and Physical Character*, *123*(792), 440–465. Retrieved April 17, 2024, from http://www.jstor.org/stable/95206

Gorbachev, Y., & Amromin, E. (2012). Ship drag reduction by hull ventilation from laval to near future: Challenges and successes. In ATMA (Ed.), *Proceedings of the conference of association*

technique maritime et aeronautique, https://www.atma.asso.fr/dyn/memoires/memoire_20.pdf

Gray-Stephens, A., Tezdogan, T., & Day, S. (2021). Minimizing Numerical Ventilation in Computational Fluid Dynamics Simulations of High-Speed Planning Hulls. *Journal of Offshore Mechanics and Arctic Engineering*, *143*(3), 031903. https://doi.org/10.1115/1.4050085

Hoang, C., Toda, Y., & Sanada, Y. (2009). Full Scale Experiment For Frictional Resistance Reduction Using Air Lubrication Method. *Proceedings of the International Ocean and Polar Engineering Conference*, 812–817. https://onepetro.org/ISOPEIOPEC/proceedings-pdf/ISOPE09/All-ISOPE09/ISOPE-I-09-368/1778678/isope-i-09-368.pdf

Iaccarino, G., Ooi, A., Durbin, P., & Behnia, M. (2003). Reynolds averaged simulation of unsteady separated flow. *International Journal of Heat and Fluid Flow*, *24*(2), 147–156. https://doi.org/10.1016/S0142-727X(02)00210-2

Insel, M. (2008). Uncertainty in the analysis of speed and powering trials. *Ocean Engineering*, *35*(11), 1183–1193. https://doi.org/10.1016/j.oceaneng.2008.04.009

International Maritime Organization. (2023). *Revised ghg reduction strategy for global shipping adopted.* https://www.imo.org/en/MediaCentre/PressBriefings/Pages/Revised-GHG-reduction-strategy-for-global-shipping-adopted-.aspx

ISO 15016: Guidelines for the assessment of speed and power performance by analysis of speed trial data. (2015). *International Organization for Standardization.* https://www.iso.org/standard/61902.html

ITTC. (2014). Recommended procedures and guidelines - practical guidelines for ship cfd applications. *Proceedings of the 29th International Towing Tank Conference.* https://www.ittc.info/media/9773/75-03-02-03.pdf

ITTC. (2017a). 1978 performance prediction method. *Proceedings of the 28th International Towing Tank Conference.* https://www.ittc.info/media/8017/75-02-03-014.pdf

ITTC. (2017b). Recommended procedures and guidelines - example of uncertainty analysis of resistance tests in towing tanks. *Proceedings of the 28th International Towing Tank Conference.* https://www.ittc.info/media/8003/75-02-02-021.pdf

ITTC. (2017c). Recommended procedures and guidelines - preparation, conduct and analysis of speed/power trials. *Proceedings of the 28th International Towing Tank Conference.* https://www.ittc.info/media/8370/75-04-01-011.pdf

ITTC. (2017d). Recommended procedures and guidelines - uncertainty analysis in cfd verification and validation, methodology and procedures. *Proceedings of the 28th International Towing Tank Conference.* https://www.ittc.info/media/8153/75-03-01-01.pdf

ITTC. (2017e). Recommended procedures and guidelines - uncertainty analysis, example for propulsion test. *Proceedings of the 28th International Towing Tank Conference.* https://www.ittc.info/media/8013/75-02-03-012.pdf

ITTC. (2021). Recommended procedures and guidelines - captive model test. *Proceedings of the 29th International Towing Tank Conference.* https://www.ittc.info/media/9683/75-02-06-02.pdf

Kawakita, C. (2013). Study on marine propeller running in bubbly flow. *Proceedings of Third International Symposium on Marine Propulsors*, *1*, 405–412. https://www.marinepropulsors.com/proceedings/2013/9A.3.pdf

Kim, Y., & Steen, S. (2023). Potential energy savings of air lubrication technology on merchant ships. *International Journal of Naval Architecture and Ocean Engineering*, *15*, 100530. https://doi.org/doi.org/10.1016/j.ijnaoe.2023.100530

Klein Woud, H., & Stapersma, D. (2017). *Design of propulsion and electric power generations systems.* The Institute of Marine Engineering, Science; Technology (IMarEST).

Korkmaz, K., Kim, K., Liefvendahl, M., Werner, S., & Orych, M. (2023). A validation study of full-scale CFD simulations for sea trial performance prediction of ships. *Proceedings of the 10th Conference on Computational Methods in Marine Engineering (Marine 2023).* https://doi.org/10.23967/marine.2023.124

Korkmaz, K. B., Werner, S., & Bensow, R. (2022). Scaling of wetted-transom resistance for improved full-scale ship performance predictions. *Ocean Engineering*, *266*, 112590. https://doi.org/10.1016/j.oceaneng.2022.112590

Larsson, L., & Raven, H. C. (2010). *Ship resistance and flow.* The Society of Naval Architects; Marine Engineers (SNAME).

Li, Z., Zhang, X., & Wan, D. (2022). Research progress on the hydrodynamic performance of water-air-bubble mixed flows around a ship. *Journal of Hydrodynamics*, *34*, 171–188. https://doi.org/10.1007/s42241-022-0026-3

Mäkiharju, S. A., Perlin, M., & Ceccio, S. L. (2012). On the energy economics of air lubrication drag reduction. *International Journal of Naval Architecture and Ocean Engineering*, *4*(4), 412–422. https://doi.org/10.2478/IJNAOE-2013-0107

MAN Energy Solutions. (2023). *Basic principles of ship propulsion* (tech. rep.). https://www.man-es.com/docs/default-source/document-sync/basic-principles-of-ship-propulsion-eng.pdf

Marine Insight. (2023). *What is squatting of ships?* https://www.marineinsight.com/naval-architecture/squatting-of-ships/

Matveev, K. (2003). Air-cavity ships are ready for a wider market. *Speed at Sea*, 13–16.

Mikulec, M., & Piehl, H. (2023). Verification and validation of cfd simulations with full-scale ship speed/power trial data. *International Journal of Naval Architecture and Ocean Engineering for Research and Development*, *74*(1), 41–62. http://dx.doi.org/10.21278/brod74103

Mukha, T., & Bensow, R. E. (2020). Flow dynamics in the closure region of an internal ship air cavity. *Ocean Engineering*, *216*, 108192. https://doi.org/10.1016/j.oceaneng.2020.108192

Murai, Y. (2014). Frictional drag reduction by bubble injection. *Experiments in Fluids*, *55*, 1773. https://doi.org/10.1007/s00348-014-1773-x

Nikolaidou, L., Laskari, A., van Terwisga, T., & Poelma, C. (2021). On the characteristics of air layer regimes. *11th International Symposium on Cavitation (CAV2021)*. http://cav2021.org/wp-content/uploads/2021/07/P00118_optimize-1.pdf

Numeca. (2024). *Cfd solutions*. https://www.numeca.de/en/products-cfd-solutions/

Orych, M., Werner, S., & Larsson, L. (2021). Validation of full-scale delivered power CFD simulations. *Ocean Engineering*, *238*, 109654. https://doi.org/doi.org/10.1016/j.oceaneng.2021.109654

Pavlov, G. A., Yun, L., Bliault, A., & He, S. (2020). ALS and ACC Propulsion. In *Air lubricated and air cavity ships: Development, design, and application* (pp. 369–414). Springer New York. https://doi.org/10.1007/978-1-0716-0425-0_7

Peifer, B. C., Callahan-Dudley, C., & Makiharju, S. A. (2020). Air layer on superhydrophobic surface for frictional drag reduction. *Journal of Ship Research*, *64*, 118–126. https://doi.org/https://doi.org/10.5957/jsr.2020.64.2.118

Ponkratov, D., & Struijk, G. D. (2024). Quantifying the uncertainty of high-fidelity speed/power trials. *Proceedings of the 8th Hull Performance Insight Conference (HullPIC), Pontignano, Italy*. https://www.marin.nl/en/publications/quantifying-the-uncertainty-of-high-fidelity-speed/power-trials

Raven, H. (2022). *A correction method for shallow-water effects on ship speed trials - the Raven Shallow-Water Correction* (tech. rep.). Marin. https://www.marin.nl/en/publications/a-correction-method-for-shallow-water-effects-on-ship-speed-trials

Roache, P. J. (1997). Quantification of uncertainty in computational fluid dynamics. *Annual Review of Fluid Mechanics*, *29*, 123–160. https://doi.org/10.1146/annurev.fluid.29.1.123

Rotte, G., Charruault, F., Kerkvliet, M., & van Terwisga, T. (2018). An investigation on the set-up of air cavity simulations using a scale resolving method. *Proceedings of the 21st Numerical Towing Tank Symposium, NuTTS*.

Rotte, G., Kerkvliet, M., & van Terwisga, T. (2017). On the turbulence modelling for an air cavity interface. *Proceedings of the 20th Numerical Towing Tank Symposium (NuTTS)*. https://www.marin.nl/en/publications/on-the-turbulence-modelling-for-an-air-cavity-interface

Rotte, G., Kerkvliet, M., & van Terwisga, T. (2019). Exploring the limits of RANS-VoF modelling for air cavity flows. *International Shipbuilding Progress*, *66*(4), 273–293. https://doi.org/10.3233/ISP-190270

Rotte, G., Kerkvliet, M., & van Terwisga, T. (2023). The resolved and unresolved issues and phenomena in numerical modelling of air cavity closure using a scale-resolving method. *Proceedings of the 25th Numerical Towing Tank Symposium, NuTTS*. https://blueoasis.pt/wp-content/uploads/2023/10/Nutts2023_proceedings_v4.pdf

Rotte, G., Zverkhovskyi, O., Kerkvliet, M., & van Terwisga, T. (2016). On the physical mechanisms for the numerical modelling of flows around air lubricated ships. *Proceedings of the 12th international conference on hydrodynamics -ICHD 2016*. http://resolver.tudelft.nl/uuid:7a5e44b8-7a1e-4402-b8eb-50cd195af444

Rotte, G., Kerkvliet, M., & van Terwisga, T. (2018). On the Influence of Eddy Viscosity in the Numerical Modelling of Air Cavities. In *Proceedings of the 10th International Symposium on Cavitation (CAV2018)*. ASME Press. https://doi.org/10.1115/1.861851_ch164

Rotteveel, E. (2019). *Influence of inland vessel stern shape aspects on propulsive performance: Derivation of insights and guidelines based on a computational study* [Doctoral dissertation, Delft University of Technology]. https://doi.org/10.4233/uuid:8d8c14e3-cdfb-4e15-8314-35dc296fdbde

Sanders, W. C., Winkel, E. S., Dowling, D. R., Perlin, M., & Ceccio, S. L. (2006). Bubble friction drag reduction in a high-Reynolds-number flat-plate turbulent boundary layer. *Journal of Fluid Mechanics*, *552*, 353–380. https://doi.org/10.1017/S0022112006008688

Seo, D.-W., & Oh, J. (2021). Uncertainty analysis of speed–power performance based on measured raw data in sea trials. *International Journal of Naval Architecture and Ocean Engineering*, *13*, 396–404. https://doi.org/https://doi.org/10.1016/j.ijnaoe.2021.04.001

Shevchuk, I., Böttner, C.-U., & Kornev, N. (2016). Numerical analysis of the flow in the gap between the ship hull and the fairway bottom in extremely shallow water. *4th MASHCON - International Conference on Ship Manoeuvring in Shallow and Confined Water with Special Focus on Ship Bottom Interaction*, 37–42. https://dx.doi.org/10.18451/978-3-939230-38-0_5

Shiri, A., Leer-Andersen, M., Bensow, R., & Norrby, J. (2012). Hydrodynamics of a displacement air cavity ship. *29th Symposium on Naval Hydrodynamics*. https://www.researchgate.net/publication/235935067_Hydrodynamics_of_a_Displacement_Air_Cavity_Ship

Silberschmidt, N., Tasker, D., Pappas, T., & Johannesson, J. (2016). Silverstream system – air lubrication performance verification and design development. In V. Bertram (Ed.), *Proceedings of the 10th symposium on high-performance marine vehicles (hiper 2016)* (pp. 236–246). Technische Universität Hamburg-Harburg. http://data.hiper-conf.info/Hiper2016_Cortona.pdf

Spalart, P. (2000). Strategies for turbulence modelling and simulations. *International Journal of Heat and Fluid Flow*, *21*(3), 252–263. https://doi.org/10.1016/S0142-727X(00)00007-2

Sverchkov, A., & Borusevich, V. (2019). Artificial cavity as a tool for reducing ship resistance [in Russian]. *Transactions from the Krylov State Research Centre*, *1*(387), 20–31. https://doi.org/10.24937/2542-2324-2019-1-387-20-31

Thill, C. (2016). Air lubrication technology – past, present and future. In V. Bertram (Ed.), *Proceedings of the 10th symposium on high-performance marine vehicles (hiper 2016)* (pp. 317–330). Technische Universität Hamburg-Harburg. http://data.hiper-conf.info/Hiper2016_Cortona.pdf

Tuck, E. O. (1966). Shallow-water flows past slender bodies. *Journal of Fluid Mechanics*, *26*, 81–95. https://doi.org/10.1017/S0022112066001101

van den Bosch, M. (2010). Definition study - sailing on shallow water.

Vermeer, H. (1977). The behaviour of a ship in restricted waters. *International Shipbuilding Progress*, *24*, 323–335. https://content-iospress-com.tudelft.idm.oclc.org/download/international-shipbuilding-progress/isp24-280-01?id=international-shipbuilding-progress%2Fisp24-280-01

Villa, D., Gaggero, S., Gaggero, T., Tani, G., Vernengo, G., & Viviani, M. (2019). An efficient and robust approach to predict ship self-propulsion coefficients. *Applied Ocean Research*, *92*, 101862. https://doi.org/10.1016/j.apor.2019.101862

Vink, B. (2017). *Verification and Validation Study of the Flow Around the RSD Tug 2513* [master thesis]. Delft University of Technology. http://resolver.tudelft.nl/uuid:9117d884-749a-4349-a842-d097d04cc71e

Vrijdag, A., & de Vos, P. (2012). Uncertainties and margins in the ship propulsion system design process. In C. Newell (Ed.), *Proceedings of the international naval engineering conference and exhibition (inec)* (pp. 618–630). http://resolver.tudelft.nl/uuid:cbc9baff-9cbb-47f4-8b76-9de8d65a628b

Vrijdag, A. (2014). Estimation of uncertainty in ship performance predictions. *Journal of Marine Engineering & Technology*, *13*, 45–55. https://doi.org/10.1080/20464177.2014.11658121

Werner, S., & Gustafsson, L. (2020). Uncertainty of speed trials. *Proceedings of the 5th Hull performance Insight Conference (HullPIC'20)*. http://data.hullpic.info/HullPIC2020_Hamburg.pdf

Wu, H., Ou, Y., & Ye, Q. (2019). Experimental study of air layer drag reduction on a flat plate and bottom hull of a ship with cavity. *Ocean Engineering*, *183*, 236–248. https://doi.org/10.1016/j.oceaneng.2019.04.088

Wu, H., Ou, Y., & Ye, Q. (2020). Numerical study on the influence of air layer for propeller performance of large ships. *Ocean Engineering*, *195*, 106681. https://doi.org/10.1016/j.oceaneng.2019.106681

Zeng, Q. (2019). *A method to improve the prediction of ship resistance in shallow water* [Doctoral dissertation, Delft University of Technology]. https://doi.org/10.4233/uuid:d4d8524a-fedc-4949-a953-f5848a1634bb

Zverkhovskyi, O. (2023). CFD Study on a Flow Around a Vessel With Air Cavities on the Bottom. *Proceedings of the 25th Numerical Towing Tank Symposium, NuTTS*. https://blueoasis.pt/wp-content/uploads/2023/10/Nutts2023_proceedings_v4.pdf

Zverkhovskyi, O., Kerkvliet, M., Lampe, A., Vaz, G., & van Terwisga, T. (2015). Numerical study on air cavity flows. *Proceedings Proceedings of NuTTS 2015*. https://www.researchgate.net/publication/281834294_Numerical_Study_on_Air_Cavity_Flows

Zverkhovskyi, O. (2014). *Ship drag reduction by air cavities* [Doctoral dissertation, Delft University of Technology]. https://doi.org/10.4233/uuid:a5754f75-55c1-4407-bebb-41458e6c9a11

Appendix A
Actuator disk model

The actuator disk model, which can be used to compute the propeller thrust in behind condition, is implemented in FINE™/Marine in the following way. The momentum equations include a body-force f_b (a source term). An actuator disk with inner radius R_H, outer radius R_P, and thickness Δ can be defined, which should be equal to the propeller hub radius, radius, and thickness respectively. The center of the actuator disk is set at the propeller center. A body force distribution is then set on the actuator disk, with components f_{bx} (axial), $f_{br} = 0$ (radial), and $f_{b\theta}$ (tangential. The axial and tangential body force distributions vary in radial direction and are based on the Goldstein optimum circulation distribution, (Goldstein, 1929), without any loading at the propeller root and tip:

$$f_{bx} = A_x r^* \sqrt{1 - r^*} \tag{A.1}$$

$$f_{b\theta} = A_\theta \frac{r^* \sqrt{1 - r^*}}{r^* \left(1 - r'_h\right) + r'_h} \tag{A.2}$$

f_{bx} and $f_{b\theta}$ are a function of the normalized radial coordinate r^*:

$$r^* = \frac{r' - r'_h}{1 - r'_h} \tag{A.3}$$

with r' and r'_h defined as:

$$r' = \frac{r}{R_p} \tag{A.4}$$

$$r'_h = \frac{R_H}{R_P} \tag{A.5}$$

with propeller radius R_P and hub radius R_H

$$r = \sqrt{\left(y - Y_{PC}\right)^2 + \left(z - Z_{PC}\right)^2} \tag{A.6}$$

with Y_{pc} and Z_{pc} the propeller center coordinates in respectively y and z direction. r^* is defined in such a way that it equals 0 at the propeller root and 1 at the propeller tip. The other coefficients are expressed as:

$$A_x = \frac{C_T}{\Delta} \frac{105}{16 \left(4 + 3r'_h\right) \left(1 - r'_h\right)} \tag{A.7}$$

with actuator disk thickness Δ.

$$A_\theta = \frac{K_Q}{\Delta J^2} \frac{105}{\pi \left(4 + 3r'_h\right) \left(1 - r'_h\right)} \tag{A.8}$$

$$C_T = \frac{2T}{\rho V^2 \pi R_P^2} \tag{A.9}$$

with reference velocity V. K_T, K_Q and J were already defined in section 2.3.1. Integrating the body forces over the actuator disk volume results in the prescribed thrust T and torque Q:

$$T = \int \int_A f_{bx} dA \tag{A.10}$$

$$Q = \int \int_A r f_{b\theta} dA \tag{A.11}$$

$$dA = 2\pi r \Delta dr \tag{A.12}$$